UNIVERSITY OF OKLAHOMA

GRADUATE COLLEGE

DETECTION OF "TRILOBITE" AND "BUTTERFLY" RYDBERG MOLECULES IN CESIUM WITH KILODEBYE DIPOLE MOMENTS

A DISSERTATION

SUBMITTED TO THE GRADUATE FACULTY

in partial fullfillment of the requirements for the

Degree of

DOCTOR OF PHILOSOPHY

By

DONALD W. BOOTH
Norman, Oklahoma
2015

DETECTION OF "TRILOBITE" AND "BUTTERFLY" RYDBERG MOLECULES IN CESIUM WITH KILODEBYE DIPOLE MOMENTS

A DISSERTATION APPROVED FOR THE
HOMER L. DODGE DEPARTMENT OF PHYSICS AND ASTRONOMY

BY

Dr. James P. Shaffer, Chair

Dr. Gregory Parker

Dr. Eric Abraham

Dr. Sheena Murphy

Dr. Zhisheng Shi

This thesis is dedicated to my mother, and to the loving memory of my father.

Acknowledgements

I would first like to acknowledge my advisor James P. Shaffer, without whose firm guidance I never would have gotten to where I am now. Second, I would like to acknowledge Jonathan Tallant. He taught me all about Zeeman slowers, dye lasers, and countless other important bits of experimental knowledge. I would also like to acknowledge Arne Schwettmann. His knowledge of computational physics has been an immense help on many of the problems I've had to solve. I also want to thank Jin Yang, who has been invaluable in his assistance in running the experiment and who I think will be a very capable person to take over the experiment, and Jon Sedlacek, who I've had many interesting conversations with while working late in the lab. I would also like to thank Henry Neeman, director of the Oklahoma Supercomputing Center for Education and Research (OSCER) for his assistance in my use of the supercomputing cluster in computational work – and for putting up with me when I screwed things up. Additionally, I would like to acknowledge our collaborators Seth Rittenhouse and Hossein Sadeghpour for their help on the theory for the trilobite molecules. Finally, I would like to thank Mark Saffman for offering me the opportunity to do post-doctoral research in his group at the University of Wisconsin, where I will be working on quantum computation using holmium.

Table of Contents

List of Tables

List of Figures

Abstract

The detection and characterization of two classes of ultralong-range Rydberg molecules known as "trilobite" and "butterfly" molecules is presented. These molecules are a subset of a class of Rydberg molecules which asymptotically consist of a Rydberg atom and a ground state atom. The trilobite and butterfly molecules have giant, body-fixed permanent dipole moments on the order of 1000 Debye. The two classes of molecules are distinguished by the relative dominance of the s-wave and p-wave electron scattering. Spectra for $(nS_{1/2} + 6S_{1/2})^3\Sigma$ molecules, where $n = 37$, 39 and 40 and measurements of the Stark broadenings of selected trilobite states in Cs due to the application of a constant external electric field are presented. Additionally, measurements of spectra and Stark splittings for p-wave dominated $(nS_{1/2} + 6S_{1/2})^3\Pi$ molecules, where $n = 31$ and 32 are presented. Computational work on Rydberg pair interactions is also discussed.

Chapter 1

Introduction

1.1 Ultralong-range Rydberg molecules

Rydberg molecules are an exotic class of homonuclear diatomic molecules which asymptotically consist of a Rydberg atom and a ground state atom. A simple cartoon picture of this system is shown in Fig. 1.1. The scattering of the Rydberg atom's electron off of the ground state atom provides the binding mechanism for the molecule. Additionally, admixtures between states, as will be discussed in Section 2.4, allow the formation of previously-unobserved "trilobite" and "butterfly" states, which have particularly large dipole moments [1, 2, 3]. Dipole moments are of interest in various applications, including control of chemical reactions and dynamics [4, 5, 6], quantum information processing [7], and tests of fundamental physical laws [4].

The theory describing the unique bonding mechanism of Rydberg molecules derives from a theoretical description by Enrico Fermi in 1934 [8]. The model Fermi used was developed to describe the broadening of spectral lines of excited states due to the presence of high-pressure gases. A notable parameter in this model is the scattering length, which determines whether the interactions in the mean-field potential are attractive or repulsive, thus determining the sign of the shift in the spectral line. The sign of the scattering length determines

whether the interaction is attractive (corresponding to a negative scattering length) or repulsive (corresponding to a positive scattering length). In 1977, Omont used the Fermi model to describe the interaction due to scattering of a Rydberg atom's electron from a neutral perturber such as a ground state atom [9]. While bound states, according to this theory, were possible, the energy scales involved were too small to observe with the technology available at the time. The development of laser cooling, which created the field of ultracold atomic physics, renewed interest in the subject. In 2000, Greene *et al.* refined the theory of Omont and found two primary classes of Rydberg molecules: a symmetric molecule corresponding to a Rydberg state with low orbital angular momentum L, and a dipolar "trilobite" molecule corresponding to a Rydberg state with high angular momentum, also known as a hydrogenic state [3]. In 2002, Hamilton *et al.* further predicted the existence of p-wave dominated "butterfly" molecules at higher electron energies than the trilobite molecules [10]. Both the trilobite and butterfly molecules are predicted to have very large dipole moments, on the order of 1000 Debye, making it possible to manipulate these molecules with very small electric fields.

The binding energies for these molecules are small ($\sim$ 1GHz, or $\sim 5\ \mu$eV). To observe these molecules, ultracold samples ($T \sim 40\ \mu$K) at high density (5×10^{13} cm^{-3}) are required. The observation is performed in a crossed far off resonance optical dipole trap, which allows us to achieve the required tempera-

tures and densities for the formation of Rydberg molecules.

Several experiments have previously been done on Rydberg molecules, primarily using ^{87}Rb. The first observation of these molecules was in 2009, where Rydberg molecules corresponding to an $(nS+5S)^3\Sigma$ state in ^{87}Rb were observed [11]. These molecules have binding energies on the order of 10 MHz. Some of these states were later determined to be bound by quantum internal reflection due to the presence of an avoided crossing in the Born-Oppenheimer potential curves of the molecular states [12]. This avoided crossing also led to a small degree of mixture between the state asymptotically corresponding to $nS+5S$ and states asymptotically corresponding to $((n-3)(L\geq 3)+5S)^3\Sigma$. This small admixture results in these molecules possessing a dipole moment of ~ 1 Debye [1].

Rydberg molecules corresponding to $(nD+5S)^3\Sigma$ have been observed in 2014 in experiments at the University of Michigan [13] and the University of Stuttgart [14]. These states lack the high-angular momentum admixture of the $nS+5S$ states, and thus have small dipole moments. Typical binding energies for these molecules are on the order of 10 MHz, and they possess dipole moments of < 1 Debye.

Additionally, experiments have been done in Rb focusing on $nS+5S$ states where $n > 60$ [15]. At high principal quantum number n, the radius of the Rydberg molecule becomes very large (scaling as n^2) and as a result there can be a large number of ground state atoms inside the Rydberg atom's electron cloud.

This facilitates the formation of trimers, tetramers, and Rydberg molecules with larger numbers of ground state atoms. The typical binding energies for these molecules is very small (< 1 MHz), and as the number of bound ground state atoms becomes large, the resonances become indistinguishable. In Rb these states have very small dipole moments.

In 2012, we observed Rydberg molecular resonances detuned to the blue of the $nS_{1/2}$ atomic lines in ^{133}Cs, where $31 \leq n \leq 34$. These states are located in potential wells asymptotically corresponding to the $(n-4)(L \geq 3)+6S)^3\Sigma$ states in ^{133}Cs. Because of avoided crossings in the ^{133}Cs potential curves which are more prominent than in the ^{87}Rb potential curves, these states have a very large ($\sim 99\%$) admixture of the $(nS + 6S)^3\Sigma$ state. However, the $\sim 1\%$ remaining admixture in the high angular momentum states allows these molecular states to have significantly larger dipole moments than were observed in ^{87}Rb. These dipole moments have been calculated to be $\sim 20 - 100$ Debye [2].

Further experiments on Rydberg molecules in ^{133}Cs are presented in this thesis. The molecules discussed in this thesis differ from the molecules observed in previous experiments in several ways. Due to the near-degeneracy of the nS and $(n-4)(L \geq 3)$ atomic states in ^{133}Cs as well as the large spin-orbit coupling of ^{133}Cs, these molecular states have large admixtures ($\sim 90\%$) of the "trilobite" state. Because of mixing between opposite-parity states in the hydrogenic manifold, the trilobite states can have a large degree of symmetry-breaking. This symmetry-breaking leads to localization of the Rydberg electron on the ground

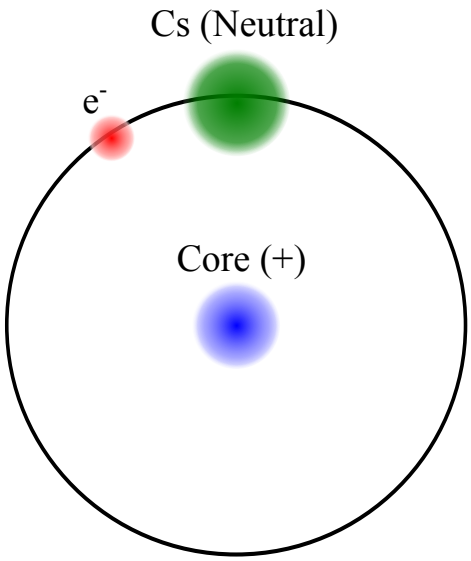

Figure 1.1: A cartoon picture of the Rydberg molecule system. A neutral ground state atom (shown in green) is in the electron cloud of a Rydberg atom (ionic core shown in blue). The electron scatters off the ground state atom, providing the binding mechanism for the molecule.

state atom, which in turn leads to a large dipole moment. As a result of the large admixture of the trilobite state in the observed states, these molecules have very large dipole moments on the order of 2000 Debye. The "trilobite" molecules are formed due to low-energy s-wave scattering. We have also observed a class of "butterfly" molecules formed in ^{133}Cs due to higher-energy p-wave scattering.

1.2 Rydberg-Rydberg pair interactions

In Chapter 3, systems of two Rydberg atoms are discussed. A cartoon image of this system is depicted in Fig. 1.2. These systems differ from the trilobite molecules discussed above in several ways. The distance between the pairs of Rydberg atoms is too large for the electron wavefunctions to overlap, so scattering interactions are not significant. The primary form of interaction between the pair of Rydberg atoms in this system is multipolar interactions. Additionally, the size scale of the Rydberg pair system is much greater than the scale of the trilobite system (~ 6 μm versus ~ 0.1 μm). The interactions of the Rydberg atom pairs can be described by pair potential curves. While the Rydberg molecule system described above can also be described in terms of pair potential curves because the electron, the third body in the three-body system, is much lighter than the other two bodies, the Rydberg-Rydberg pair system is effectively a true two-body system.

Numerous experiments have studied the interactions of Rydberg atoms in various contexts, including dipole blockade [16], resonant energy transfer [17, 18, 19], and state-changing interactions between Rydberg atoms [20]. In our lab, we have observed bound states, called macrodimer states, formed in wells in the potential surfaces of the Rydberg-Rydberg pair systems in the presence of an electric field [21].

Chapter 3 presents computational work done on several different Rydberg

pair systems. State-changing interactions between $nD + nD$ Rydberg pairs in ^{87}Rb, where $29 \leq n \leq 43$, are presented. The results from our computational work on this system illustrate the importance of pair interactions in Rydberg systems. This type of system is one which it had been assumed could only be described as a many-body system. However, the experimental results for this system indicate that the behavior of the system is due to two-body interactions, and our calculation is able to describe the behavior of the system.

Anisotropic scattering calculations for $90D + 90D$ pairs of Rydberg atoms interacting on a potential surface in a 100 mV cm^{-1} background electric field are described. The atoms in this system are polarized by the electric field and exhibit a strong dipolar anisotropy as a result. Avoided crossings in the potential surfaces result in non-adiabatic transitions between states which we analyze in our scattering calculations.

Third, numerical calculations for a system of Rydberg atoms in a hot vapor cell are discussed. These atoms are far above the ultracold temperatures that the other cases consider. Despite this, Rydberg-Rydberg interactions are still important to consider. In this type of system, Rydberg blockade – in which excitation of Rydberg atoms is inhibited by the presence of neighboring Rydberg atoms – is very significant, as well as anti-blockade – in which the excitation of Rydberg atoms by off-resonant light is enhanced by the presence of a neighboring Rydberg atom. This work focuses on the anti-blockade effect, which can give rise to aggregations of Rydberg atoms formed as a result of a few off-resonant

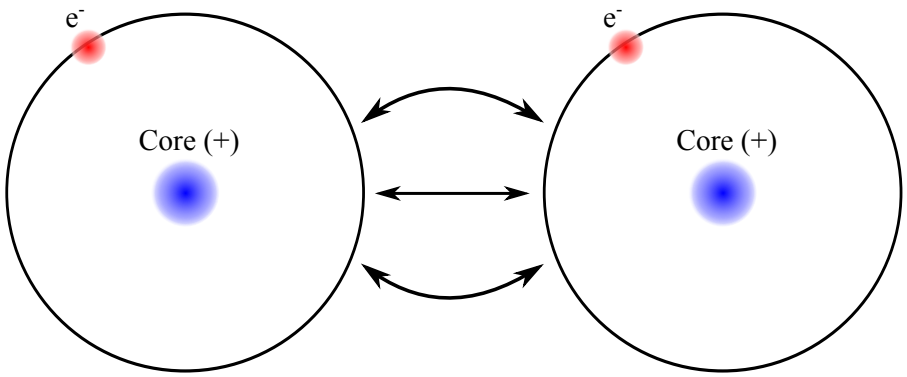

Figure 1.2: A cartoon picture of the Rydberg-Rydberg pair system. Two Rydberg atoms, whose electron clouds do not overlap, interact with each other via multipolar interactions.

excitations.

Fourth, numerical calculations for a transitions of Rydberg atoms from $nD + nD$ states to $(n-2)P + (n+2)(L \gg 3)$ states in ^{87}Rb are described. Dipole blockade is again an important effect in this case: as the density of atoms is increased, the resonances observed in the experiment corresponding to Förster resonances with $(n-2)P + (n+2)(L \gg 3)$ broaden.

1.3 Structure of this thesis

This thesis is organized as follows. Chapter 2 explains the theoretical principles of the Rydberg molecules and Rydberg pair interactions that are explored in the thesis. Various properties of Rydberg atoms and their relevance to Rydberg molecules and pair interactions are described. Section 2.3 compares and contrasts

two different systems: the Rydberg molecule system, consisting of a Rydberg atom and a ground state atom, and the Rydberg pair system, consisting of two Rydberg atoms. The theoretical models that describe the Rydberg molecule and Rydberg pair systems are also presented. Chapter 3 discusses the calculations that were performed for various Rydberg-Rydberg pair systems in ^{87}Rb and ^{133}Cs.

Chapter 4 describes the experimental apparatus used in the Rydberg molecule experiments. The vacuum systems and ^{133}Cs ovens for the main chamber and the Zeeman slower are presented. In addition the magneto-optical trap (MOT) and far-off resonance trap (FORT) systems are described. The systems for excitation and detection of Rydberg atoms are also explained. Additionally, the systems for frequency reference using electromagnetically-induced transparency (EIT) are introduced.

The observations of "trilobite" and "butterfly" ultralong-range Rydberg molecules are the primary results presented in this thesis, and these are discussed in Chapter 5. The measurements of the spectra associated with these states, as well as measurements of the molecular-frame permanent electric dipole moments of these molecules are presented.

In Chapter 6, the main body of the thesis is concluded and future directions for the experiment are presented. Following Chapter 6, instructions for use of the Rycol program, results from which are discussed in Chapter 3, are presented in Appendix A.

Chapter 2

Theory

2.1 Introduction

In this chapter, the properties of Rydberg atoms are introduced, and these properties are used in the discussion of ultralong-range Rydberg molecules and Rydberg-Rydberg interactions. The scaling laws of Rydberg atoms are important for understanding the uses of Rydberg atoms and their propensity to form bound states such as macrodimers and Rydberg molecules. Several types of Rydberg molecules which can be formed due to scattering of the Rydberg atom's valence electron by neighboring ground state atoms are discussed in this chapter. Additionally, multipolar interactions between pairs of Rydberg atoms, which can give rise to state-changing interactions and macrodimer states, are discussed.

2.2 Properties of Rydberg atoms

The experiments described in this thesis involve Rydberg atoms. Rydberg atoms are atoms in highly-excited states, where the principal quantum number $n >> 1$. These atoms, due to the weak binding between the valence electron and the ionic core, have highly exaggerated properties compared to atoms with lower n.

2.2.1 Scaling laws

Many of the properties of Rydberg atoms obey scaling laws as a function of n. For example, the polarizability of the atom scales as n^7 [22]. This means that an atom in the $100S_{1/2}$ state will have a polarizability that is $2^7 = 128$ times the polarizability of an atom in the $50S_{1/2}$ state. A list of selected scaling laws is presented in Table 2.1.

These scaling laws have important effects on experiments involving Rydberg atoms. For example, the transition dipole moment from the $6P_{3/2}$ state into a dipole-allowed Rydberg state scales as n^{-2}. This means that it requires far more laser power to achieve the same Rabi frequency at higher n as compared to lower n.

The radius of the atom scales as n^2, which is important in the behavior of the ultralong-range Rydberg molecules which are discussed later in the chapter. The minimum of the Born-Oppenheimer potential well in which the molecule resides is located at the outermost antinode in the atomic wavefunction. As the distance between the two atoms increases, the possible dipole moments that the molecule can have also increase. Thus, ultralong-range Rydberg molecules in states with larger n can possess a larger dipole moment.

Table 2.1: Selected scaling laws for Rydberg atom properties.

Property	Scales as [22]	Cs $40S_{1/2}$
Atomic radius	n^2	123 nm
Spacings between adjacent energy levels	n^{-2}	136 GHz
Polarizability	n^7	6 MHz (V cm^{-1})$^{-2}$
Radiative lifetime	n^3	68 μs

2.2.2 State energies

In Rydberg atoms the electron typically orbits far from the ionic core, and so its behavior and state energies are similar to those of the hydrogen atom. However, because the ionic core has a finite size and a charge distribution significantly different to those of the proton in the hydrogen atom, the electron has a significant interaction with the core that must be considered in calculating the energy states. This is particularly the case for states with lower orbital angular momentum, as the electron spends more time near the ionic core.

The most common way to include the interaction of the electron with the core is with quantum defect theory. When the quantum defect is included the energy E_{nlj} is, in atomic units:

$$E_{nlj} = -\frac{1}{2(n-\delta_{nlj})^2}, \tag{2.1}$$

where δ_{nlj} is the quantum defect, and is dependent primarily on the orbital quantum number l, but also to a lesser extent on the total angular momentum j

and the principal quantum number n. The quantum defect is expressed as an expansion in powers of $(n - \delta_0(l, j))$, where $\delta_0(l, j)$ is the zeroth-order term of the expansion:

$$\delta_{nlj} = \delta_0(l, j) + \sum_{k=0}^{\infty} \frac{\delta_{2k}(l, j)}{(n - \delta_0(l, j))^{2k}}. \tag{2.2}$$

The expansion coefficients $\delta_{2k}(l, j)$ can be found by fitting energy levels observed in experimental spectra (Cs: [23], Rb: [24, 25]). For practical reasons it is necessary to truncate the sum, typically at the highest order for which coefficients are available.

Because of fine-structure splitting the $\delta_{2k}(l, j)$ terms are dependent on j, but the coefficients given in [23] for Cs are not j-dependent. Thus, it is necessary to separately include the j dependence. The expression used for the fine-structure splitting is: [26]

$$\Delta_{\rm fs}(n, l, J; n, l, J+1) = A\left[n - \epsilon_{l,J,J+1}(n)\right]^{-3} + B\left[n - \epsilon_{l,J,J+1}(n)\right]^{-5} + C\left[n - \epsilon_{l,J,J+1}(n)\right]^{-7}, \tag{2.3}$$

where the average quantum defect $\epsilon_{l,J,J+1}(n)$ is given by the expression:

$$\epsilon_{l,J,J+1}(n) = \epsilon_{l,J,J+1}(\infty) + a_{l,J,J+1}\left[n - \epsilon_{l,J,J+1}(\infty)\right]^{-2}. \tag{2.4}$$

The parameters A, B, C, $\epsilon_{l,J,J+1}(\infty)$, and $a_{l,J,J+1}$ are l-dependent and are listed in Table 5 in [26].

2.2.3 Wavefunctions

To calculate wavefunctions for Rydberg states, we use an l-dependent model potential presented in [27]:

$$V_l(r) = -\frac{Z_l(r)}{r} - \frac{\alpha_c}{2r^4}\left[1 - e^{-(r/r_c)^6}\right], \tag{2.5}$$

where r_c is a cutoff radius used in the model, α_c is the static dipole polarizability of the positive-ion core, and the radial charge parameter Z_l is given by:

$$Z_l(r) = 1 + (z-1)e^{-a_1 r} - r(a_3 + a_4 r)e^{-a_2 r}, \tag{2.6}$$

where z is the nuclear charge of the atom (e.g. 55 for Cs), and a_n are parameters of the fit used in the model.

With this potential, we apply the Schrödinger equation to obtain wavefunctions for each state. To numerically solve the 1-D radial Schrödinger equation, we use a Fortran program called RADIAL [28]. Using the SBOUND subroutine, RADIAL can calculate the bound states in the potential on a variably-spaced grid. The grid spacing is selected so that grid points are closer-spaced at short range, where the wavefunctions are more oscillatory, and farther-spaced at long range, where the wavefunctions are less oscillatory. An example of the output of the program is shown in Fig. 2.1. The potential expressed in Eqn. 2.5 is shown in blue, with wavefunctions corresponding to the $35S$, $45S$, $60S$, and $90S$ Rydberg states shown in red.

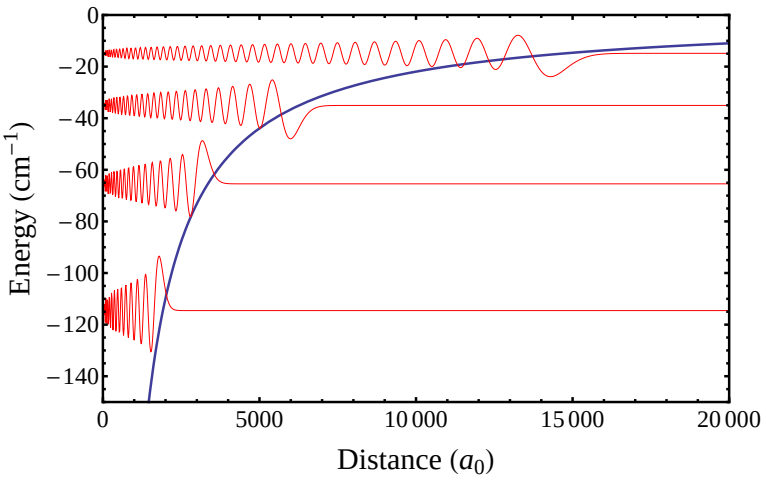

Figure 2.1: The l-dependent model potential for $l = 0$ from 2.5 is shown in blue, with corresponding wavefunctions for the $35S$, $45S$, $60S$, and $90S$ Rydberg states calculated using RADIAL shown in red.

Additionally, this program can calculate continuum wavefunctions above the ionization threshold using the SFREE subroutine, which is necessary for determining photoionization cross sections for Rydberg states in an optical dipole trap.

2.2.4 Lifetimes

There are two principal components to the lifetime of a Rydberg state: radiative and blackbody decay. A Rydberg atom decays radiatively due to spontaneous emission as a result of the finite lifetime of the excited state. However, because the Rydberg levels are close in energy, blackbody radiation from the surrounding

environment can induce transitions in the far infrared, acting as another source of loss from the Rydberg state.

The radiative lifetimes scale approximately as n_{eff}^3 [29]:

$$\tau_r = \tau_s n_{eff}^3, \tag{2.7}$$

where $n_{eff} = (n - \delta_{nlj})$ is the effective principal quantum number, and τ_s is a parameter for the radiative lifetime that depends on l as well as the properties of the atom. The radiative lifetime τ_r can be combined with the blackbody lifetime τ_{bb} to obtain the effective lifetime of the state τ_{eff}:

$$\tau_{eff} = \left(\frac{1}{\tau_r} + \frac{1}{\tau_{bb}} \right)^{-1}. \tag{2.8}$$

In [29] an empirical expression for the lifetimes is given:

$$\tau_{eff} = \left(\frac{1}{\tau_s n_{eff}^{\delta}} + \frac{A}{n_{eff}^D} \frac{21.4}{\exp(315780B/n_{eff}^C T) - 1} \right)^{-1}, \tag{2.9}$$

where the parameters A, B, C, D, and δ are atom-dependent and state-dependent, and are listed in [29]. T is the temperature of the environment in Kelvin. This expression yields the lifetime in ns. This model has been verified by observations in Cs [30] and Rb [31, 32].

Rydberg atoms formed in an optical dipole trap experience another form of loss due to photoionization. In the presence of the dipole trap light, the effective lifetime becomes:

$$\tau_{eff} = \left(\frac{1}{\tau_r} + \frac{1}{\tau_{bb}} + \frac{1}{\tau_{PI}} \right)^{-1}, \tag{2.10}$$

where τ_{PI}^{-1} is the rate of photoionization in the trap. The rate of photoionization can be calculated from the photoionization cross section σ using the expression:

$$\frac{1}{\tau_{PI}} = \frac{I}{\hbar\omega}\sigma, \tag{2.11}$$

where ω is the angular frequency of the trapping light, and I is the light intensity at the trap center. The photoionization cross section can be obtained using the expression [33]:

$$\sigma = 2\pi^2 \frac{\hbar e^2}{mc} \frac{df}{dE}\bigg|_{E_c}, \tag{2.12}$$

where $E_c = \hbar\omega + E_r$ is the energy of the electron removed from the atom (the Rydberg state energy E_r plus the energy of one photon from the ionizing field), and the oscillator strength distribution df/dE is given by:

$$\frac{df}{dE} = \sum_{L=(L_r-1,L_r+1)} \frac{2m\omega \ \mathrm{Max}(L_r, L)}{3\hbar(2L_r+1)} \left| \int \Psi_r(r) r \phi_{L,E}(r) dr \right|^2, \tag{2.13}$$

where L_r is the angular momentum of the Rydberg state, $\Psi_r(r)$ is the radial wavefunction of the Rydberg state, and $\phi_{L,E}(r)$ is the wavefunction of the continuum state.

2.3 Types of ultralong-range bound states involving Rydberg atoms

There are two different types of ultra-long range bound states discussed in this thesis. The first type, commonly known as ultralong-range Rydberg molecules, is a system composed of a Rydberg atom and a ground state atom, where the ground state atom is inside the electron cloud of the Rydberg atom. The molecule is bound by scattering of the Rydberg electron and the ground state atom. The second type, commonly known as a Rydberg macrodimer, is a system composed of two Rydberg atoms, bound by multipolar interactions. The internuclear spacing for a macrodimer is large enough that there is no overlap between the wave functions of the two atoms.

These two types of bound states involving Rydberg atoms are both extremely long-range: the typical internuclear spacing for the trilobite molecules is $\sim$ 100 nm [3], and for the macrodimers the internuclear spacing is $\sim$ 5000 nm [34]. For comparison, the internuclear spacing of a ground-state Cs_2 molecule is on the order of 0.1 nm.

2.4 Rydberg Molecules

2.4.1 Introduction

Rydberg molecules, composed of a Rydberg atom and a ground state atom bound by the scattering of the Rydberg electron from the ground state atom, can be placed in three categories, characterized by the orbital angular momentum of the Rydberg electron and the relative dominance of the s-wave and p-wave scattering interactions. When the angular momentum of the Rydberg electron $L < 3$, a symmetric molecule with no permanent electric dipole moment is possible. This, however, ignores admixtures between states which can introduce a dipole moment. These admixtures will be discussed later.

When $L \geq 3$, two different types of molecules are possible, depending on the relative dominance of the s-wave and p-wave scattering interactions. When the s-wave interaction is dominant, which occurs at low electron energies corresponding to large internuclear distances, a "trilobite" molecule is formed. The name comes from the shape of the Rydberg electron's probability density distribution [3], which is shown in Fig. 2.2 for three states in Cs. For the states shown, there is a small admixture of the symmetric molecular state, which increases with n. The trilobite states have very large dipole moments $\sim 1 - 3$ kDebye, and they have Σ molecular symmetry.

When the p-wave term is dominant, which occurs at high electron energies, corresponding to short internuclear distances, a "butterfly" molecule is formed.

The name again comes from the shape of the Rydberg electron's probability distribution [10]. The butterfly states have large dipole moments on the order of kDebye, and can exhibit Π or $\Sigma(M = 0)$ molecular symmetry.

2.4.2 Electron-atom scattering

The scattering length a determines whether the potential curves for the system are attractive or repulsive. If the scattering length is negative, then the potential is attractive, allowing bound states to form. A negative scattering length causes an attractive force between the electron and the ground state perturber, providing a binding mechanism for the molecule. This can also be seen in the potential curves (examples of which are shown in Fig. 2.4): the negative scattering length results in potential wells below the $nS+6S$ asymptote, which can support bound states. The dominant term in the scattering, the s-wave term, has a scattering length that is negative in the $^3\Sigma$ system for both Cs (a_s =−21.7 a_0) and Rb (a_s =−16.1 a_0) [35]. The $^1\Sigma$ system in Cs is also attractive, with a_s =−1.33 a_0, but this small scattering length yields very weak binding energies. As a result, $^1\Sigma$ states are not considered in this work.

The quantum defect of ^{133}Cs plays a large role in enabling large admixtures between the $(nS + 6S)^3\Sigma$ and $((n - 4)(L \geq 3) + 6S)^3\Sigma$ states. In ^{133}Cs, the zeroth-order term of the quantum defect of the S state is 4.05, compared to the Rb zeroth-order term of 3.13. The result is that the nS and $(n - 4)$ hydrogenic atomic energy levels are far closer to degeneracy in ^{133}Cs than in ^{87}Rb. This

Figure 2.2: Electron probability distributions for the red-detuned vibrational levels of the $(37S+6S)^3\Sigma$, $(39S+6S)^3\Sigma$, and $(40S+6S)^3\Sigma$ systems. The ionic core of the Rydberg atom is in the center of the distribution and the ground state atom is at the peak of the portion corresponding to the "trilobite" state. These states have an admixture in the symmetric state, which can be seen in the rings surrounding the ionic core in the probability density.

near-degeneracy facilitates the admixture between the states, as less energy shift is required to cause the Born-Oppenheimer potential curves to cross.

In addition, the $e^- + \mathrm{Cs}(6S)$ system has a shape resonance corresponding to the $6S6P$ state which is 8 meV above the $6S_{1/2}$ state [36]. This resonance is very important in the calculation of trilobite potential curves for Cs, as it shifts the energies of the curves, altering the structure of the crossings in the curves. Additionally, the spin-orbit coupling is very significant in ^{133}Cs. This is included in the potential calculations by adjusting the p-wave scattering length:

$$a_p = \sum_{J=0}^{2} \left(C_{10,1M_J}^{JM_J}\right)^2 a_{p,J}^3, \tag{2.14}$$

where $C_{10,1M_J}^{JM_J}$ is the Clebsch-Gordan coefficient coupling the Rydberg electron's angular momentum to the angular momentum of the Rydberg–ground state atom system.

2.4.3 Theoretical model

The simplest approximation of the potential curves for a trilobite molecule uses the Fermi pseudopotential method. This model was first established by Enrico Fermi in 1934 to describe broadenings seen in excited state spectral lines in gases. The Born-Oppenheimer potential, according to this model, can be expressed as,

$$V_{pseudo}(\vec{r}, \vec{R}) = 2\pi a(k)\delta(\vec{r} - \vec{R}) = 2\pi \frac{\tan(\eta_0)}{k}\delta(\vec{r} - \vec{R}), \tag{2.15}$$

where $\vec{r}$ is the position of the electron, R is the position of the ground state perturber, and $a(k)$ is the energy-dependent s-wave scattering length. $a(k)$ is often written in terms of the (energy-dependent) s-wave scattering phase shift η_0:

$$a(k) = \frac{\tan(\eta_0)}{k}. \tag{2.16}$$

The wavenumber, k, is approximated using a classical model, considering the Rydberg state energy and the Coulomb interaction between the electron and the ionic core of the Rydberg atom:

$$\frac{k(R)^2}{2} = -\frac{1}{2n^2} + \frac{1}{R}. \tag{2.17}$$

The s-wave scattering term for the Rydberg atom–ground state atom system can be expressed as:

$$U_s(\vec{r}, \vec{R}) = 2\pi \frac{\tan(\eta_0)}{k} \left|\Psi_{nlm}(R)\right|^2, \tag{2.18}$$

where the delta function from the Fermi pseudopotential, when integrated over the electronic position, results in the potential depending on the probability density of the electron, $|\Psi_{nlm}(R)|^2$. Thus, the potential mimics the shape of the Rydberg electron probability distribution, resulting in multiple peaks and wells, corresponding to the nodes and antinodes of the probability distribution.

As the internuclear separation between the ground state perturber and the Rydberg ionic core decreases, the energy of the electron increases. As the

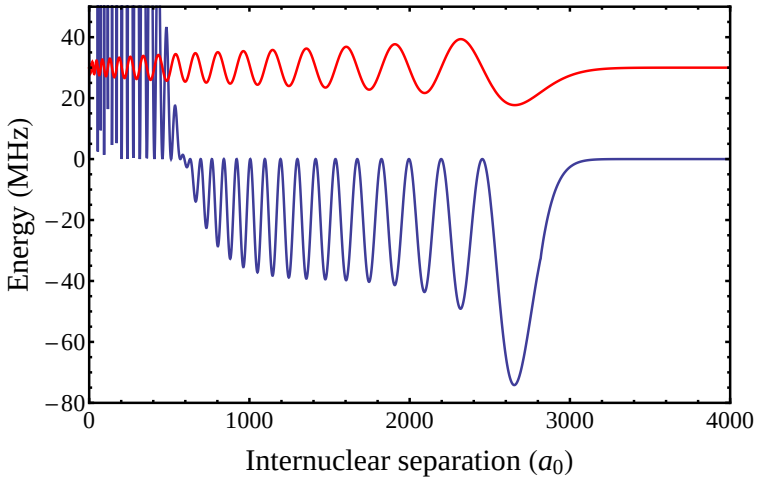

Figure 2.3: In red, the atomic wavefunction for the $40D_{5/2}$ state in Cs, in arbitrary units. In blue, the Fermi pseudopotential (with only s-wave scattering considered) for the $(40D_{5/2}+6S)^3\Sigma$ ultralong-range Rydberg molecular state.

energy increases, higher-order interactions – in particular, p-wave interactions – must be considered. These interactions are an extension of the pseudopotential method which allow higher-energy scattering to be considered. The reason for the necessity of the higher-order terms is illustrated in Fig. 2 of [10]. At zero energy, the p-wave phase shift is zero, and the s-wave interaction is the only term that needs to be considered. As the energy increases, though, the p-wave interaction increases and becomes larger than the s-wave interaction. At these energies, the p-wave interaction not only must be considered in the calculation, but is in fact the dominant interaction.

The p-wave interaction can be expressed in the potential as:

$$V_p(\vec{r}, \vec{R}) = -6\pi \frac{\tan(\eta_1)}{k^3} \vec{\nabla} \Psi_{nlm}(R) \cdot \vec{\nabla} \Psi_{nlm}(R'). \tag{2.19}$$

The p-wave potential is characterized by a scattering volume term, $\tan(\eta_1)/k^3$, and the p-wave potential depends on the gradient of the wavefunction rather than the magnitude.

Another method for calculating potential curves for Rydberg molecule systems involves the Coulomb function. This method was used in [12], and is described in detail in [37]. This method is particularly useful in cases where there are multiple avoided crossings, though the Fermi pseudopotential method produces sufficiently accurate results in most cases.

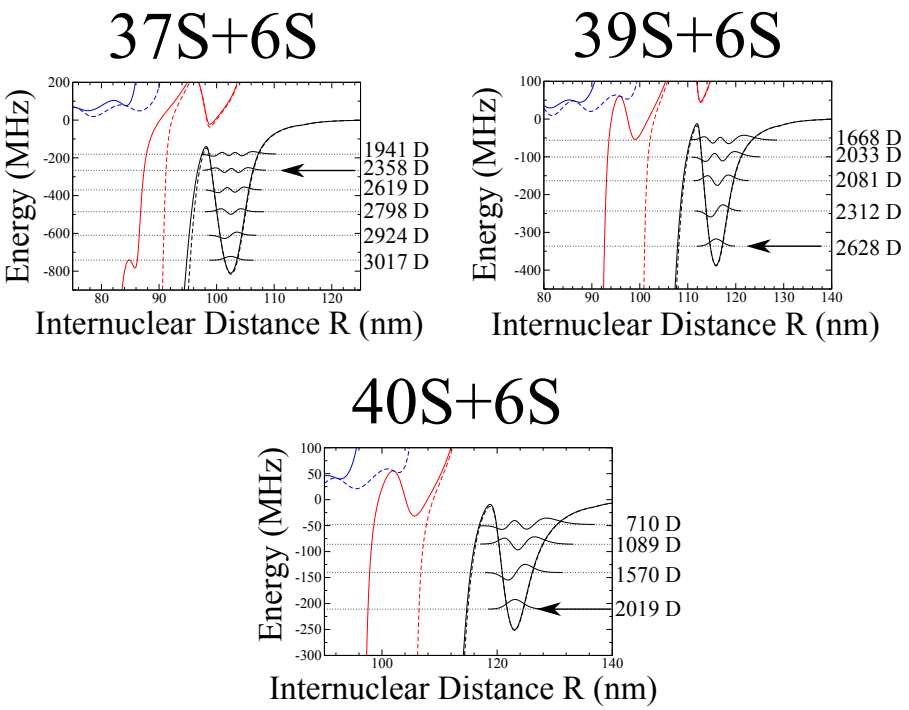

Figure 2.4: Potential curves for the $(37S + 6S)^3\Sigma$, $(39S + 6S)^3\Sigma$, and $(40S + 6S)^3\Sigma$ trilobite molecules. Bound vibrational states are indicated with the vibrational wavefunction and the corresponding dipole moment. The arrows indicate the states for which dipole moments were measured.

2.4.4 Dipole moments

The dipole moments in the trilobite and butterfly states occur due to the localization of the electron on the ground state perturber. This localization occurs as a result of the mixing of states of opposite parity: the degenerate $L \geq 3$ states have very large admixtures with each other. As a result the s-wave potentials for the hydrogenic states in the absence of interactions with other states (in particular, S states), can be expressed as:

$$V_{s(nlm)}(R) = 2\pi a(k) \sum_{l=l_{min}}^{n-1} \frac{2l+1}{4\pi} \left|\Psi_{nlm}(R)\right|^2, \tag{2.20}$$

where $l_{min} = 3$ is the minimum orbital angular momentum in the degenerate manifold.

Because of the large distances between the Rydberg ionic core and the ground state perturber, the localization of the electron can result in very large dipole moments. For the trilobite states, when $n = 37$, these dipole moments are ~ 3 kDebye.

The low-L symmetric Rydberg molecules do not, in the absence of admixtures with high-L states, have dipole moments. However, admixtures with the high-L states can be formed in certain circumstances. In ^{133}Cs, the non-integer portion of the quantum defect for the S state is very small: $\delta_{s(NI)} = 0.05$. This causes the S state to be nearly degenerate with the hydrogenic states, which have quantum defects that are approximately zero. This can be illustrated by comparing the

energy spacing between the $36S$ and $32F$ states in ^{133}Cs to the $35S$ and $32F$ states in ^{87}Rb (the difference in the n between ^{87}Rb and ^{133}Cs is due to the difference in the integer part of the S state quantum defect). For ^{133}Cs, the energy spacing is 3.3 GHz, while for ^{87}Rb, the energy spacing is 45 GHz [12].

The near-degeneracy between the S state and the hydrogenic states, combined with the large spin-orbit coupling and the low-energy p-wave resonance in Cs, allows significant admixtures between the S state and the hydrogenic states. These admixtures allow dipole moments to be imparted on states that are otherwise non-polar. For example, in ^{87}Rb, dipole moments of ~ 1 Debye were observed in Rydberg molecules with $< 1\%$ hydrogenic admixtures [1]. More recently, states were observed in Cs with dipole moments of $20 - 100$ Debye, due to hydrogenic admixtures of $\sim 1\%$ [2].

Experimental observation of trilobite states with hydrogenic admixtures of $60 - 90\%$ will be discussed in Chapter 5. These states form in the outermost potential well red-detuned from the $37S + 6S$, $39S + 6S$, and $40S + 6S$ states in Cs. The potentials for these states are depicted in Fig. 2.4. For $40S + 6S$, the hydrogenic admixture is $\sim 60\%$, resulting in smaller dipole moments than at $37S + 6S$, where the hydrogenic admixture is $\sim 90\%$. This is counterintuitive, considering the fact that the radius of the Rydberg electron increases as n^2: between $37S$ and $40S$, the radius increases from 105 nm to 123 nm. However, the hydrogenic admixture has a stronger effect on the dipole moments than the

radius, resulting in smaller dipole moments as n is increased.

2.5 Rydberg–Rydberg interactions

Pairs of Rydberg atoms interact via multipolar interactions, in contrast to the scattering interactions that bind the Rydberg molecules discussed in the previous section. These multipolar interactions are extremely long-range, with bound states being formed at internuclear separations on the order of microns. At small fields (e.g. $<\sim 50$ mV cm^{-1} for $90D_{5/2}$ in Cs) the dominant interaction is the van der Waals force. At larger fields, the atoms are polarized by the electric field, allowing the dipole-dipole, dipole-quadrupole, and quadrupole-quadrupole interactions to dominate. The interactions between pairs of Rydberg atoms are anisotropic, in that they depend on the relative alignment of the dipoles, which can be aligned by a background electric field. In addition, the very large polarizability of the Rydberg atoms allows the multipolar interactions to be tuned with electric fields, which becomes important in the formation of macrodimer states.

The interactions between pairs of Rydberg atoms can be determined via pair potential curves. To calculate these curves, we use a program called Rycol, the use of which is described in Appendix A. There are a series of steps required to calculate the pair potentials. First, a Stark Hamiltonian is calculated in a basis of selected atomic states and diagonalized to find Stark-shifted state energies

and wavefunctions. Then a pair state Hamiltonian is constructed using those Stark basis energies and wavefunctions. The pair state Hamiltonian is then diagonalized at different internuclear distances to produce the pair potentials.

The method used for calculating the Stark-shifted state energies and wavefunctions is described in [38]. The matrix elements are of the form (from equation 8 in [38]):

$$\langle nlm|\, Fz\, |n'l'm'\rangle = \delta_{m,m'}\delta_{l,l'\pm1} F\, \langle lm|\cos\theta\, |l'm'\rangle\, \langle nl|\, r\, |n'l'\rangle\,, \tag{2.21}$$

where F is the magnitude of the electric field, defined to be along the z axis, and the angular terms are:

$$\langle lm|\cos\theta\, |l-1,m\rangle = \left(\frac{l^2-m^2}{(2l+1)(2l-1)}\right)^{1/2}, \tag{2.22}$$

$$\langle lm|\cos\theta\, |l+1,m\rangle = \left(\frac{(l+1)^2-m^2}{(2l+1)(2l+3)}\right)^{1/2}. \tag{2.23}$$

The radial matrix elements $\langle nl|\, r\, |n'l'\rangle$ are calculated from wavefunctions that are computed using the Fortran program RADIAL [28]. The potential used for this calculation is the model potential from [27].

The pair state Hamiltonian can be calculated from the Stark basis using the expression [34]:

$$\langle\widetilde{\alpha}|\left\langle\widetilde{\beta}\right|H(R)\left|\widetilde{\alpha'}\right\rangle\left|\widetilde{\beta'}\right\rangle$$
$$=\delta_{\alpha\alpha'}\delta_{\beta\beta'}E_{\alpha\beta}+\langle\widetilde{\alpha}|\left\langle\widetilde{\beta}\right|\left(\sum_{L_1,L_2=1}^{2}\sum_{m=-L<}^{L<}C_{L_1,L_2m}\frac{r^{(1)^{L_1}}r^{(2)^{L_2}}}{R^{L_1+L_2+1}}Y^{(1)}_{L_1m}Y^{(2)}_{L_2m}\right)\left|\widetilde{\alpha'}\right\rangle\left|\widetilde{\beta'}\right\rangle, \tag{2.24}$$

where

$$C_{L_1,L_2m}=(-1)^{L_2}\frac{4\pi}{\left[(2L_1+1)(2L_2+1)\right]^{1/2}} \times\frac{(L_1+L_2)!}{\left[(L_1+m)!(L_1-m)!(L_2+m)!(L_2-m)!\right]^{1/2}}. \tag{2.25}$$

The above expression contains dipole-dipole, dipole-quadrupole, and quadrupole-quadrupole interactions, specified by the sum over L_1 and L_2: for dipole-dipole interactions, $L_1 = L_2 = 1$, for quadrupole-quadrupole interactions, $L_1 = L_2 = 2$, and for dipole-quadrupole interactions, one of the two variables is 2 while the other is 1. Higher-order terms can be included, but are sufficiently small that they are below the level of precision needed for the calculation. Because the electron clouds of the atoms do not overlap, the basis states for the pair calculation can be written in terms of the independent atom quantum numbers: $|\alpha\rangle\,|\beta\rangle = |n, l, j, m_j\rangle\left|n', l', j', m'_j\right\rangle$.

For cases where the internuclear axis is not parallel to the electric field, the pair state Hamiltonian must be rotated to place the z-axis along the electric field axis. The dependence of the Hamiltonian is in the form of spherical harmonics,

which can be rotated using the identity:

$$Y_l^m(\theta,\phi) = \sum_{m'} D^l_{m'm}(\Theta,\Phi,\Xi) Y_l^{m'}(\theta',\phi'), \tag{2.26}$$

where D is the Wigner rotation matrix, which depends on the Euler angles. For this case, Θ is the angle between the electric field and the internuclear axis.

The unrotated Hamiltonian is block-diagonal in the total projection of angular momentum along the internuclear axis $M = m_{j1} + m_{j2}$ greatly simplifying the diagonalization by allowing the calculation to be performed by diagonalizing a series of smaller Hamiltonians. However, the rotated Hamiltonian is no longer block diagonal, since the Wigner matrix mixes m while conserving l, requiring the full matrix with all M values to be diagonalized.

These pair potentials have been used for various applications, some of which are discussed in Chapter 3. Wells in pair potentials have been used to predict the presence of macrodimer states [34, 21]. In addition, avoided crossings in pair potentials can yield information about population transfer between Rydberg states [39].

Chapter 3

Rydberg-Rydberg Pair Interactions in an Electric Field

3.1 Introduction

At a range of $\sim \mu m$, Rydberg atoms primarily interact with each other via multipolar interactions. These interactions, along with the dense state structure of the Rydberg atoms, allows for intricate and complicated behavior. Rydberg atoms have large polarizabilities, which allows their interactions to be easily controlled with electric fields.

There are numerous applications for pair potential curves for Rydberg-Rydberg pair systems, including in quantum information [40, 7], resonant energy transfer [17, 18, 19], dipole blockade [16], collisions between Rydberg atoms [20], and Rydberg macrodimer systems [41, 42].

Pair interactions in Cs in the presence of electric fields have been used in our research group to create macrodimer states [21]. Anisotropic behavior in Rydberg pair interactions have been explored computationally by our research group [43] as well as experimentally by other research groups [44].

This chapter discusses numerical calculations done on four different Rydberg-Rydberg systems. First, state-changing interactions between $nD + nD$ Rydberg pairs in ^{85}Rb, where $29 \leq n \leq 43$, are discussed. Second, scattering calculations

for $90D + 90D$ pairs of Rydberg atoms interacting on an anisotropic potential in a 100 mV cm^{-1} background electric field are discussed. Third, numerical calculations for a system of Rydberg atoms in a vapor cell is discussed. Fourth, numerical calculations for a transitions of Rydberg atoms from $nD + nD$ states to $(n-2)P + (n+2)(L \gg 3)$ states in ^{85}Rb are discussed.

3.2 $nD + nD$ Pair Interactions in Rb

Non-adiabatic pairwise state-changing processes in Rydberg atoms are of interest because control of these interactions is necessary for understanding and controlling the many-body behavior of the Rydberg atoms. The systematic parameters which affect the presence and degree of many-body interactions include state selection, atomic density, and external fields. An experiment performed by our collaborators at the University of São Paulo, described in [39], considered the interactions between pairs of nD Rydberg atoms, where $29 \leq n \leq 41$, at background electric fields of 0.5 V cm^{-1} and 2 V cm^{-1}. State-selective pulsed electric-field ionization was used to determine the populations of Rydberg atoms in the nD and $(n+2)P$ states, by applying a ramped electric field which ionizes the less strongly bound $(n+2)P$ states before the more strongly bound nD states. An $(n+2)P$ signal was observed that was quadratic with the density of the atomic sample, indicating a two-body process. The $(n+2)P$ signal changed significantly when n was varied and when the electric field was varied.

To explain the experimental results, we calculated potential curves for states nearby the $nD + nD$ pair states, for $29 \leq n \leq 41$, and then performed an analysis on the potentials using the classical Landau-Zener approximation.

3.2.1 Potential calculation

The potential calculations were performed at two electric fields, 0.5 V cm^{-1} and 2 V cm^{-1}, for states around the $nD + nD$ asymptotes, where $29 \leq n \leq 41$. The potential curves for the two fields at $n = 37$ are shown in Fig. 3.1. The $nD + nD$ potential curves are close in energy to $(n + 2)P + (n - 2)L$ pair states, where $L \geq 3$.

The calculations for the potentials include dipole-dipole, dipole-quadrupole, and quadrupole-quadrupole interactions. To test the relative importance of the quadrupole terms, a set of potential curves was calculated considering only dipole-dipole terms. A comparison for $37D + 37D$ at 2 V cm^{-1} is shown in Fig. 3.2. In this case, when the quadrupole contribution is omitted, an avoided crossing that is present in the potentials does not appear. Interactions between the energy levels, represented in the Hamiltonian via off-diagonal terms, result in crossings between the potential curves becoming avoided crossings. Thus, to get the correct result from the Landau-Zener analysis, it is important to include the quadrupolar contributions.

The basis set for the pair state Hamiltonian includes pair states nearby energetically to the $nD + nD$ asymptote. The size of the basis set is selected

to be large enough for convergence, but small enough to fit inside the memory of a node on the supercomputing cluster. The typical basis set size is ~ 5000 states for each M. Because in this case the Hamiltonian is approximately block-diagonal in M, the individual M values can be diagonalized separately, greatly saving on memory usage.

The energy gap between the curves in the avoided crossings is a representation of the strength of the interaction. This can be used to determine the probability of a state-changing interaction, using the Landau-Zener formula.

3.2.2 Landau-Zener analysis

To estimate the probability of state-changing interactions, we used the Landau-Zener semi-classical approximation. Because the timescale of the experiment is very short, (~ 100 ns), the atoms are effectively frozen. Thus any state changes are not the result of free-atom collisions, in which two Rydberg atoms approach each other from long distance and collide. However, a pair of atoms excited along the potential at a internuclear separation R near an avoided crossing has a certain probability of changing state via a nonadiabatic transition.

The Landau-Zener transition probability is [45]:

$$P = e^{-2\pi\Gamma}, \tag{3.1}$$

where

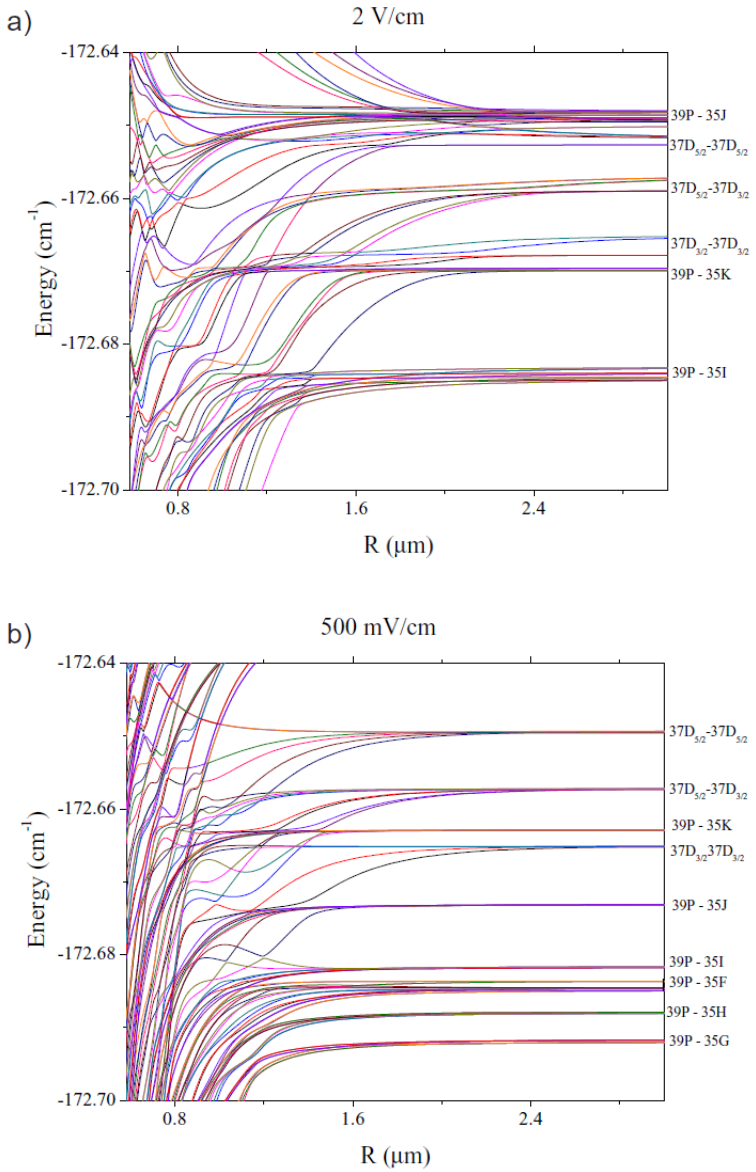

Figure 3.1: Pair potential curves around $37D + 37D$, $M = 0$, in ^{87}Rb85 at electric field of a) 2 V cm^{-1} and b) 0.5 V cm^{-1}.

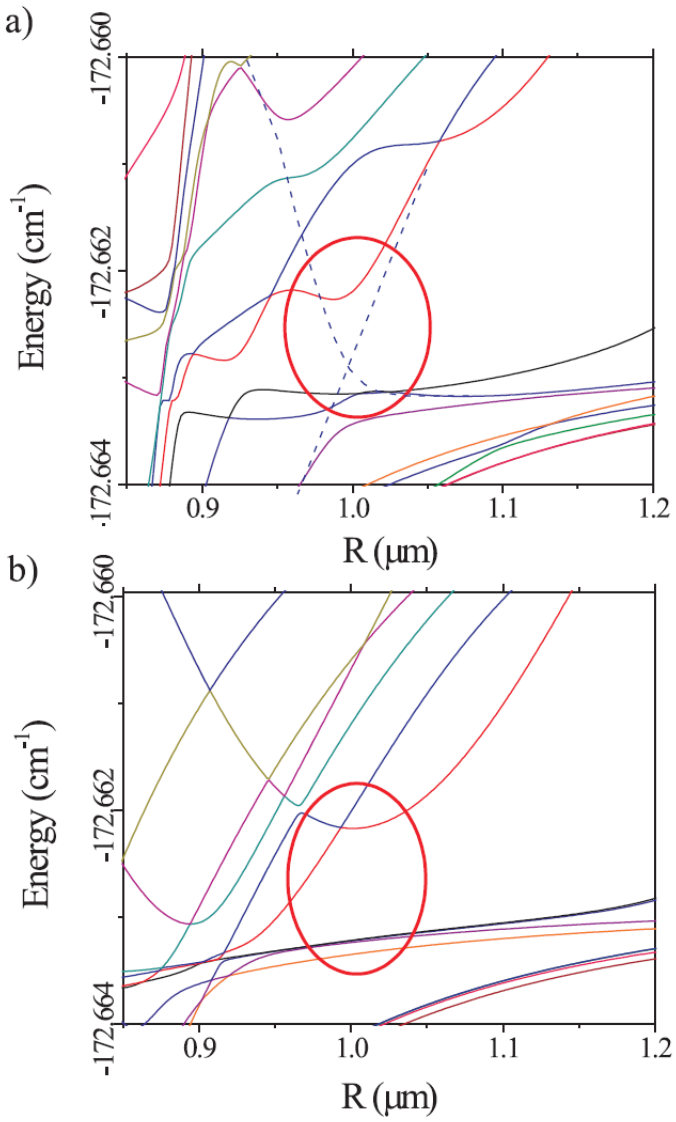

Figure 3.2: Pair potential curves around $37D + 37D$, $M = 0$, in ^{87}Rb85 at electric field of 2 V cm^{-1} a) with dipole-dipole, dipole-quadrupole, and quadrupole-quadrupole contributions included, and b) with dipole-dipole contributions only. The diabatic curves marking the crossing are shown in dotted lines. This avoided crossing is absent in (b).

$$\Gamma = \frac{\Delta E^2}{\left|4\hbar\frac{dR}{dt}\partial(E_2 - E_1)/\partial R\right|}, \tag{3.2}$$

ΔE is the energy gap between the potential curves at the avoided crossing, and $\partial(E_2 - E_1)/\partial R$ is the difference between the slopes of the diabatic (crossing) potentials. The velocity dR/dt used in the calculation is the kinetic energy at the crossing point assuming an excitation near the dissociation limit.

The crossings were located and their transition probabilities computed using an computer search algorithm which detected avoided crossings by checking for points where the potential curves make close approaches. The algorithm was checked using two methods. First, transition probabilities at avoided crossings were calculated manually and compared to the results from the program. Second, the number of states included in the calculation was varied to ensure that enough states were included for the calculation to converge. One difficulty of using the search algorithm is that it may miss avoided crossings in regions where there are non-interacting potential curves located energetically between the interacting potential curves. Such avoided crossings must be calculated manually. An additional assumption made in the calculation is that a single Landau-Zener transition is made. This assumption is valid due to the short timescales in the experiment.

For a pair of atoms to be excited in the correct range for the interaction to occur, there must be a nearest neighbor pair within that range. The probability of finding a nearest neighbor within that range P_{nn} can be expressed as:

$$P_{nn} = \int_{R_{min}}^{R_{max}} 4\pi\rho R^2 e^{-4\pi R^3\rho/3} dR, \tag{3.3}$$

where R_{min} and R_{max} are the nearest and farthest distances at which the transitions can occur and ρ is the density of ground-state atoms in the MOT.

3.2.3 Results

The number of $(n+2)P$ atoms resulting from Landau-Zener transitions, $N_{(n+2)P}$, can be obtained from the expression:

$$N_{(n+2)P} = \sum_i \frac{P_{\text{react}}^{(i)} P_{nn} N_{gs}}{16}, \tag{3.4}$$

where N_{gs} is the number of ground state atoms in the excitation volume and $P_{\text{react}}^{(i)}$ is the Landau-Zener probability at the ith avoided crossing. The factor of 16 comes from the assumption that the transition into the $nD + nD$ pair state is saturated. For an incoherent excitation of one atom to the Rydberg state, 1/4 of the population is transferred. For two atoms, the result is an overall probability of 1/16. This can then be used to obtain a two-body collision parameter K by the expression (derived from Eq. 14.28 in [22])

$$K = N_{(n+2)P} \frac{R_0^2}{2} v_0, \tag{3.5}$$

where R_0 is the internuclear separation at the first avoided crossing and v_0 is the velocity at the first avoided crossing. The results from this calculation can be seen in Fig. 3.3. There is very good agreement between experiment and theory,

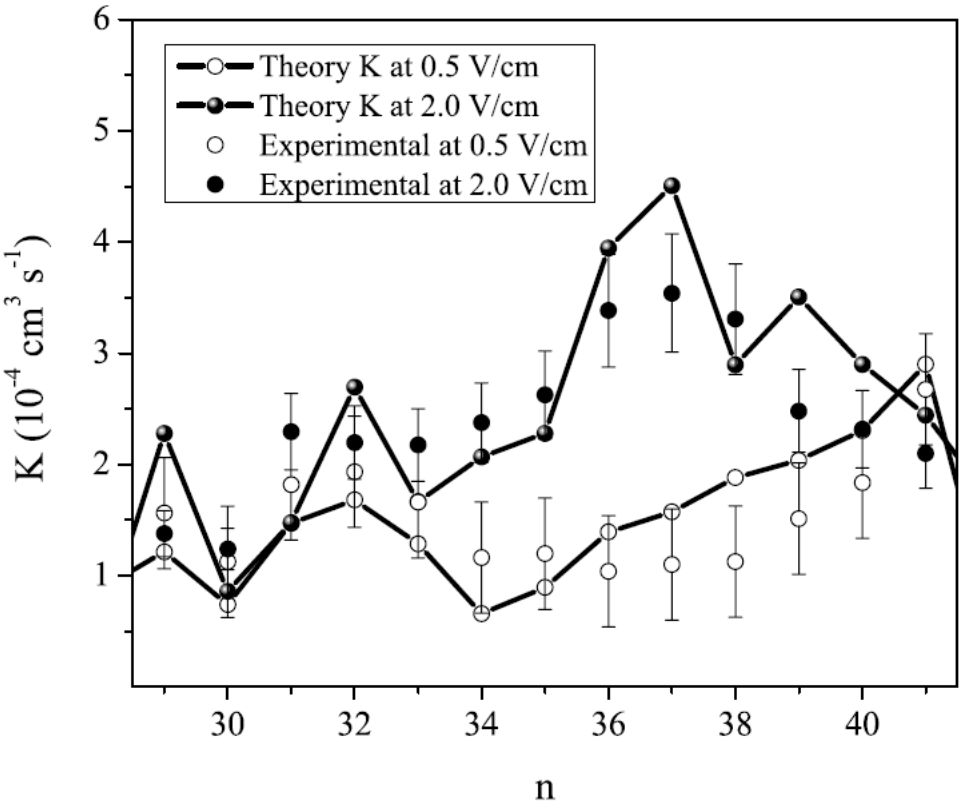

Figure 3.3: Experimental and theoretical two-body collision parameter K at 0.5 V cm^{-1} and 2 V cm^{-1}, for $29 \leq n \leq 41$.

especially considering the lack of adjustable parameters in the theory. With an electric field of 2 V cm^{-1}, the $nD + nD$ and $(n+2)P + (n-2)L$ asymptotes pass each other at $n = 37$, resulting in a peak in the collision parameter.

To summarize, the model using the Landau-Zener method was able to reproduce the experimental results, indicating that the multichannel nature of the interaction cannot be neglected. Additionally, the interactions considered are two-body, rather than many-body in nature, as indicated by the quadratic dependence of the signal on the density of the sample, and the ability of the pair

potential model to describe the results.

3.3 Anisotropic Interactions in Cs

In large electric fields, the anisotropic nature of the Rydberg-Rydberg pair interaction becomes very significant, with amplitudes on the order of 100 MHz. While some anisotropy is present at smaller fields, the impact parameters average out the effect, with the exceptions of particularly sensitive measurements, or measurements in restricted geometries such as in [44]. Anisotropic interactions can give rise to interesting effects in Rydberg atom systems, including the appearance of new phases in a quantum gas or lattice of Rydberg atoms [46, 47].

The calculation of potential surfaces for anisotropic Rydberg interactions presents several computational problems not present in the isotropic case due to the Hamiltonian no longer being block-diagonal in the total projection of the angular momentum along the internuclear axis, as described in Sec. 3.3.1. These issues result in the calculation being significantly more computationally-intensive.

The potential surfaces calculated according to the method described in Sec. 3.3.1 are then used to do a scattering calculation to determine angularly-dependent cross sections for state-changing collisions, as described in Sec. 3.3.2.

3.3.1 Potential calculation

When the electric field axis is not parallel to the internuclear axis, the pair-state Hamiltonian must be rotated to align its z-axis with the electric field axis. Alternatively, the coordinate system for the atomic wavefunctions can be rotated to fall along the internuclear axis, but the former method is used because it is more convenient, giving useful information about the atomic states in the Stark basis. The angular dependence of the Hamiltonian is in the form of spherical harmonics, which can be rotated using the identity:

$$Y_l^m(\theta,\phi) = \sum_{m'} D^l_{m'm}(\Theta,\Phi,\Xi) Y_l^{m'}(\theta',\phi'), \tag{3.6}$$

where D is the Wigner rotation matrix, which depends on the Euler angles. For this case, Θ is the angle between the electric field and the internuclear axis.

This expression does not mix the l terms, which determine whether a matrix element corresponds to a dipole-dipole, dipole-quadrupole, or quadrupole-quadrupole interaction. Thus, these matrices can still be calculated and stored separately. However, the total projections of the angular momentum along the internuclear axis $M = M_{J1} + M_{J2}$ are mixed, and thus the matrix is no longer block diagonal. Thus the basis set must include all M values, which greatly increases the memory usage of the program. The basis set for the calculations is ~ 50000 states. The matrices for this basis set require ~ 60 GB of memory, which makes the program too large to fit in the memory of a single supercomputer

node. Thus the matrices must be split across multiple nodes, which makes the calculation much slower as the nodes are required to communicate with each other to perform a diagonalization of the matrix.

Potential calculations were performed for $nD + nD$ pair states with n =50, 70, 89, and 90, at a field of 100 mV cm^{-1}. The potentials for the $nD_{5/2} + nD_{5/2}$ states are shown as contour plots in Fig. 3.4. For $n = 50$, the field is well below the level needed to have a significant anisotropic dipole-dipole interaction, and thus the anisotropy is very small. As n is increased, the anisotropy becomes more significant. This can be seen in the $90D_{5/2}$ potential, where the dipole-dipole interaction varies by 250 MHz as a function of the angle Θ between the internuclear axis and the electric field axis at a distance of 6 μm.

At small internuclear distances, there are perturbations in the dipole-dipole interaction appearing in the potential surfaces. These are due to avoided crossings between the potential surface and other neighboring potential surfaces. At these avoided crossings, state-changing interactions are possible. To investigate these interactions, we performed a scattering calculation on these potential surfaces.

3.3.2 Scattering calculation

In the scattering calculation, we consider a system of two Rydberg atoms on the potential surface calculated using the method described above. They have a certain probability of changing into another pair state due to interactions between the potential surfaces. Thus the calculation must consider a number

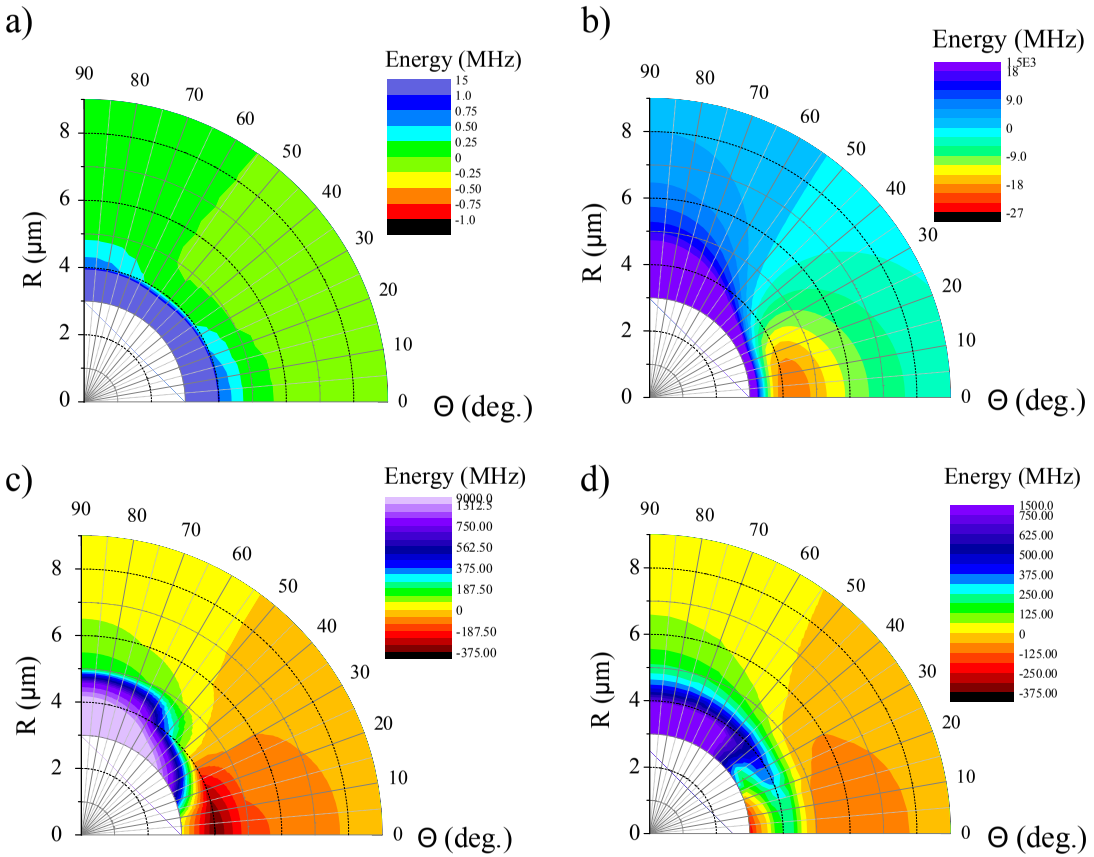

Figure 3.4: Contour plot of the $nD_{5/2}(m_j = 5/2) + nD_{5/2}(m_j = -5/2)$ potential for a) $n = 50$, b) $n = 70$, c) $n = 89$, and d) $n = 90$. As n increases the magnitude of the anisotropic interaction increases. The perturbations in the dipole potential at small R are due to avoided crossings in the potentials.

of coupled channels, N_{prop}, which must be propagated through the scattering interaction.

For the scattering interaction, it is assumed that the excitation occurs at long range and the atoms move along the potential surface, interacting with each other. The propagation in space is done using the Smooth Variable Discretized Enhanced Renormalized Numerov method (SVD-ERN), described in [48].

Using the R matrix calculated using the SVN method, it is possible to calculate the reactance matrix K using the expression (from Eqn. 122 in [49]):

$$K = (RF - B)^{-1} (RE - A), \tag{3.7}$$

where A, B, E, and F are matrices calculated from the rotational wavefunction $\upsilon(\theta_D; \rho)$ and the vibrational wavefunction $\xi(s_f)$ by the expression (from Eqns. 116-121 in [49]):

$$A_{fi} = \delta_{\tau_f \tau_i} \delta_{j_f j_i} \delta_{l_f l_i} \rho^{1/2} \int_0^{\pi/2} d\theta_{Df} \upsilon_f^*(\theta_{Df}\rho) a_{ii}(S_f) \xi_i(s_f), \tag{3.8}$$

$$B_{fi} = \delta_{\tau_f \tau_i} \delta_{j_f j_i} \delta_{l_f l_i} \rho^{1/2} \int_0^{\pi/2} d\theta_{Df} \upsilon_f^*(\theta_{Df}\rho) b_{ii}(S_f) \xi_i(s_f), \tag{3.9}$$

$$C_{fi} = \delta_{\tau_f \tau_i} \delta_{j_f j_i} \delta_{l_f l_i} \rho^{1/2} \int_0^{\pi/2} d\theta_{Df} \upsilon_f^*(\theta_{Df}\rho) \left[\cos\theta_{Df} \xi_i \frac{\partial a_{ii}}{\partial S_f} + \sin\theta_{Df} a_{ii} \frac{\partial \xi_i}{\partial s_f} \right], \tag{3.10}$$

$$D_{fi} = \delta_{\tau_f \tau_i} \delta_{j_f j_i} \delta_{l_f l_i} \rho^{1/2} \int_0^{\pi/2} d\theta_{Df} \upsilon_f^*(\theta_{Df}\rho) \left[\cos\theta_{Df} \xi_i \frac{\partial b_{ii}}{\partial S_f} + \sin\theta_{Df} b_{ii} \frac{\partial \xi_i}{\partial s_f} \right], \tag{3.11}$$

$$E = \frac{1}{2\rho} A + C, \tag{3.12}$$

$$F = \frac{1}{2\rho} B + D. \tag{3.13}$$

In these expressions, the scale of the system is expressed by the radius ρ, which in the two-body system is simply the internuclear distance R. The elements of the matrices a and b are proportional to the spherical Bessel functions j_l and y_l.

3.3.3 Results

Results of the scattering calculation are shown for the $89D_{5/2} + 89D_{5/2}$ system on three different axes in Figs. 3.5, 3.6, and 3.7. The three internuclear axes presented in the figures are parallel to, 57.4° from, and perpendicular to the electric field axis. The 57.4° angle is of interest because that is the angle at which the anisotropic dipole-dipole interaction, which is of the form $3\cos^2(\Theta) - 1$,

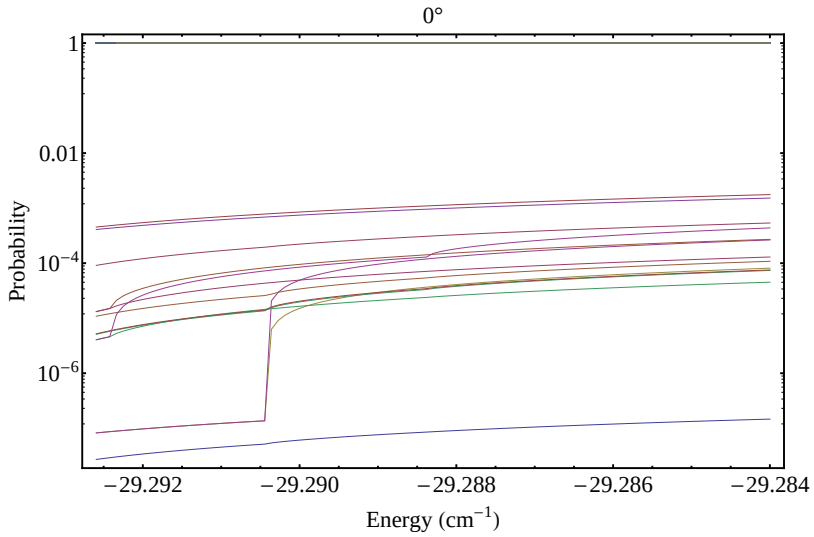

Figure 3.5: State-to-state transition probabilities for various states in the $89D_{5/2} + 89D_{5/2}$ manifold as a function of scattering energy along an internuclear axis parallel to the electric field axis.

is minimized. The graphs present for each axis the state-to-state transition probabilities for each sublevel of the $89D_{5/2} + 89D_{5/2}$ manifold.

A strong resonance is present in the probability at 57.4° at -29.2915 cm^{-1}. This energy corresponds to a neighboring $89D_{3/2} + 89D_{5/2}$ threshold. The resonance is narrow in Θ, with a width of $\sim 1°$.

For each of these cases, the transition probability increases as the scattering energy increases, with sudden increases in the probability as thresholds are crossed. The resonance at 54.7° indicates a strong angular dependence to the cross sections, which may be detectable in experiments.

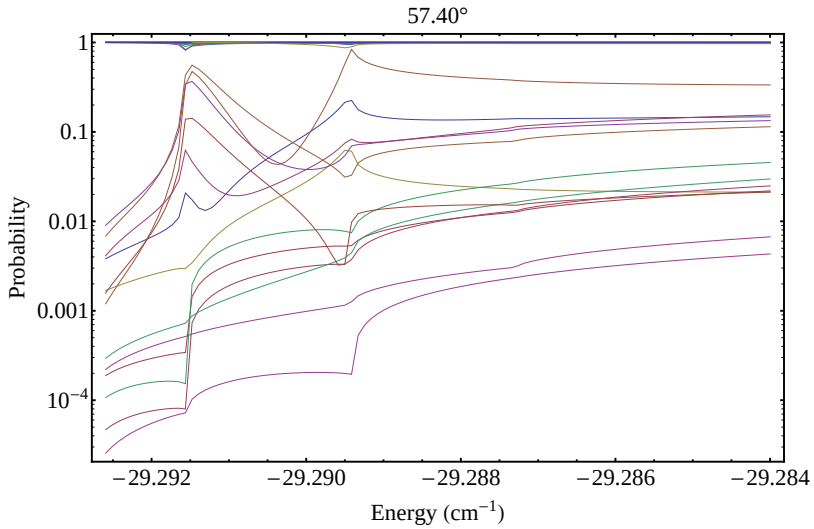

Figure 3.6: State-to-state transition probabilities for various states in the $89D_{5/2} + 89D_{5/2}$ manifold as a function of scattering energy along an internuclear axis 57.4° from the electric field axis. This angle is chosen because it is where the dipole-dipole interaction is minimized. The strong resonance at $-29.2915\ \mathrm{cm}^{-1}$ corresponds to a neighboring $89D_{3/2} + 89D_{5/2}$ threshold.

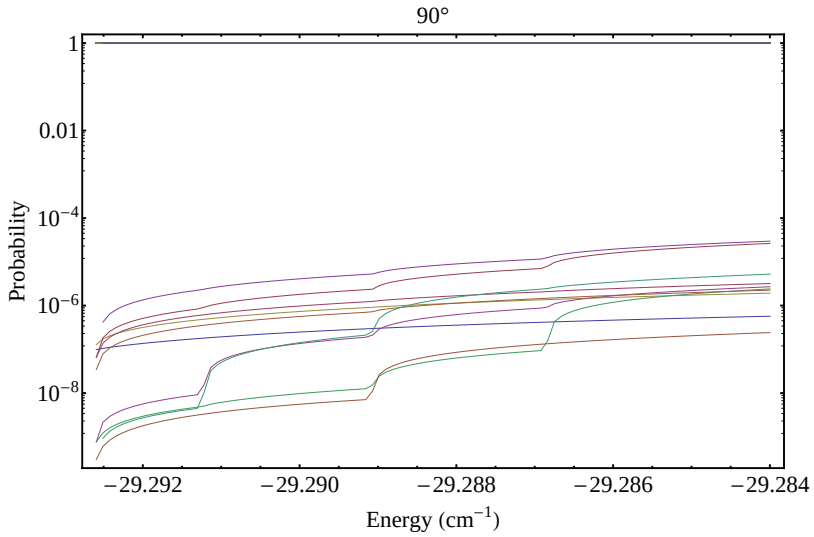

Figure 3.7: State-to-state transition probabilities for various states in the $89D_{5/2} + 89D_{5/2}$ manifold as a function of scattering energy along an internuclear axis perpendicular to the electric field axis.

3.4 Rydberg Aggregations in a Vapor Cell

The experiments discussed thus far have all involved ultracold atoms. However, Rydberg-Rydberg interactions also can be significant in hot atoms as well. [50] discusses an experiment in which Rydberg atoms were excited in a vapor cell. In the vapor cell the atomic sample is room-temperature (300 K), and very dense.

In a dense sample such as this, Rydberg blockade and anti-blockade become very important effects. In Rydberg blockade, a resonant laser cannot excite atoms that are closer than a certain distance (called the blockade radius) from a Rydberg atom, because the multipolar interactions shift the Rydberg line away from the laser's frequency.

Anti-blockade relies on a similar effect to allow off-resonant excitation of Rydberg atoms: at a certain distance, the multipolar interactions can cancel out the detuning of the laser, allowing excitation of pairs of atoms at that distance while preventing excitation of pairs of atoms at other distances. Because this makes the distances between pairs of excited Rydberg atoms controllable, this gives rise to spatial correlations in the positions of the Rydberg atoms.

3.4.1 Results

Potentials and eigenvectors were calculated for states energetically nearby the $32S + 32S$ state in Cs. The potential curves are shown in Fig. 3.8, with colors indicating the eigenvector component of the $32S + 32S$ pair state. At smaller internuclear distances, mixing between the $32S + 32S$ state and neighboring $31P + 31D$ states enables population transfer of $32S$ Rydberg atoms into the $31P$ state.

The bottom graph in Fig. 3.8 shows cross sections of the $32S+32S$ component at various detunings. Because of the multipolar interactions, certain internuclear distances are selected out at these detunings. For example, at -2 GHz detuning, this results in a peak in the $32S + 32S$ component at ~ 0.53 μm, meaning that pairs of atoms will be preferentially excited at this distance.

Because of the overlap between the $32S + 32S$ and $31P + 31D$ components, population transfer will occur into the $31P + 31D$ state. This means that interactions between $32S + 31P$ and $32S + 31D$ pairs must also be considered.

However, because the interactions in the $32S+31D$ pair states are repulsive, they do not lead to pair state excitations for negative detunings because the positive shift in energy does not cancel out the detuning in the laser at any internuclear distance. The $32S + 31P$ pair states are attractive, with an interaction strength of $C_3^{S-P} = -290$ MHz μm^3. This agrees well with the experimental value of -258 MHz μm^3 [50].

3.5 Electric-field induced transitions to $(n+2)P+(n-2)L$ hydrogenic states in Rb

The experiment described in 3.2 raises the possibility of transitions from $nD+nD$ pair states into $(n+2)P+(n-2)L$ pair states, where $L > 3$, via interactions that are higher-order than dipole-dipole interactions. At a field of ~ 1.65 V cm^{-1}, the asymptote corresponding to $39P + 35(L = 12)$ is nearly degenerate with the $nD + nD$ pair state asymptote, allowing strong interactions which can result in population transfer. In the experiment a significant transfer of population into the $(n+2)P$ state was observed. To explain this population transfer we calculated potential curves for the $37D + 37D$ system at fields around 1.65 V cm^{-1} and performed an analysis on these potential curves to determine expected lineshapes at various ground state atomic densities.

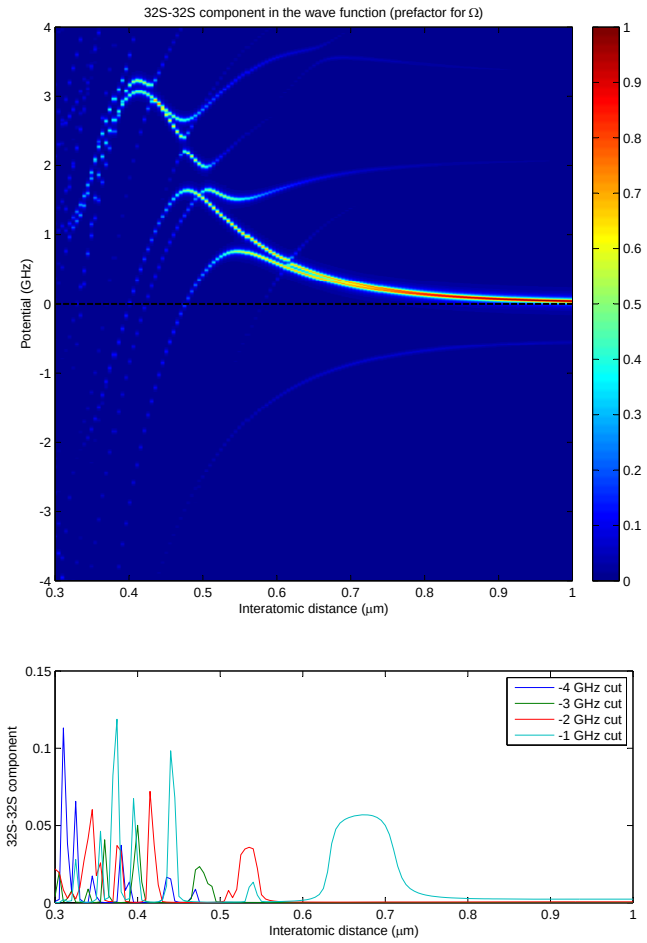

Figure 3.8: Top: Potential curves around $32S + 32S$, with shading indicating the magnitude of the $32S + 32S$ component. Bottom: Cross sections of the $32S + 32S$ component at various detunings below the $32S$ atomic resonance.

3.5.1 Potential calculation

The potential calculation for this system must include all L states up to $L = (n-1)$. As a result, the matrices for the angular terms which are used for the pair-state Hamiltonian are much larger than in calculations which use a basis which is truncated in L. These matrices are large enough that they no longer fit in memory, and thus the program must be modified. An advantage, however, of using a basis with such a large number of L values included is that most of the elements of the matrix correspond to transitions which are dipole-forbidden, and as a result have an angular matrix term of zero. Because of this the matrix can be represented in sparse form. While this does increase the time required for the program to look up a matrix element, it allows the matrix to be easily fit in the RAM of a single supercomputer node without requiring more time- and memory-costly measures such as Scalapack.

To implement this change, the Mathematica notebook was modified to output the matrices in sparse form as a table in which each row corresponds to a non-zero matrix element where the columns are the row, column, and value of the element. The Fortran program imports this table and uses it to define the non-zero elements of the sparse matrix. A lookup subroutine was written which uses the binary search algorithm to find a given element in the table. It is important to note that the Mathematica notebook sorts the elements by column and row. This sorting is necessary for the binary search to work, and if the

elements are given out of order the search algorithm will fail.

For the $37D + 37D$ system we calculated potentials and eigenvectors at fields varying from 1.6 V cm^{-1} to 1.7 V cm^{-1} in intervals of 0.025 V cm^{-1}. At each of these fields we used the potentials and eigenvectors to calculate a lineshape for the $37D$ and $39P$ signal.

3.6 Analysis and Results

The equation used for determining the lineshape is based on Eqn. 36 from [51]:

$$\alpha(E) = \frac{\rho e^2 \pi}{4c\epsilon_0 m_e} \sum_{a=1}^{3} \frac{\sigma/2\pi}{\sigma^2 + (E_{dd_a} - E)^2} \int_0^\infty \sum_{i}^{\text{all states}} P_{pair}(R) p_i(R) R^2 \mathrm{d}R, \quad (3.14)$$

where E_{dd_a} is the asymptotic energy for the $37D_{5/2} + 37D_{5/2}$ pair state and ω is the single-photon Rabi frequency. e is the charge of the electron, and m_e is the mass of the electron. Since there is an applied electric field, the m_J sublevels of $37D_{5/2} + 37D_{5/2}$ split, and so we account for the three asymptotes with the sum over the asymptotes a. E is the energy of the photon, σ is the linewidth including the laser linewidth as well as the linewidth of the $5P_{3/2}$ state, P_{pair} is the pair-state correlation function

$$P_{pair} = \int_0^R 4\pi\rho R'^2 e^{-4\pi\rho R'^3/3} dR', \quad (3.15)$$

and $p_i(R)$ is the excitation probability into the states corresponding to the asymptotes E_{dd_a}. For the P state yield, the excitation probability contains an

additional term indicating the overlap between the $D + D$ state and the $P + L$ state: $p_i(R) = p_P(R)p_D(R)$.

At the laser intensities and densities used in the experiment, saturation must be considered. The lineshape with saturation is [52]

$$\alpha_{sat}(E) = \frac{\alpha(E)}{1 + S_E}, \tag{3.16}$$

where

$$S_E = \eta(\rho)\frac{B_{12}\rho_s(E)}{\Gamma}L(E_{dd_a} - E), \tag{3.17}$$

B_{12} is the Einstein coefficient of induced absorption, $\rho_s(E)$ is the spectral energy density of the excitation light, Γ is the mean relaxation rate, $\eta(\rho)$ is the hard sphere model parameter [53], and

$$L(E_{dd_a} - E) = \alpha(E)\frac{4c\epsilon_0 m_e}{\rho e^2 \pi} \tag{3.18}$$

is the lineshape function, proportional to $P_{exc}(E)$. The density-dependent hard-sphere model treats the system as containing spheres around the Rydberg atoms in which further excitation is forbidden, thus limiting the number of Rydberg atoms that can be formed from a high ground-state density sample.

Figs. 3.9–3.13 show the potential curves for the $37D + 37D$ system at electric fields of 1.600 V cm^{-1}, 1.625 V cm^{-1}, 1.650 V cm^{-1}, 1.675 V cm^{-1}, and 1.700 V cm^{-1}, with a ground state density of 5×10^{11} cm^{-3}. The magnitude

of the eigenvector component corresponding to the $37D + 37D$ pair state is indicated by the shading of the lines, with darker shading indicating a larger component. These potentials were used to calculate a lineshape, shown on the right section of each figure. The lineshape agrees well with the experimental results, which were taken at a field of 1.65 V cm^{-1}. The states surrounding the $37D + 37D$ pair states are $39P + 35(L = 12)$ pair states. The calculated output and experimental output is indicated for $37D$ atoms (in red) and $39P$ atoms (in blue).

Fig. 3.14 shows the experimental and calculated yield of $39P$ atoms as a function of electric field with a constant excitation laser detuning of 0 MHz at densities of 2×10^{10} cm^{-3}, 6×10^{11} cm^{-3}, 1.2×10^{12} cm^{-3}, 1.8×10^{12} cm^{-3}, 2.4×10^{12} cm^{-3}, and 3×10^{12} cm^{-3}. As the density is increased, the lines broaden and the yield saturates to a fractional transfer of ~ 0.4 . This is due to the dipole blockade: as the atom spacing is reduced, more of the potential curve becomes accessible, causing excitation to occur at a larger range of electric fields when the excitation energy is held constant.

3.7 Conclusion

In summary, the pair potential calculation methods presented above have been shown to be useful in various Rydberg atom systems. In the ^{85}Rb $nD + nD$ experiment described in Sec. 3.2, a fairly simple classical model using the

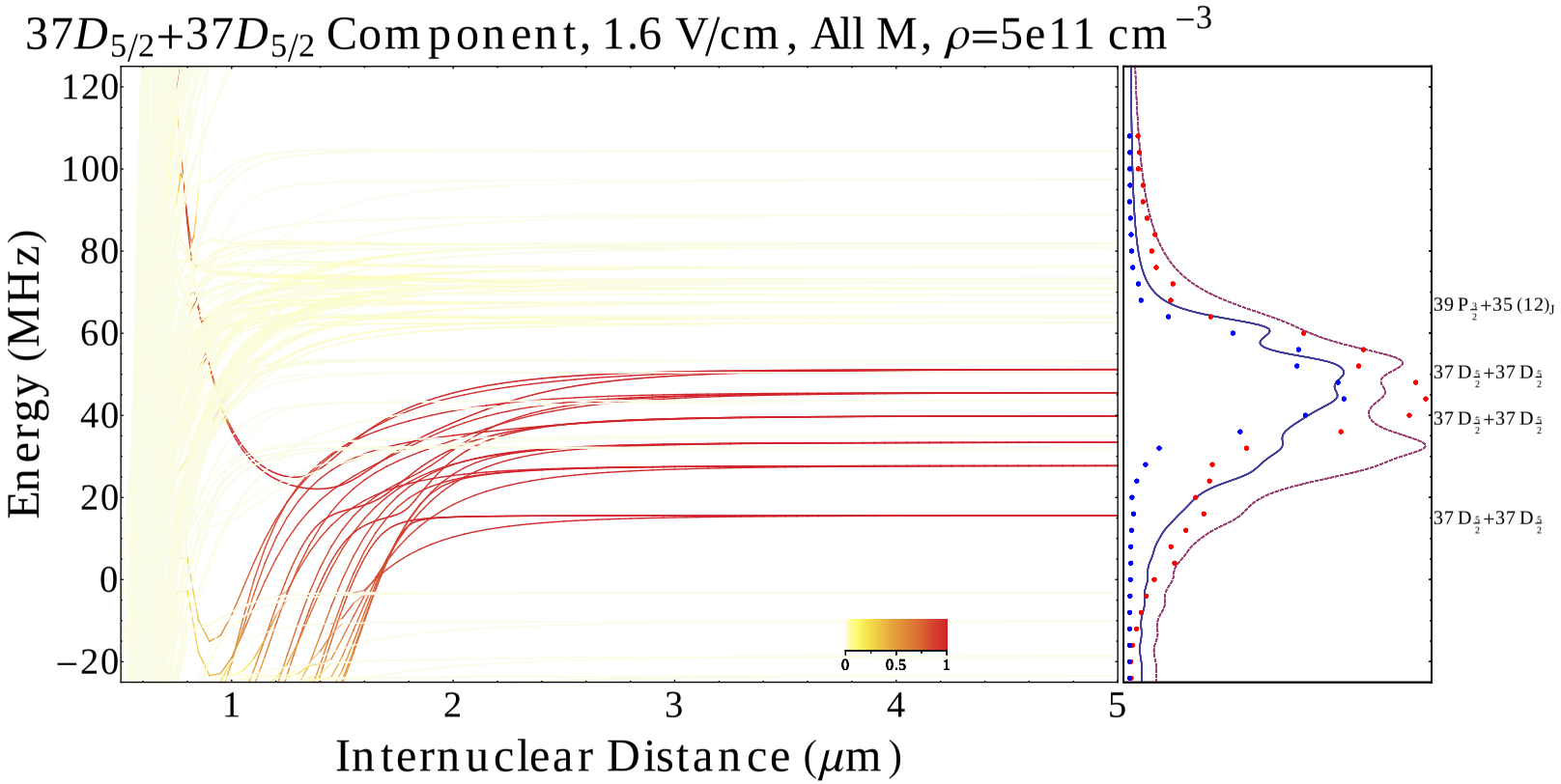

Figure 3.9: Left: Potential curves near the $37D_{5/2} + 37D_{5/2}$ asymptote in an electric field of 1.6 V cm^{-1}. Darker color indicates larger $37D_{5/2} + 37D_{5/2}$ component. Right: Calculated yield of $37D_{5/2}$ atoms (red points are experimental data, red line is calculated spectrum), and calculated yield of $(n-2)P$ atoms (blue points are experimental data, blue line is calculated spectrum).

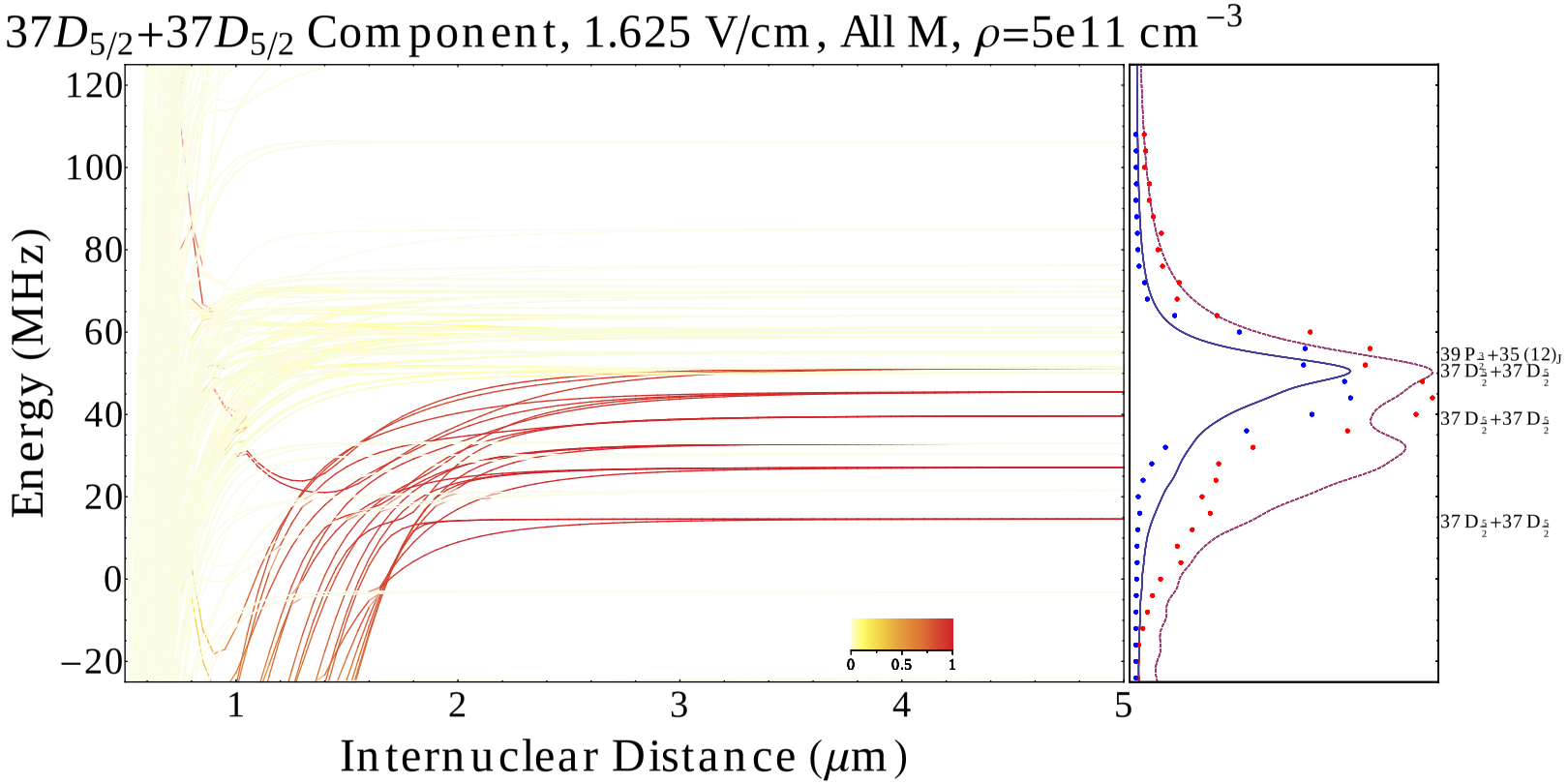

Figure 3.10: Left: Potential curves near the $37D_{5/2}$+$37D_{5/2}$ asymptote in an electric field of 1.625 V cm^{-1}. Darker color indicates larger $37D_{5/2} + 37D_{5/2}$ component. Right: Calculated yield of $37D_{5/2}$ atoms (red points are experimental data, red line is calculated spectrum), and calculated yield of $(n-2)P$ atoms (blue points are experimental data, blue line is calculated spectrum).

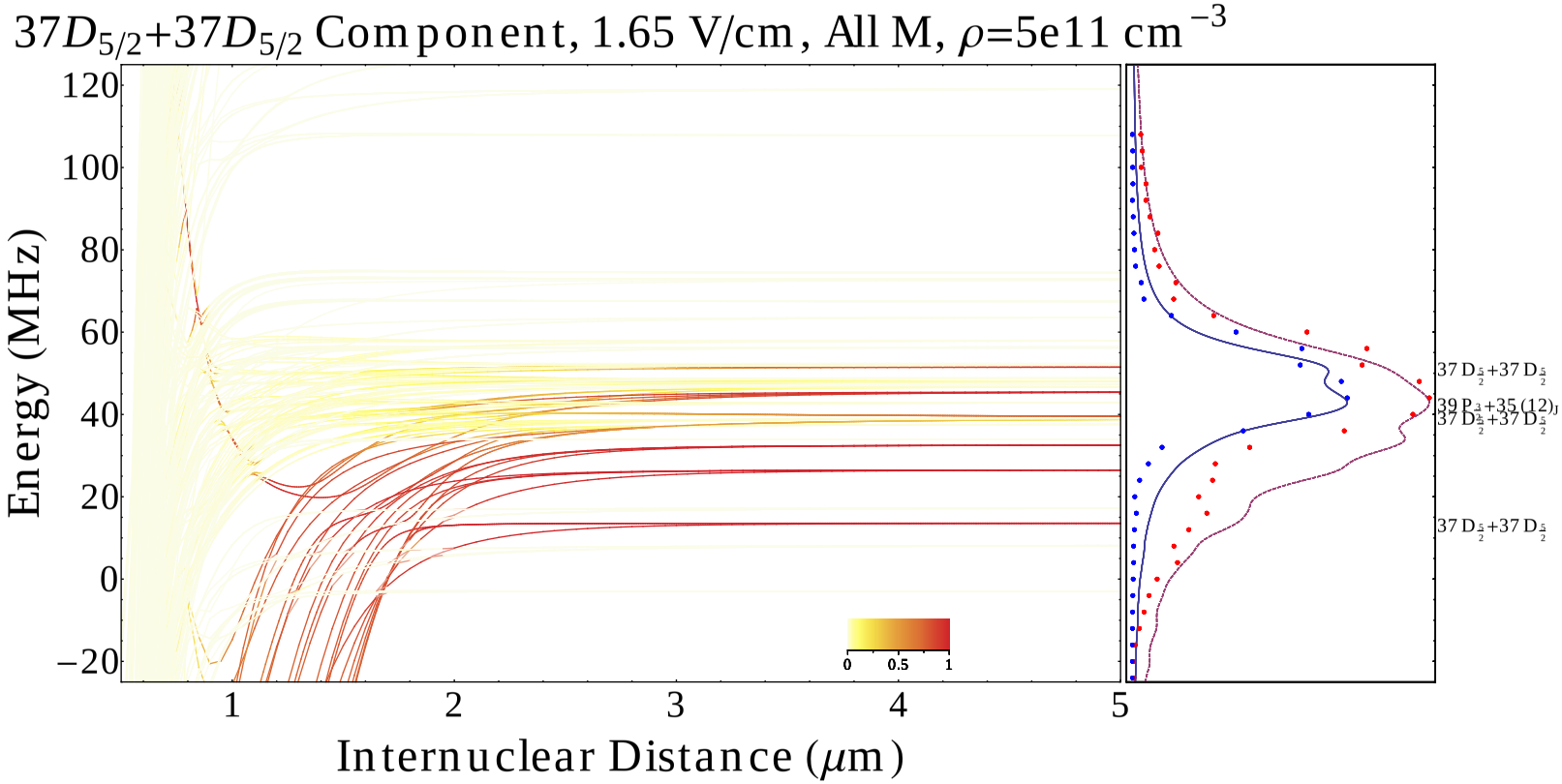

Figure 3.11: Left: Potential curves near the $37D_{5/2}+37D_{5/2}$ asymptote in an electric field of 1.65 V cm^{-1}. Darker color indicates larger $37D_{5/2}+37D_{5/2}$ component. Right: Calculated yield of $37D_{5/2}$ atoms (red points are experimental data, red line is calculated spectrum), and calculated yield of $(n-2)P$ atoms (blue points are experimental data, blue line is calculated spectrum).

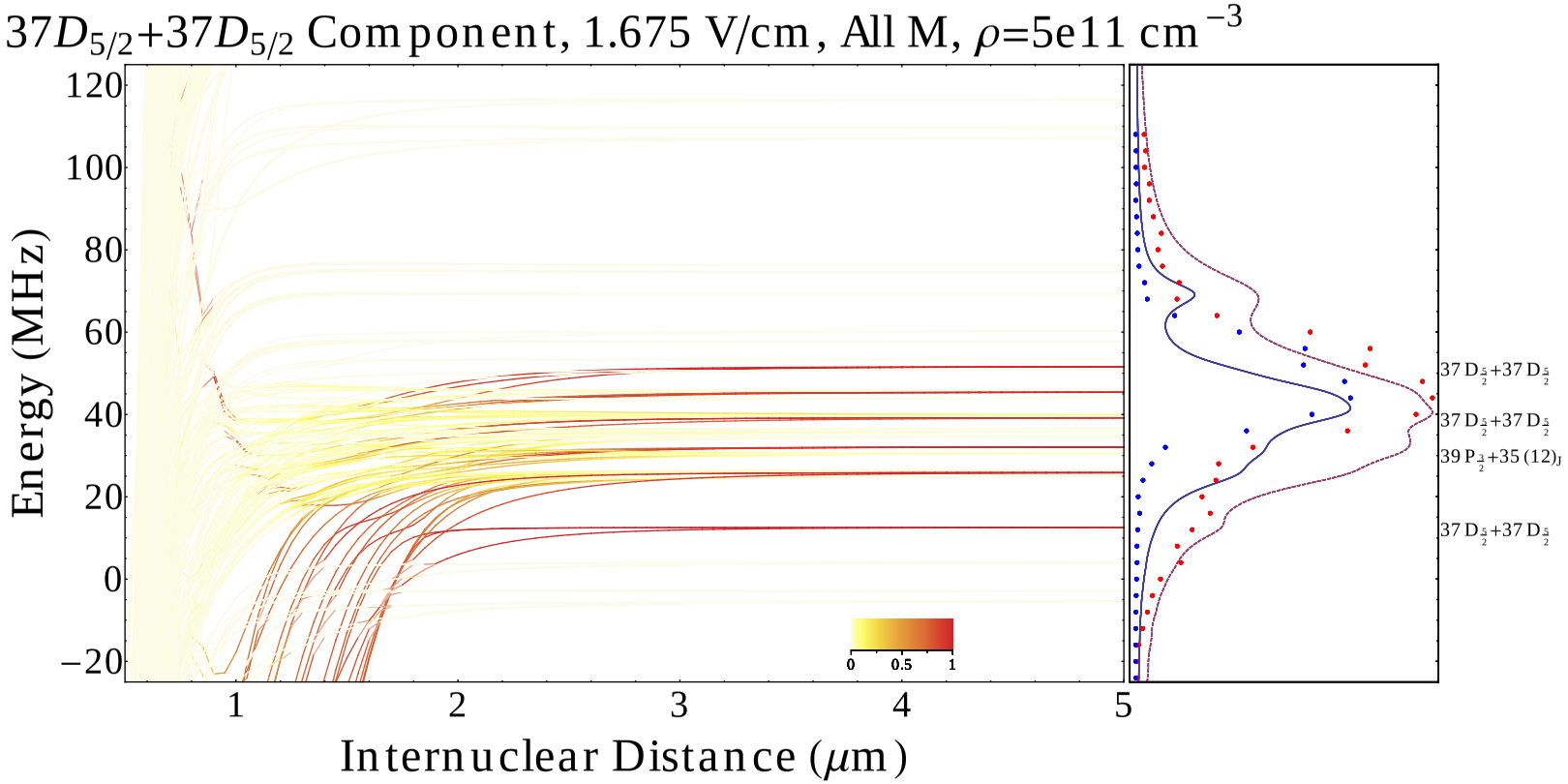

Figure 3.12: Left: Potential curves near the $37D_{5/2}$+$37D_{5/2}$ asymptote in an electric field of 1.675 V cm^{-1}. Darker color indicates larger $37D_{5/2} + 37D_{5/2}$ component. Right: Calculated yield of $37D_{5/2}$ atoms (red points are experimental data, red line is calculated spectrum), and calculated yield of $(n-2)P$ atoms (blue points are experimental data, blue line is calculated spectrum).

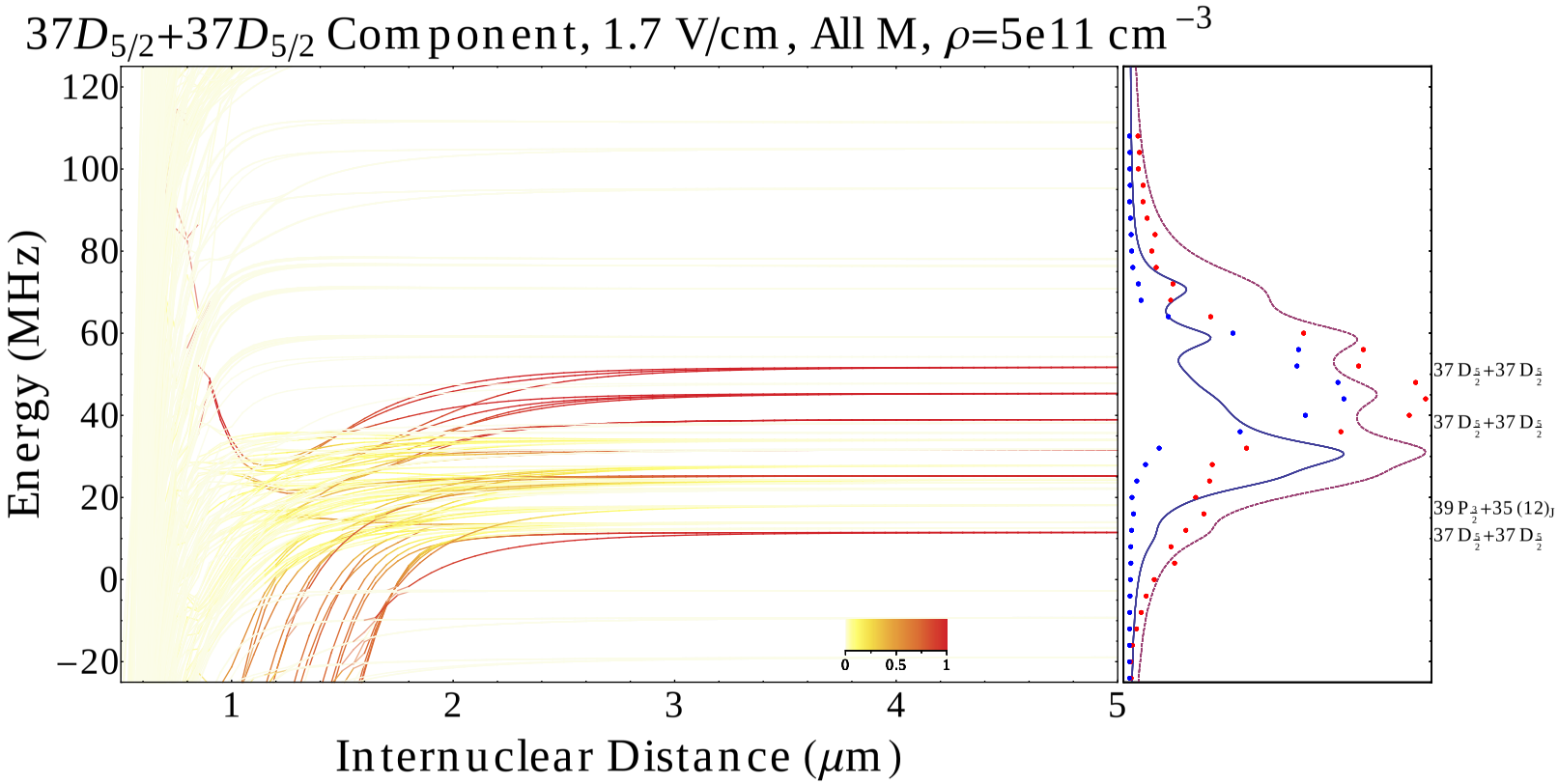

Figure 3.13: Left: Potential curves near the $37D_{5/2} + 37D_{5/2}$ asymptote in an electric field of 1.7 V cm^{-1}. Darker color indicates larger $37D_{5/2} + 37D_{5/2}$ component. Right: Calculated yield of $37D_{5/2}$ atoms (red points are experimental data, red line is calculated spectrum), and calculated yield of $(n-2)P$ atoms (blue points are experimental data, blue line is calculated spectrum).

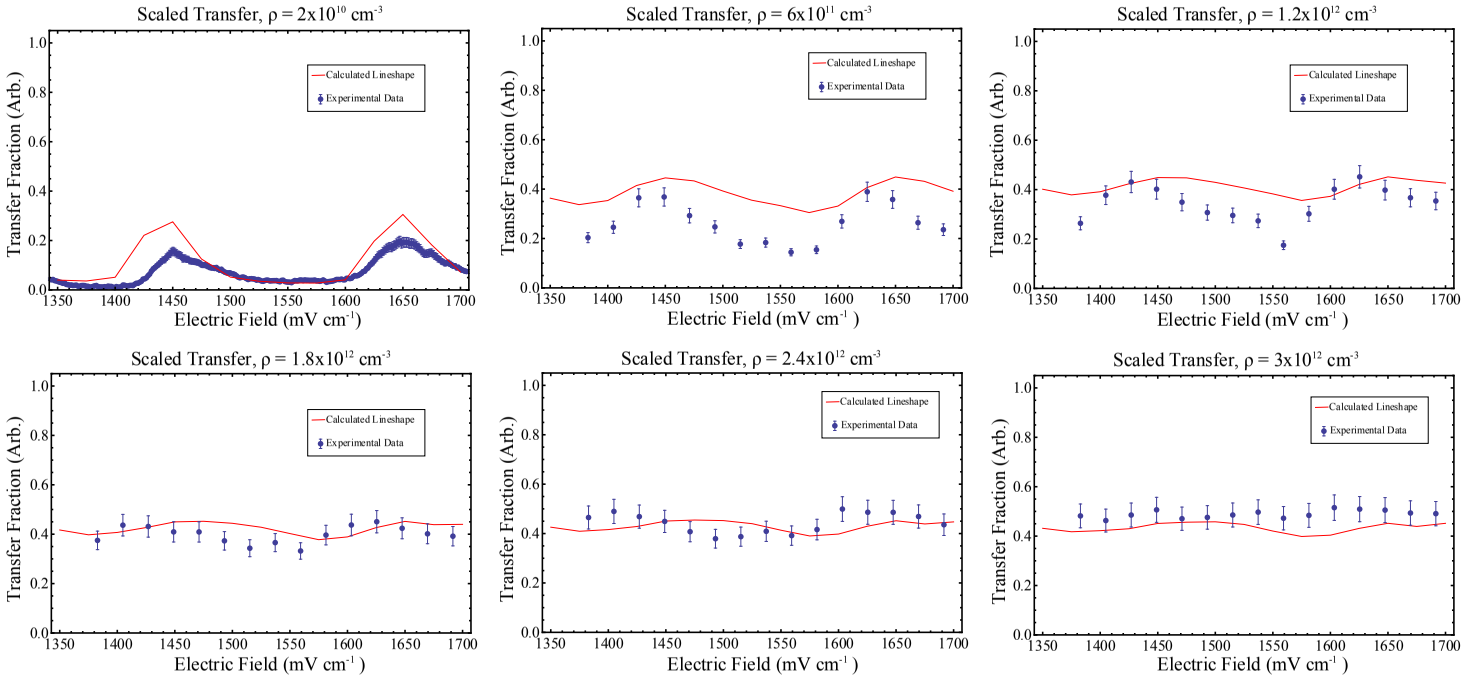

Figure 3.14: Experimental and calculated lineshapes as a function of electric field, with an excitation laser detuning of 0 MHz at densities ranging from 2×10^{10} cm^{-3} to 3×10^{12} cm^{-3}. Two resonances appear in the density range shown; as the field is increased these resonances become saturated.

Landau-Zener method was shown to accurately explain the experimental results for transitions resulting in observation of $(n+2)P$ atoms. In the anisotropic Cs numerical calculations, the method described is able to determine the angular dependence of the potentials and can be used to determine angular-dependent scattering cross sections for the system. In the Cs vapor cell Rydberg aggregation system, pair potentials were used to verify the source of the initially dipole-forbidden states which result from the interactions in the system. Finally, in the ^{85}Rb system described in Sec. 3.5, pair potential calculations were used to explain the lineshapes seen in the experiment and the behavior of the system in an electric field.

By successfully explaining the results of these experiments, these calculations emphasize the importance of pair interactions in Rydberg atom physics. Previously, it was thought that phenomena such as those studied in [39] could only be sufficiently described by many-body interactions. However, the work presented above provides evidence that two-body interactions can describe the behavior of these Rydberg atom systems.

Chapter 4

Experimental apparatus

This chapter describes the experimental apparatus used in our experiments on ultralong-range Rydberg molecules, described in Chapter 5. The structure of the ultra-high vacuum systems used in the experiment is described in Sec. 4.1. The lasers used for Zeeman slowing and magneto-optical trapping of cesium atoms are described in Sec. 4.2 and the magneto-optical trap and dipole trap are described in Sec. 4.3.

After a sample of cesium atoms has been obtained in the dipole trap, they are excited into Rydberg states using the lasers described in Sec. 4.4, and detected using the apparatus described in Sec. 4.6. The timing of the experiments is described in Sec. 4.5.

4.1 Vacuum system

The vacuum system for the main chamber is pumped by a Leybold TMP 350M turbomolecular pump, which is backed by a Varian M2 diffusion pump, which in turn is backed by a Leybold D65B rotary-vane mechanical pump. The base pressure of the mechanical pump at the gauge near the roughing valve is 45 mTorr. Under ordinary operation, with the diffusion pump running, the minimum pressure gauge reading near the diffusion pump is $\sim 5 - 10$ mTorr.

The turbomolecular pump is separated from the main chamber by a gate

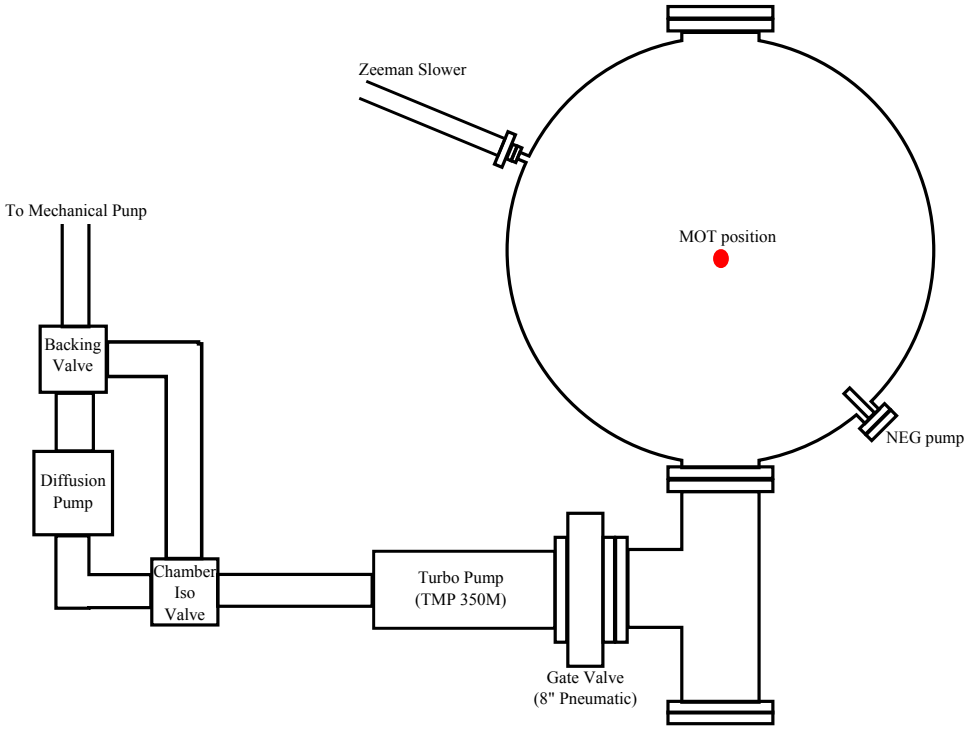

Figure 4.1: A schematic of the vacuum system in the main chamber. The chamber is pumped by the turbomolecular pump, which is backed by the diffusion pump, which is backed by the mechanical pump. Valves allow switching the turbomolecular pump's backing between the diffusion pump and the mechanical pump.

valve. In normal operation the gate valve is kept open, but in the event of a power outage, a programmable logic controller (PLC) closes the gate valve, protecting the chamber from contamination. Two valves located in the lines surrounding the diffusion pump (Fig. 4.1) allow the turbomolecular pump to be backed by either the diffusion pump or the mechanical pump. When the PLC is set to mechanical pump backing, the backing valve bypasses the diffusion pump and the chamber isolation value remains open, allowing the mechanical pump to pump directly on the turbomolecular pump. When diffusion pump backing is selected, the backing valve closes off the bypass, causing the mechanical pump to pump on the diffusion pump. When Chamber Isolation is selected on the PLC, both valves close, isolating the turbomolecular pump from the mechanical pump.

The vacuum system is controlled by a program on the PLC which accepts input from various sources and from a touch panel display. A picture of the touch panel interface is shown in Fig. 4.2. The buttons control various parts of the vacuum system, providing switches for the user to turn pumps on and off, or to open and close valves. The button in the bottom right corner of the screen turns off the backlight. Because the backlight has a limited lifetime, it should be turned off when not in use. The display can be modified using a program available from the manufacturer called "C-More", a screenshot of which is shown in Fig. 4.3. Each button modifies a variable in the memory of the touch panel which is linked to a memory address in the PLC. For example, the "Chamber

Iso OFF" button modifies the variable CHAMBER_ISO, which in turn modifies the memory address C12 in the PLC. For the software to connect to the panel, there must be a USB cable connecting the computer to the panel.

The program on the PLC is controlled by another program, called "DirectSoft32". This program connects to the PLC through a serial cable connection. A screenshot of this program is shown in Fig. 4.4. Once connected, the program on the PLC is shown and its status can be observed. Each line of the program consists of a series of gates which must be "on" for the output address to turn on. There are two kinds of gates: "normally open" and "normally closed." "Normally open" gates are on when the address associated with them is on (for example when an input port is receiving a voltage), and off when the address associated with them is off (when the input port is not receiving a signal). "Normally closed" gates function the opposite way: they are "on" when the address associated with them is "off" and vice versa. "Normally closed" gates are marked on the interface with a diagonal line through them.

4.1.1 Main chamber

The main chamber consists of a spherical vacuum chamber which is connected to the turbomolecular pump via an 8" tee. Attached to the spherical chamber there is a NEG pump (SAES CapaciTorr 400-2) which supplements the pumping of the turbo pump, and a hot-cathode ion gauge. The base pressure in the chamber is $\sim 2 \times 10^{-11}$ Torr. The main chamber contains heating lamps and is wrapped

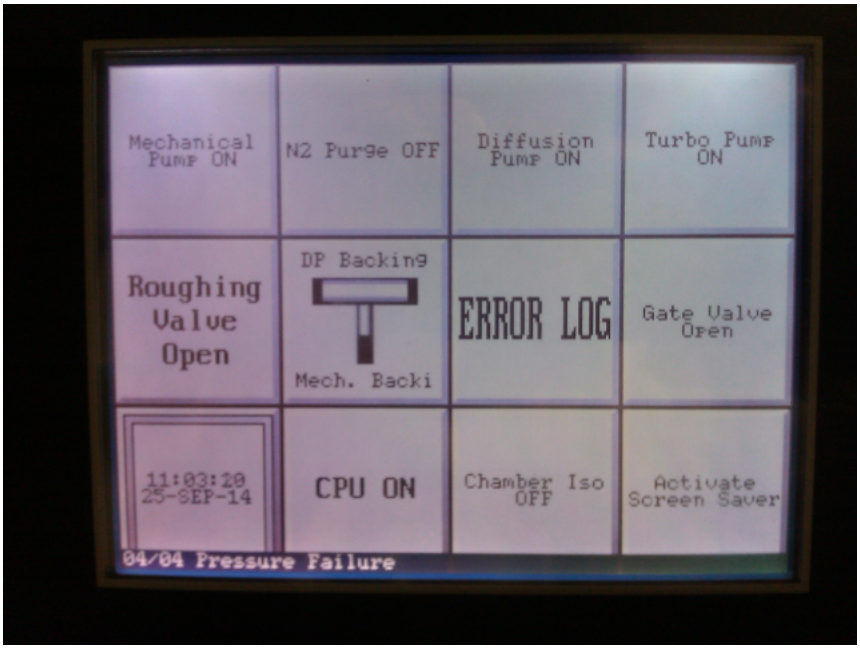

Figure 4.2: Picture of the touch panel interface which controls the PLC in the vacuum system. Various elements of the vacuum system can be controlled using the touch interface.

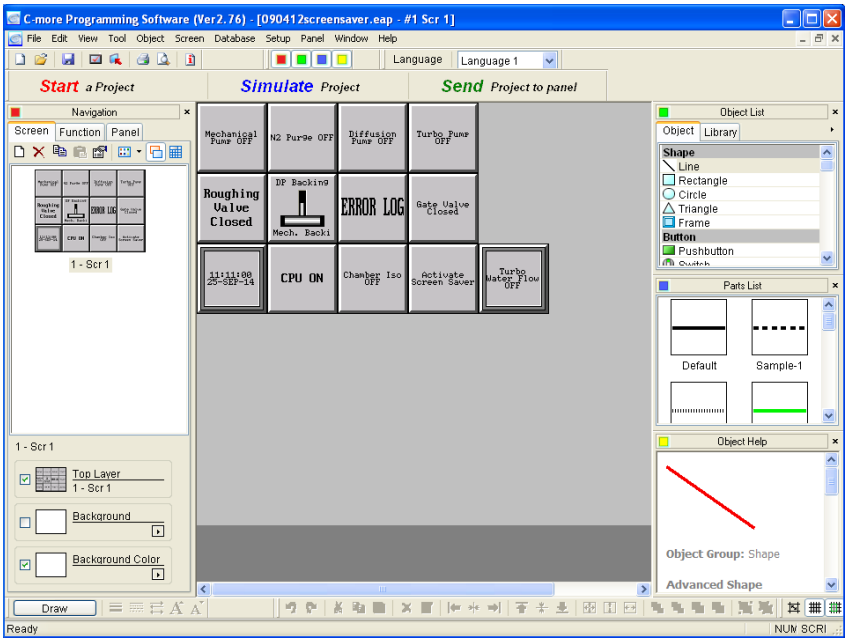

Figure 4.3: Screenshot of the CMore software which allows the touch panel display to be modified. Each button is linked to a variable name, which is linked to a memory address in the PLC.

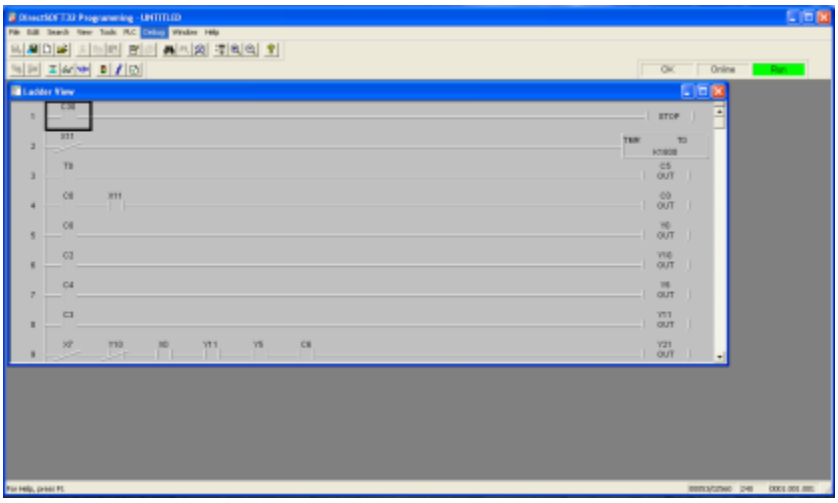

Figure 4.4: Screenshot of the DirectSoft32 software. Each line in the code represents an output channel in the program. The numbers above each item are memory addresses in the PLC. By clicking the Status button (third button in the second row below the menu), the program can show which memory addresses are in the "on" status.

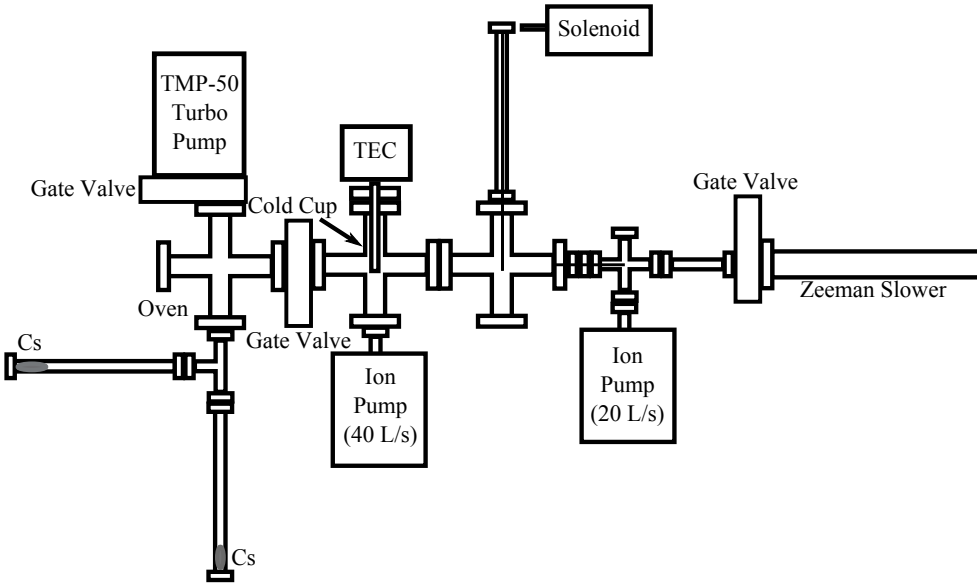

Figure 4.5: Diagram of the Zeeman slower.

with resistive heating tapes to facilitate baking to achieve base pressure.

4.1.2 Zeeman slower

A Zeeman slower is attached to the main chamber through one of the ports on the chamber. A schematic of the slower design is shown in Fig. 4.5. A 3-foot-long 2.75" nipple, wrapped with magnet coil wire is used as the source of the magnetic field for the Zeeman slower. This coil is also used during baking as a heat source. A gate valve (VAT 0132-UE08) separates the slower coil from the rest of the slower apparatus. The gate valve is attached to a 3" flexible coupling,

which allows for alignment adjustments of the atomic beam.

On the other end of the flexible coupling is a 1.33" six-way cross. A 20 Ls^{-1} ion pump is attached to this cross. The cross is attached to a 2.75" 4-way cross and a 2.75" 6-way cross through a 4"-long, 5 mm-diameter differential pumping tube. Another 40 Ls^{-1} ion pump is attached to the 2.75" 6-way cross. Both ion pumps are isolated using baffles with three plates. The baffles are used to decrease the amount of cesium pumped by the ion pumps.

A solenoid-driven mechanical beam shutter is attached to the 4-way cross. It consists of a 6-inch flexible coupling and a rod welded to a blank 1.33" flange. The rod is moved into the atomic beam by a 24 V solenoid, and springs are used to return it to its original position.

A copper cold cup is attached to the 2.75" 6-way cross, acting as a pump for stray cesium inside this section of the Zeeman slower. The temperature of the cold cup is maintained using a thermo-electric cooler (TE Tech CP-036) which keeps the cold cup at $-10\ ^{\circ}\mathrm{C}$. With the cold cup running, pressures in this section of the chamber are dominated by the vapor pressure of the cesium on the cold cup and are typically $\sim 1.0 \times 10^{-6}$ Torr when the oven is hot, and $\sim 1.0 \times 10^{-7}$ Torr when the oven is cold.

The oven of the Zeeman slower is separated from the 2.75" 6-way cross by a gate valve and a 5 mm aperture. The oven consists of a 2.75" cross with a window at the opposite end from the aperture (to facilitate alignment of the atomic beam), attached to two flexible couplings which contain cesium ampoules,

and a gate valve separating the oven from a turbomolecular pump (Leybold TMP50) which is used when baking the vacuum system.

To align the atomic beam to the magnetic field axis, a visible laser is sent through the window in the oven and aligned to the apertures in the Zeeman slower system. If the atomic beam is aligned with the Zeeman slower magnetic field axis, the laser will exit the chamber centered on the input window of the Zeeman slower laser. If this does not occur, the oven section may be mechanically moved (with the flexible coupling preventing motion of the slower tube) until the atomic beam is aligned with the axis.

4.2 Laser systems

Several laser systems are used in the experiments described in this thesis. For cold atom trapping, four lasers are used: trapping and repumping lasers for the MOT, a laser for the Zeeman slower, and a trapping laser for the FORT. The MOT and slower lasers are tuned near hyperfine levels of the $6S_{1/2} \rightarrow 6P_{3/2}$ transition in ^{133}Cs.

The MOT trapping laser is detuned ~ 15 MHz red of the $6S_{1/2}(F = 4) \rightarrow 6P_{3/2}(F' = 5)$ transition. This laser provides the primary cooling mechanism for the MOT, as the atoms cycle on this transition, continually losing energy as they scatter photons. Because there is a detuning from the cycling transition, though, some of the atoms will instead be excited into the $F' = 4$ level, and thus

be able to fall into the $6S_{1/2}(F = 3)$ ground state. These atoms do not absorb light from the trapper laser, and as a result the cooling process stops for these atoms. To prevent these atoms from being lost, a repumping laser is used. This laser is tuned to the $6S_{1/2}(F = 3) \rightarrow 6P_{3/2}(F' = 4)$ transition, and causes atoms to fall back into the $6S_{1/2}(F = 4)$ ground state and reenter the cycling process.

The beam used in the Zeeman slower has two components, one detuned from the $6S_{1/2}(F = 3) \rightarrow 6P_{3/2}(F' = 4)$ by ~ -300 MHz which is derived from the repumper laser, and another detuned from the $6S_{1/2}(F = 4) \rightarrow 6P_{3/2}(F' = 5)$ by ~ -325 MHz which is derived from a separate laser. This laser is used to slow atoms in one dimension as they pass through the Zeeman slower coil. Because the Doppler shift changes as the atoms are slowed, a spatially-varying magnetic field is used to tune the atoms into resonance using the Zeeman effect.

The beam used in the FORT has a wavelength of 1064 nm and is very far detuned from the nearest transition, $6S_{1/2} \rightarrow 6P_{3/2}$, which occurs at 894 nm. As a result, very little scattering of light takes place due to the FORT laser. The trapping force from the FORT laser is instead due to the dipole force, caused by the induced dipoles of the atoms interacting with the radiation field of the laser. The force is proportional to the gradient of the intensity, yielding a conservative potential proportional to the intensity of the laser. To trap atoms effectively, the light must be focused tightly so that the gradient and the intensity at the trap are maximized.

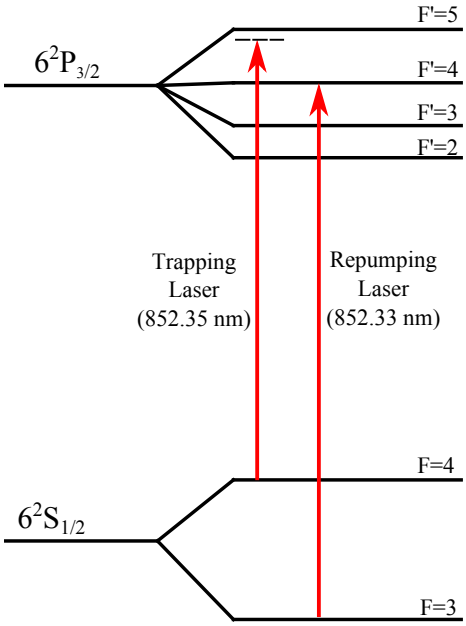

Figure 4.6: Level diagram for the D2 transition ($6S_{1/2} \rightarrow 6P_{3/2}$) in ^{133}Cs.

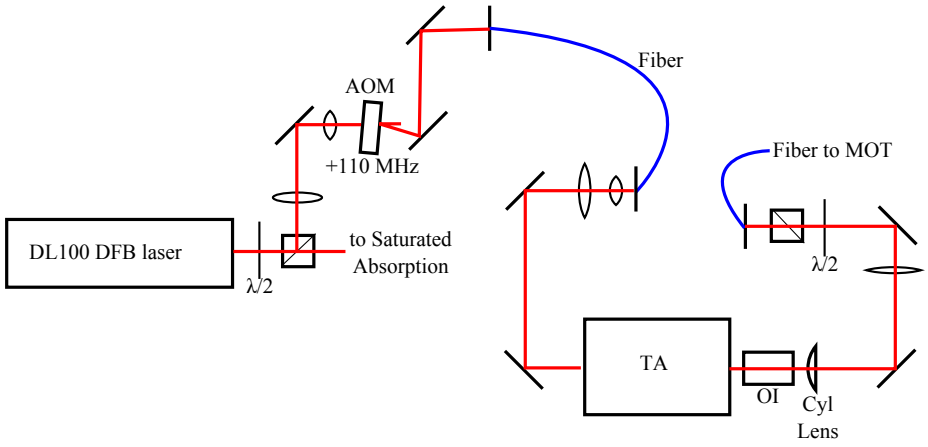

Figure 4.7: Diagram of the trapper laser tapered amplifier alignment. Blue curves represent polarization-preserving single-mode optical fibers.

4.2.1 MOT trapping laser

The MOT trapping laser system consists of an 852 nm diode laser amplified by a tapered amplifier. A schematic of the system is shown in Fig. 4.7.

The diode laser is a Toptica DL100 system configured to use a distributed feedback (DFB) diode. The diode is locked using a Toptica Digilock system to a saturated absorption signal. The Digilock applies a modulation to the diode current and uses a lock-in amplifier to produce a first-derivative signal from the saturated absorption signal. This allows for locking to the top of saturated absorption peaks, which avoids issues with frequency drift due to changes in laser intensity. The laser is locked to the top of the crossover peak between

the ^{133}Cs $6S_{1/2}(F = 4) \rightarrow 6P_{3/2}(F' = 4)$ and $6S_{1/2}(F = 4) \rightarrow 6P_{3/2}(F' = 5)$ transitions. An acousto-optic modulator (AOM) is used to shift the frequency of the light to the MOT trapping frequency, as well as to modulate the intensity of the light. The light is coupled to a single-mode polarization-preserving optical fiber for spatial mode filtering.

A tapered amplifier (Eagleyard Photonics EYP-0850-00500-3006-CMT03) is used to amplify the MOT trapping light, using the DL100 as a seed laser. This amplification allows the laser to be run at a lower current than would otherwise be required, extending the lifetime of the diode. The light emitted from the tapered amplifier (TA) has the same spectral properties as the seed light. The seed laser power at the TA is 15 mW, and the power immediately after the TA is $\sim$ 300 mW. The output is sent through an optical isolator and a single-mode polarization-preserving optical fiber. The output power, which is up-collimated to a diameter of 2 cm and split between the MOT axes, is 100 mW.

The controller for the TA is a Wavelength LDTC 2-2E current and temperature controller. The temperature is set using a trimpot on the controller board, and the current is set using an external potentiometer. A zener diode external to the board is used to limit the current to 1.4 A.

The output mode of the TA has a 3:1 aspect ratio and is highly divergent. To collimate the beam, two lenses are required: an aspheric lens (Thorlabs C230TME-B) which collimates the vertical dimension of the beam, and a 50 mm

cylindrical lens which is used to collimate the horizontal dimension of the beam.

4.2.2 Repumper

The repumper laser is used in the MOT to pump atoms out of the $6S_{1/2}(F = 3)$ ground state, which is inaccessible to the trapping laser, into the $6S_{1/2}(F = 4)$ state. This is done using light resonant to the $6S_{1/2}(F = 3) \rightarrow 6P_{3/2}(F' = 4)$ transition. This light is generated by an external-cavity diode laser (ECDL) system. The diode used in the system is a JDS Uniphase SDL-5401-G1, operating at 852 nm. The grating used to establish the external cavity is a Thorlabs GH-180. A piezoelectric transducer is used to move the grating to allow the frequency of the laser to be tuned. A thermoelectric cooler (Thorlabs TEC3-2.5) is used to control the temperature of the diode. The mount for the laser was machined in the physics department. The current controller is a Thorlabs LDC500, and the temperature controller is a Thorlabs TEC2000.

The repumper is frequency stabilized by dichroic atomic vapor laser locking (DAVLL) [54]. The Zeeman shift due to a constant magnetic field is used to shift the resonance frequencies of orthogonal circular polarizations, and the signals from the two polarizations are subtracted to produce a dispersive signal. A saturating beam counter-propagating with the probe beam is used to produce narrow saturated absorption signals as a reference for laser locking.

The repumper laser is passed through an AOM and copropagated with the MOT beams using a polarizing beamsplitter cube.

4.2.3 Zeeman slower laser

The Zeeman slower system uses an ECDL of similar construction to the repumper laser. Unlike the repumper laser, the controller for this laser is a Wavelength LDTC500. The laser is locked to a saturated absorption DAVLL signal. The laser is locked to the $6S_{1/2}(F = 4) \rightarrow 6S_{1/2}(F = 5)$ transition. The locking is done using a PID loop encoded in a Digilent Nexys 2 Spartan 3-E field-programmable gate array (FPGA) [55].

The output of the Zeeman slower laser is coupled to a single-mode polarization-preserving fiber for spatial filtering. A small amount of repumper light ($\sim$ 100 μW) is also coupled into the fiber. The output of the fiber is then coupled to a TA (Eagleyard Photonics EYP-0850-00500-3006-CMT03). The output of the TA is passed through an AOM and coupled to another single-mode polarization-preserving fiber. The AOM detunes the laser red by 275 MHz and allows switching the laser on and off. After the fiber, the laser has 25 mW of power.

At the output of the fiber, a spot is imaged on the Zeeman slower beam. This is done to prevent the beam from interacting with the MOT. A schematic of the imaging system can be seen in Fig. 4.8. A $\lambda/4$ waveplate is used to create the σ^- circular polarization needed for slowing.

The laser is aligned to the atomic beam by maximizing the light that passes through the apertures after the atomic beam has been aligned following the

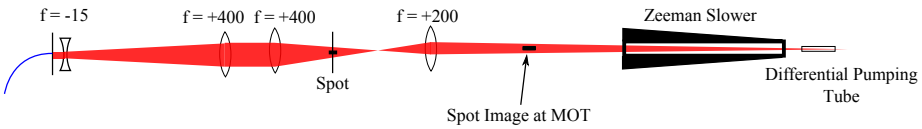

Figure 4.8: Setup for imaging a spot onto the Zeeman slower beam. The focal lengths of the lenses are in mm. The distance between the final lens and the MOT is 400 mm. Following the final lens, the beam converges to a focus 2 m from the lens.

instructions in Section 4.1.2.

4.3 Trap Apparatus

4.3.1 Magneto-optic trap

The magneto-optic trap (MOT) is formed in the center of the spherical vacuum chamber. Six independent beams are sent into the chamber as three pairs of counterpropagating beams which are orthogonal to each other. Fig. 4.9 shows the configuration of optics needed for a six-beam MOT. This configuration of the optics allows the beam balances on each pair of beams to be independently controlled by rotating the $\lambda/2$ waveplates before the pair's splitting cube.

For loading the far-off resonance trap (FORT), it is necessary that the beams be well-balanced. In the MOT the atoms are slowed by an optical molasses: the six orthogonal beams which slow the atoms down in three dimensions. How well the beams are balanced will determine the quality of the optical molasses and

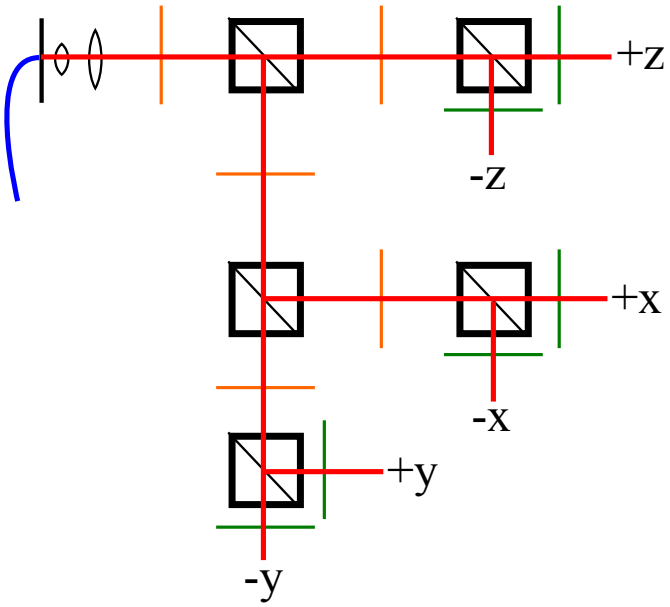

Figure 4.9: Schematic of the beamsplitter setup for a 6-beam MOT. This setup allows balances of the pairs of beams to be independently controlled without changing the powers of the other beams. This facilitates beam balance adjustment for improving the optical molasses.

as a result the temperature of the MOT. The temperature of the atoms needs to be very low to be loaded into the dipole trap: the temperature of the MOT is ~ 125 μK, limited by the Doppler cooling limit, and the temperature of the FORT is ~ 40 μK. As a result the quality of the molasses strongly impacts the number of atoms that can be loaded into the FORT.

The molasses can be tested by turning off the magnetic field in the chamber while the trapping lasers remain on. If the beams are well-balanced, the atoms will remain in the same place for at least one second. If the atoms are pushed off to one side, the $\lambda/2$ waveplates should be adjusted to balance the beams. In addition, the alignment of the MOT beams may need to be adjusted. In general the alignment of the MOT beams should be adjusted for maximum atom number, but the optimum molasses can only be obtained when the alignments are set so that the position of the MOT overlaps the zero of the magnetic field as well as possible. This can also be adjusted by adjusting the currents in the bias field coils outside the vacuum chamber.

The magnetic field coils for the MOT are located inside the vacuum chamber. The coils are water-cooled copper tubes, typically carrying 30 A of current. The coils are switched using an insulated-gate bipolar transistor (IGBT) which can turn off the magnetic field in as little as 10 μs, depending on the number of transient voltage suppressors (TVS) used in the circuit (depicted in Fig. 4.10).

The MOT can be loaded from the Zeeman slower or from a background atomic vapor. The oven for the background vapor is connected to the chamber.

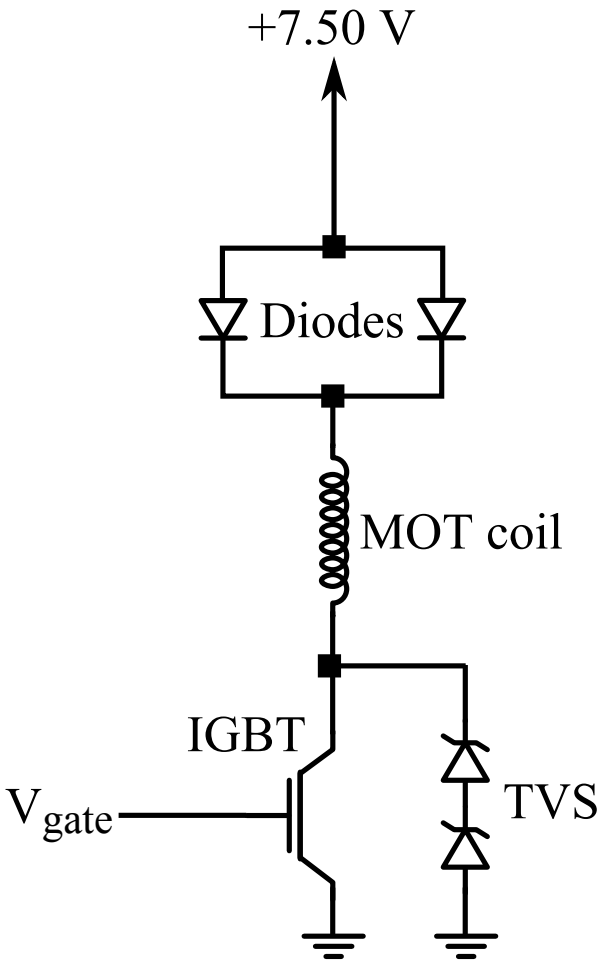

Figure 4.10: Circuit diagram for the IGBT current switch.

The cesium source in this oven is typically heated to ~ 40 °C during operation. This oven was not used during the trilobite experiment because it causes a higher background pressure to occur in the main chamber, which reduces the lifetime of the FORT.

4.3.2 Far off-resonance trap

The crossed FORT is formed using a 1064 nm ytterbium fiber laser which operates at a power of 50 W (IPG YLR-50-1064-LP). The crossing beams have a $(1/e^2)$ beam waist of 98 ± 1 μm. The first pass of the laser is sent along the same axis as the z-axis of the MOT lasers, and the second pass is at an angle of 22.5^o to the first, resulting in the cross having an aspect ratio of $\sim 2:1$. With these parameters, the trap depth is $T \sim 5$ mK and the trap frequencies are $2\pi \times 3.58$ kHz along the short axis and $2\pi \times 1.0$ kHz along the long axis. After loading, the peak density of the trap is $\sim 5 \times 10^{13}$ cm^{-3}.

After exiting the chamber, the beam is recollimated and sent through a $\lambda/2$ waveplate which rotates the linear polarization by 90 degrees. This polarization change is necessary to prevent interference between the two beams. Interference between the two beams would result in the formation of an optical lattice, due to the interference fringes, rather than the desired crossed dipole trap. Since the beams are not interferometrically stabilized, the fringes would be unstable. This instability would heat atoms out of the trap, preventing atoms from being trapped in the crossing region. Thus, it is necessary to prevent the fringes by

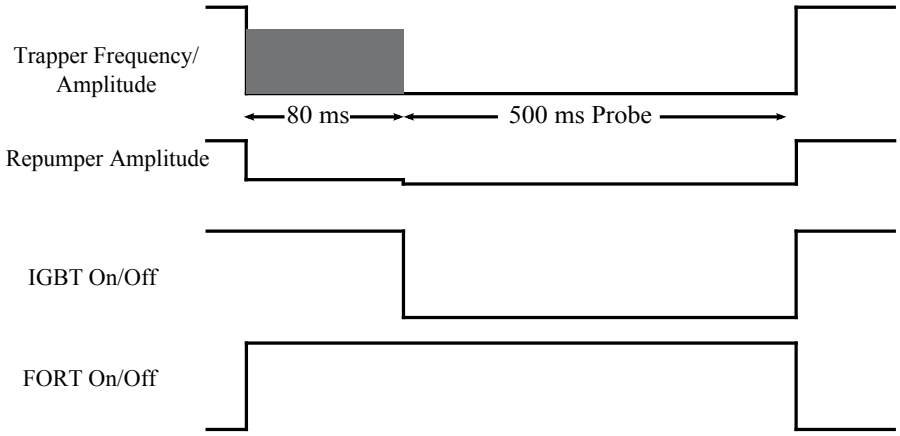

Figure 4.11: Timing diagram for the FORT loading. Gray shading in the trapper timing represents a −15 MHz frequency detuning. After the MOT is loaded for 1.4 s, the MOT trapping laser is detuned by −15 MHz and reduced in power by a factor of 1/3, at the same time as the repumper laser is reduced in amplitude. At the same time, the FORT laser is turned on. This loading period occurs for 80 ms, then the MOT lasers and IGBT are turned off. The FORT is then probed for 500 ms before the MOT loading cycle begins again.

rotating the polarization of the second pass of the laser.

Because the trap depth of the FORT is small and the FORT does not actively cool atoms, it must be loaded from a MOT. This process involves cooling the atoms below the Doppler cooling limit using polarization-gradient cooling. To do this, the MOT trapping laser is shifted in frequency and power. This is done by shifting the AOM in the seed laser for the TA by ~ 15 MHz. This shift also reduces the output power of the TA by changing the pointing of the seed laser

into the optical fiber, reducing the total power of the trapper laser from 100 mW to $\sim$ 35 mW. This process reduces the temperature of the atoms in the MOT from the Doppler temperature in ^{133}Cs, $\sim$ 125 μK [56], to $\sim$ 40 μK.

Additionally, the repumper laser is reduced in power to $\sim$ 50 μW to facilitate optical pumping into the $6S_{1/2}(F = 3)$ ground state. This is necessary to avoid collision-induced trap loss, as the $\sim$ 9 GHz energy difference between the hyperfine levels in ^{133}Cs is sufficient to heat atoms out of the trap, greatly reducing trap lifetime.

A timing diagram is shown in Fig. 4.11. The MOT is loaded for 1.4 s before the FORT loading begins. The polarization gradient cooling and optical pumping is done for 80 ms. After the cooling, the MOT lasers and magnetic field are turned off.

The lifetime of the FORT is dependent on the density of the FORT and the background pressure of the vacuum. A decay curve for the FORT is shown in Fig. 4.12. The data is fit to an exponential decay function with two time constants. The shorter time constant models the three-body recombination losses which occur at high densities. Three-body recombination occurs in dense samples, and is a common problem in BEC experiments [57]. As the density decreases, the three-body recombination losses decrease and the losses due to background collisions, modeled by the second decay constant, become dominant. The first decay constant fits to 30 ms and the second decay constant fits to 1470 ms.

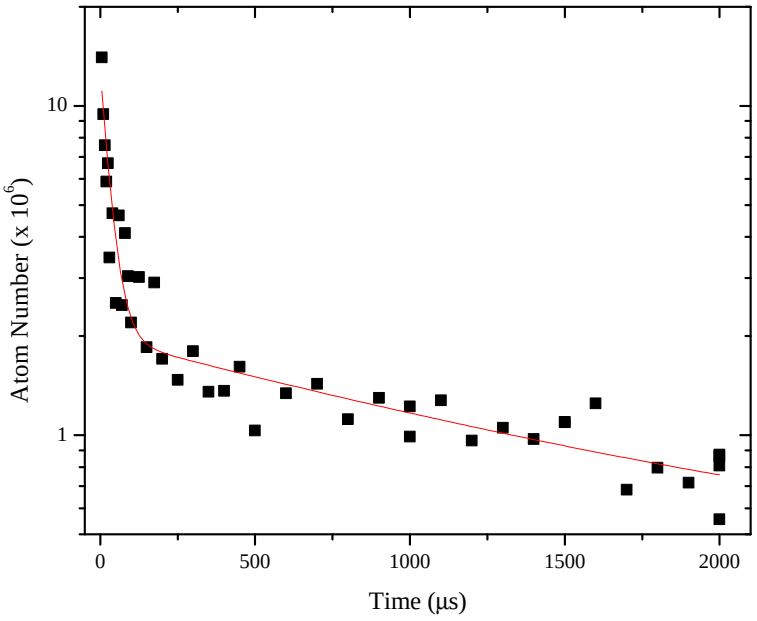

Figure 4.12: A decay curve for the crossed FORT. The atom number is plotted against the holding time of the trap, on a logarithmic scale. The red line shows an exponential decay fit with two time constants. The shorter time constant is 30 ms and the longer time constant is 1470 ms.

4.3.3 Trap Imaging

Imaging of the MOT and FORT can be done by fluorescence or absorption imaging. There are two CCD cameras used for imaging. A Watec 902H3 is used for fluorescence imaging during initial alignment and detection of the MOT and FORT, as its sensitivity is useful for detecting low levels of light, but it saturates at higher levels of light. An 850 nm interference filter is used to remove stray light at wavelengths other than the ^{133}Cs D2 line.

A Basler A202k is used for fluorescence imaging of larger traps, as well as for absorption imaging of traps. On the computer that controls the camera, two programs are needed: CCT+ controls camera exposure parameters including gain, exposure time, and triggering, while pdvshow (or, for absorption imaging, getpic16bit) displays and records the images.

Fluorescence imaging of the MOT is relatively simple: under normal operation the MOT fluoresces due to scattered light from the trapper laser. The fluorescence image can be taken by setting CCT+ to free-run triggering and setting the focus of the lens on the camera to obtain a clear image of the MOT. When the MOT is functioning well, the image in pdvshow should be red at 2 ms exposure time.

Obtaining a fluorescence image of the FORT requires flashing on the MOT beams and triggering the camera at the same time to observe the fluorescence. The camera is triggered using a TTL signal sent into the BNC on the back of the control computer. This BNC is internally connected to the trigger pins on the

control card. CCT+'s triggering option should be set to "ExSync Programmable". The process of flashing the MOT beams is destructive to the FORT. If the FORT is functioning well, the image of the cross in pdvshow should be red at 2 ms exposure time with maximum gain.

A simple imaging system is used for absorption imaging in our system. A 1 mm collimated probe laser, produced by an ECDL tuned to the $6S_{1/2}(F = 3) \rightarrow 6P_{3/2}(F' = 2)$ transition and decreased in power to 500 μW, is pulsed for 200 μs. An $f = 100$ mm lens is placed 400 mm from the trap, with the Basler camera placed ~ 125 mm from the lens. This imaging system has a magnification factor of $-1/4$. The camera position will need to be adjusted carefully to obtain the clearest image possible.

By subtracting the image with the dipole trap present from the image without the dipole trap present, an image of the FORT can be produced. The subtraction can be done in the getpic16bit program by taking a "flat field" image of the absorption beam with the FORT absent and a "background" image with the absorption beam absent, and then selecting "Flat Field Subtraction". The image that the program presents is proportional to the optical density of the FORT, according to the relation:

$$\text{Pixel Value} = \frac{OD \times 1024}{5}, \tag{4.1}$$

where OD is the optical density. If using a camera other than the Basler, the

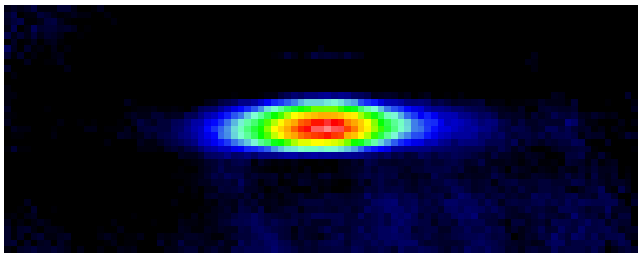

Figure 4.13: False-color absorption image of the crossed FORT. The absorption imaging beam is in the same plane as the FORT beams.

factor of 1024 may be different. The Basler A202k is a 10-bit camera, resulting in a factor of $2^{10} = 1024$. If using a 16-bit camera, the factor is $2^{16} = 65536$.

An example of an absorption image produced using this process is shown in Fig. 4.13. Images of the MOT can be similarly produced by tuning the probe laser to the $6S_{1/2}(F = 4) \rightarrow 6P_{3/2}(F' = 5)$ transition.

4.4 Excitation Lasers

The excitation into the Rydberg state is a two-photon excitation, requiring two lasers. There are several advantages to using a two-photon excitation rather than a one-photon excitation. Using a two-photon transition allows longer wavelengths to be used for excitation light. In this case, an 852 nm and a 510 nm photon rather than a 320 nm photon, which would be difficult to generate with current laser technology. Using a two-photon excitation, only S and D Rydberg states are dipole-allowed, as opposed to only P states in the case of a one-photon excitation. In the presence of electric fields, state mixing due to the Stark effect

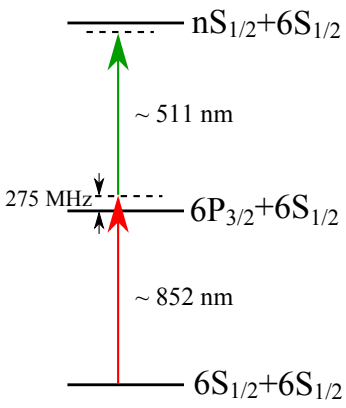

Figure 4.14: Level diagram for the two-photon Rydberg excitation.

can allow the excitation of states that are dipole-forbidden in the field-free case, including P states.

A level diagram for the two-photon transition is shown in Fig. 4.14. The first step of the excitation is near the $6S_{1/2} \rightarrow 6P_{3/2}$ transition, and the second step is from the $6P_{3/2}$ state to the Rydberg state.

4.4.1 First step laser

The first step laser is an ECDL of similar design to the repumper laser. It is locked to a saturated-absorption DAVLL signal. It is operated on the $6S_{1/2}(F = 3) \rightarrow 6P_{3/2}$ transition, since the atoms trapped in the FORT must be in the lowest ground hyperfine state to avoid hyperfine-changing collisions.

A separate saturated-absorption cell is used as a frequency reference to verify the frequency of the first step laser. The laser is locked using the DAVLL to a

frequency that maximizes one of the peaks in the saturated absorption setup (for example, in the trilobite spectra experiment, the $6P_{3/2}F' = 4$ peak is used), and then the saturated absorption signal is monitored to ensure the laser has not drifted. Using this system the frequency of the first-step laser relative to the $6S_{1/2} \rightarrow 6P_{3/2}$ transition can be verified to within ~ 2 MHz.

The light from the first-step laser is coupled to a polarization-preserving optical fiber and sent to the experiment. The light for the experiment is sent into the chamber collimated with a 1 mm spot size and a power of 2 mW.

4.4.2 Second step laser

The second step of the Rydberg transition is provided by a photon ~ 511 nm. This green light is generated using a Coherent 699-21 dye laser. The gain medium for this laser is Coumarin 521 dye dissolved in ethylene glycol. With 7.3 W pumping from an Ar^+ laser, the 699 produces ~ 300 mW of output power. The laser has a linewidth of ~ 1.5 MHz and is frequency-stabilized to a signal from a Fabry-Perot cavity.

The light from the 699 is sent through an AOM, and the first-order spot is coupled to a single-mode polarization-preserving optical fiber. The output from the fiber is ~ 70 mW. This output is focused and co-propagated with the second pass of the FORT beam. The spot size of the green light is 25 μm.

The output wavelength of the 699 is monitored using a wavemeter and an iodine cell reference, as well as with an electromagnetically-induced transparency

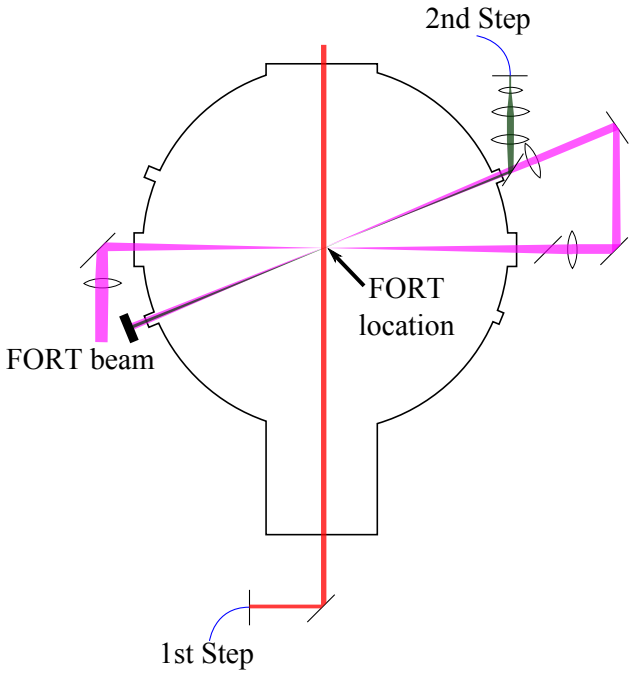

Figure 4.15: Diagram showing alignments of the excitation beams in the trilobite experiment relative to the FORT beam alignment. View is from above; all the beams are coplanar.

(EIT) setup.

4.4.3 Excitation beam alignment

A schematic of the excitation beam alignment is shown in Fig. 4.15. The first-step beam is sent into the chamber collimated to a 1 mm spot size and passed through the dipole trap perpendicular to the first pass of the FORT beam. The power in the first-step beam is ~ 2 mW.

Alignment of the first-step laser can be done by setting up the absorption

imaging optics described in Sec. 4.3.3, using the first-step laser (attenuated to 500 μW) as the absorption imaging beam. If the cross is centered in the absorption image, then the beam is aligned to the cross. For rough alignment, one can increase the power of the first-step laser, tune it to the $6S_{1/2}(F = 4) \rightarrow 6P_{3/2}(F' = 5)$ transition, and use the first step laser to destroy the MOT.

The second-step beam is copropagated with the second pass of the dipole trap and is focused to a spot size of 25 μm. The angle between the first-step and second-step beams is 72.5°. The power in the second-step beam is $\sim$ 70 mW.

Alignment of the second-step beam can be done by ion detection, and the AC Stark shift of the FORT can be exploited to facilitate alignment to the cross. Tune the second-step laser to resonance and adjust the alignment to maximize the ion signal. If the detector becomes saturated, attenuate the second-step laser. After maximizing the signal, tune the laser blue of the transition by $\sim$ 10 MHz and maximize the signal again. Because the AC Stark shift from the FORT moves the Rydberg transition to the blue, detuning the laser allows finding the maximum AC Stark shift, which corresponds to the cross region of the FORT.

For rough alignment of the second-step laser, reduce the output power of the fiber laser to $<$ 1 W and place a mirror between the chamber window and the dichroic mirror that couples the second-step laser. Using an infrared-sensitive card (as a precaution, only use a card rated for the power of the fiber laser, as more sensitive cards can be damaged by the beam), locate the focus of the fiber

laser. Adjust the alignment of the second-step laser so that it is aligned with the FORT beam the entire way through the focus. The lens position of the second-step laser may also need to be adjusted so that the foci are in the same plane.

4.4.4 EIT reference

The frequency of the 699 is monitored using an EIT reference cell. A schematic of this setup can be seen in Fig. 4.16. The light from the zero-order spot from the 699 AOM is sent through another AOM (AOM G in Fig. 5.3) and a chopper wheel. This light passes through co-propagating with the light from the first step laser and is retroreflected by a dichroic mirror and counter-propagates with the first step laser.

Knowing the frequency of the first-step laser (by referencing it to the saturated absorption cell) and the frequencies of the various AOM shifts, it is possible to calculate the frequencies of all the EIT peaks relative to the Rydberg line in the FORT. If the first-step light at the EIT cell is detuned from a hyperfine level by δ_{hf}, then for the EIT peak to occur, the Doppler shift from the second step must cancel out the Doppler shift from the first step for the same atomic velocity class. This occurs when the second-step detuning δ_{ss} is:

$$\delta_{ss} = \delta_{hf} \frac{\lambda_1}{\lambda_2}, \tag{4.2}$$

where λ_1 and λ_2 are the wavelengths of the first and second step lasers respectively;

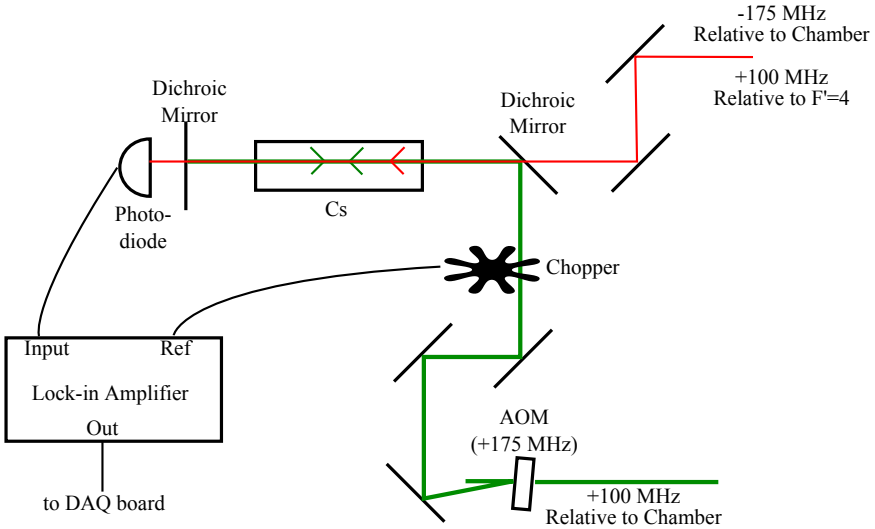

Figure 4.16: Diagram of the EIT alignment and electronics. The first-step laser alignment is shown in red. The first-step laser is coupled to the second-step with a dichroic mirror, passes through the cell and through another dichroic mirror, then is measured by a photodiode. The second-step beam, shown in green, passes through an AOM and a chopper wheel, is coupled in with the dichroic mirror, then passes both counterpropagating and copropagating with the first-step laser. The output of the photodiode is demodulated with a lock-in amplifier locked to the reference signal from the chopper.

in ^{133}Cs, they are $\sim$ 852 nm and $\sim$ 510 nm. When the second-step light is both counter- and co-propagating with the first-step light, two EIT peaks will be present for each hyperfine level. The counterpropagating peak will occur at $\delta_{hf} - \delta_{ss}$ from the undetuned frequency in the cell, and the copropagating peak will occur at $\delta_{hf} + \delta_{ss}$ from the undetuned frequency in the cell. For example, if the light in the cell is resonant with the $F' = 3$ hyperfine level in the cell, then the peaks associated with the $F' = 4$ hyperfine level, detuned by 200 MHz, will occur at -134 MHz and 534 MHz relative to the undetuned frequency in the cell. The frequencies of the peaks relative to the Rydberg line in the chamber are offset by the frequency differences between the first-step and second-step lasers in the cell and in the chamber.

As an example, for the AOM detunings shown in Fig. 5.3, the detuning of the first-step light δ_{hf} from $F' = 3$ at the EIT cell is 300 MHz. The detuning of the second-step light at which the EIT peak occurs, δ_{ss}, is 501 MHz. Thus, EIT peaks will occur at:

$$\nu_{EIT} = \Delta_1 + \Delta_2 + \delta_{hf} \pm \delta_{ss}, \tag{4.3}$$

where Δ_1 is the frequency difference between the cell and the chamber for the first-step light (in this case, 175 MHz), and Δ_2 is the frequency difference between the cell and the chamber for the second-step light (in this case, -375 MHz, the sum of the two AOMs in the second-step laser alignment). Putting in these numbers yields EIT peak positions relative to the atomic Rydberg line in the

chamber (ignoring AC Stark shift) of −401 MHz for the counterpropagating peak and 601 MHz for the copropagating peak. A Mathematica notebook "EIT_Shifts.nb" has been written to automatically calculate these peak positions given the AOM shifts.

4.5 Experimental timing

The master timing for the experiment comes from an SRS DG535 digital pulse generator. This pulse generator has a resolution of 5 ps.

There are four variable delays, labeled A, B, C, and D, and a T0 channel, which is used to trigger the Thorlabs DG 100N pulse generator. Channels A and B are used as the start and end timers for the 699 and first step laser pulses, and channel C is used as the start timer for the electric field pulser. The internal trigger is used for the SRS pulse generator, in burst mode. The experiment is typically run at 2 kHz, with bursts of 1000 pulses every two seconds (4000 periods).

The Thorlabs pulse generator has six outputs and a resolution of 25 ns. Channel 1 on the Thorlabs box is sent through an AND gate with channel 1 on the National Instruments DAQ card to produce the on/off signal for the FORT. Channel 2 on the Thorlabs box is used as a modulation signal for the chopper AOM in the saturated absorption setup in the first-step laser. Channel 3 is the trigger for the National Instruments DAQ board. Channel 4 is used as a

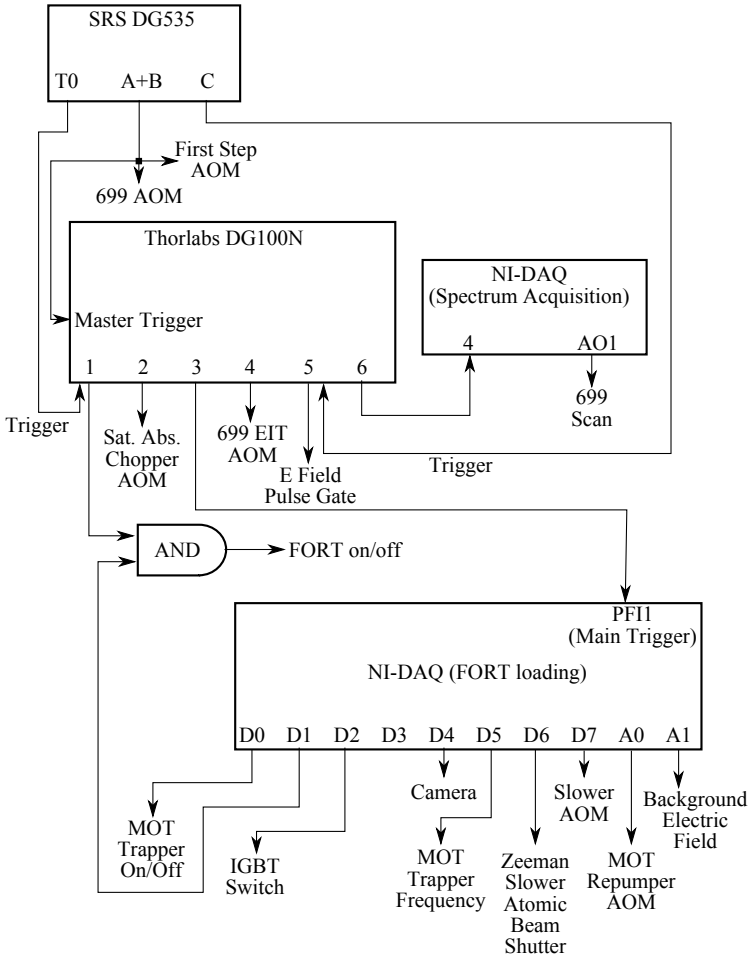

Figure 4.17: Diagram of the timing electronics for the experiment. The SRS DG535 and the Thorlabs DG100N control the timing of the probing, and the NI-DAQ board controls the timing of the FORT loading. Channel D3 on the NI-DAQ board is unused.

constant-on channel. Channel 5 receives as an external trigger the output of channel C from the SRS pulse generator and when triggered outputs a 500 ns TTL pulse which provides the gate signal for the electric field pulser. The reason Channel 5 is used in this way is so that only Channel C (and not Channel D) needs to be adjusted on the Stanford box in order to adjust the delay before the electric field pulse, since the length of Channel C's pulse is determined by the value of Channel D. Channel 6 on the Thorlabs box is used as a trigger which informs the NI-DAQ board which is used for scanning the second-step laser when the pulse train has ended and the frequency can be incremented.

The National Instruments DAQ card, which is used for the timing of the FORT loading, is triggered from channel 3 of the Thorlabs pulse generator, which is given a 1500 ms pulse length. This is done so that the National Instruments board will only be triggered by the first T0 per burst, which ensures that the timing of excitation pulses falls during the time the FORT is present.

The control program for the National Instruments board is a custom program written in C++. The interface for this program is shown in Fig. 4.18. The NI board has eight digital outputs and two analog outputs. Timings in the control program for the NI board are in μs, and the resolution of the board is 10 μs. Each digital output has a delay, width, and polarity associated with it. As an example, a digital channel with a delay of 500 μs, a width of 1000 μs, and positive polarity will, after the NI board receives its trigger, be off for 500 μs, then turn on for 1000 μs, then turn off until the board is triggered again (unless

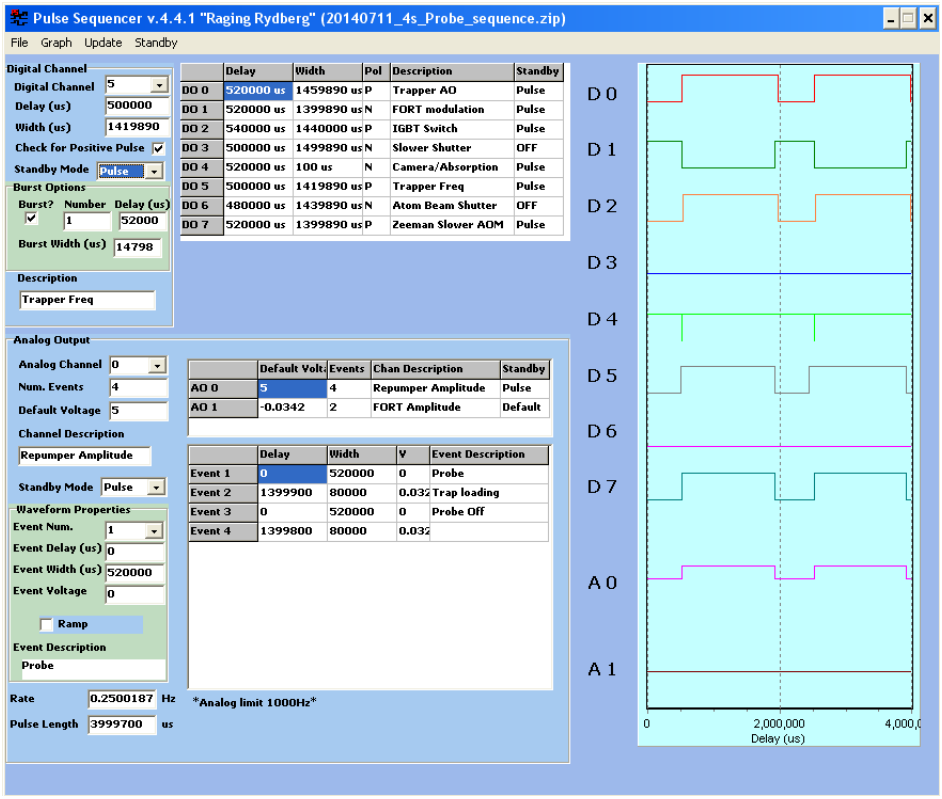

Figure 4.18: Screenshot of the control program for the National Instruments DAQ card. In the top left is the control for the digital channels with parameters for channel 5 displayed. In the bottom left is the control for the analog channels, with channel 0 displayed. Below the analog channel interface, the text box labeled "Pulse Length" determines the total length of the pulse (and as a result the maximum rate at which the board can be triggered.)

the delay+width is exactly the same as the pulse length, in which case the channel will stay on). The burst option allows a second delay and width to be specified, which will be repeated for a specified number of times, after the initial delay and width.

The analog channels each have a default voltage which the board returns to during delays and after the end of the pulse. Each analog channel then has a certain number of events which each consist of a delay, a width, and a voltage. For example, the analog channel controlling the repumper amplitude has a default voltage of 5 V and four events. Event 1 has a delay of 0 μs, a width of 520000 μs, and a voltage of 0 V. Event 2 has a delay of 1399900 μs, a width of 80000 μs, and a voltage of 0.032 V. Thus after a trigger is received, A0 will immediately go to 0 V, stay there for 520 ms, then return to 5 V for 1.3999 s, then it will go to 32 mV for 80 ms.

4.6 Rydberg ionization and detection

To detect any Rydberg atoms present in the sample, they must be ionized and projected onto the microchannel plate (MCP) detector in the chamber. The voltage on the MCP is -5 kV.

There are two primary ways to perform the ionization: photoionization and pulsed electric field ionization (PFI). In either case, the ions are projected onto the detector by an electric field pulse, and the resulting voltage pulses from the

MCP are counted by a multi-channel analyzer (MCA) card (FastComTec P7886) with 500 ps resolution in the experimental control computer.

For many experiments done in the FORT, the photoionization of Rydberg atoms due to the FORT beam [30] can be used for the ionization step. The main advantage of using photoionization is that this method does not require large electric pulses. The maximum voltage that can be supplied by the pulser in the experiment (DEI PVX-4140, supplied by a Glassman EK high voltage power supply) is 2 kV. With an electric field plate spacing of 4.5 cm, the maximum field that can be supplied at the FORT is ~ 440 Vcm^{-1}. Additionally, the repetition rate of the experiment is limited by the power that can be dissipated on the resistors in the chamber. The combined resistance of the system in the chamber is 3 kΩ, and the resistors can only dissipate 1/8 W. As a result, the average power dissipated across the resistors must not exceed 1/8 W. The average power can be expressed as:

$$P = \frac{V^2}{R}\tau f, \tag{4.4}$$

where τ is the width of the electric field pulse, and f is the repetition rate of the experiment. As the power is dependent on the square of the voltage, higher voltages require much lower repetition rates to avoid going over the power limit.

The threshold field for electric field ionization as a function of principal quantum number n is [22]

$$E = \frac{1}{9n^4}. \tag{4.5}$$

For $n \leq 31$, the threshold field exceeds the maximum that the pulser can provide, and as a result for these n, photoionization must be used instead.

Photoionization with a single FORT photon works because the energy required to ionize a Rydberg atom ($\sim 10^{-2}$ eV) is less than the energy provided by a photon from the FORT beam 1.17 eV. In this process the Rydberg electron absorbs the photon and is separated from the ionic core, gaining a large amount of kinetic energy due to the energy of the photon. The cross-section σ of the photoionization is given by [33]:

$$\sigma = 2\pi^2 \frac{\hbar e^2}{m_{Cs} c} f, \tag{4.6}$$

where the oscillator strength f is:

$$f = \sum_{L=L_{ryd}-1}^{L_{ryd}+1} \frac{2m_{Cs}\omega \mathrm{Max}(L, L_{ryd})}{3\hbar(2L_{ryd}+1)} \int_0^\infty \Psi_{ryd}(R) R \Psi_{cont} \mathrm{d}R, \tag{4.7}$$

where L_{ryd} is the orbital angular momentum quantum number of the Rydberg state being photoionized, ω is the angular frequency of the laser field, Ψ_{ryd} is the radial wavefunction of the Rydberg atom, and Ψ_{cont} is the radial wavefunction of the continuum state at the sum of the Rydberg state energy and the photon energy.

The photoionization rate can then be determined from the cross section by:

$$R = \frac{I_{max}}{2\hbar\omega}\sigma, \tag{4.8}$$

where I_{max} is the light intensity at the center of the crossing region of the FORT. This method was used to calculate photoionization rates in a single-beam trap for $nD_{5/2}$ Rydberg states which were then experimentally verified [30].

The disadvantages of using photoionization include the presence of an AC Stark shift due to the light field, and a reduced detection efficiency, as not all the atoms will be ionized at the same time. In the trilobite experiment, the efficiency of the photoionization is $\sim 50\%$.

For $n > 31$, it is possible to do pulsed electric-field ionization in this apparatus. This has the advantage of greater detection efficiency, and the possibility of state selection by applying a ramped electric field. The electric field can be ramped by applying capacitors across the output of the pulser.

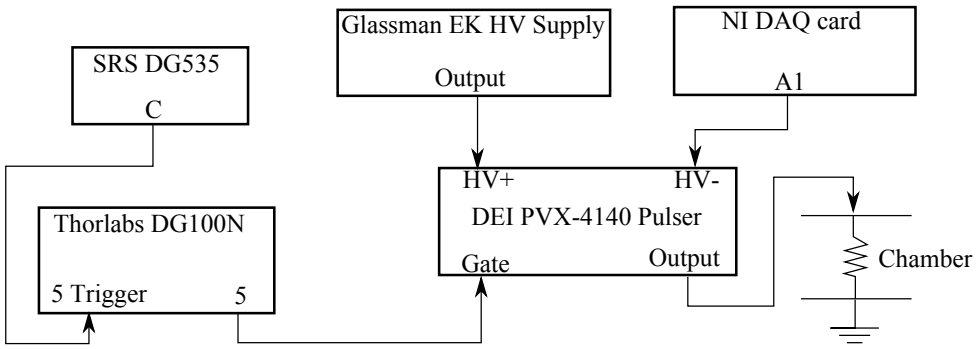

Figure 4.19: Diagram of the electronics setup for the electric field pulsing. Three inputs are needed for the pulser: a positive high-voltage input (HV+), a negative high-voltage input (HV-), and a gate. The gate accepts a TTL pulse from Channel 5 of the Thorlabs box. When the TTL is high, the pulser sends HV+ to the chamber, and when the TTL is low, the pulser sends HV- to the chamber. HV+ comes from a high voltage power supply, and HV-, which is used to provide a background electric field, comes from analog channel 1 of the NI DAQ board.

Chapter 5

Trilobite Molecules with kiloDebye Dipole Moments

5.1 Introduction

Trilobite molecules, as described theoretically in Sec. 2.4, are bound states which asymptotically correspond to a Rydberg atom and a ground state atom. The ground state atom is located inside the electron cloud of the Rydberg atom and is bound to the Rydberg atom due to the scattering interaction between the ground state atom and the Rydberg electron.

These molecular states are of interest due to their long-range interactions and their strong sensitivity to electric fields. Some of these molecular states exhibit strong symmetry breaking, which causes localization of the electron wavepacket on the ground state perturber, resulting in a permanent electric dipole moment. This system is a few-body system consisting of two heavy bodies (the ground state atom and the Rydberg ionic core) and a light body (the electron). As a result, the system's interactions can be constructed in terms of two-body interactions despite the system being three-body.

There are three classes of these ultralong-range Rydberg molecules, separated based on the orbital angular momentum of the Rydberg electron and the relative dominance of the p-wave contribution to the potential, as described in Sec. 2.4.

States with $L \leq 2$ are nonpolar, and states with $L > 2$ are polar. The symmetric $L \leq 2$ states are (in the case of S and D states) accessible via a two-photon transition from the $S_{1/2}$ ground states of the alkali atoms. These states, ignoring any admixture of high angular momentum, lack a permanent electric dipole moment.

The $L > 2$ states, also called hydrogenic states, can possess very large dipole moments due to mixing of states with opposite parity. Because the hydrogenic states are nearly degenerate, the associated ultralong-range Rydberg molecules have strong mixing between the many states of opposite parity in the hydrogenic manifold, breaking the symmetry of the homonuclear diatomic molecule, causing the probability distribution of the electron to collect near the ground state perturber [3]. In this case the interaction between the electron and the ground state atom results in a localization of the electron wavepacket near the perturber, causing a permanent molecular-frame electric dipole moment. The interactions between states can also introduce admixtures of the high angular momentum states into the symmetric $L \leq 2$ states, allowing the mixed states to possess permanent electric dipole moments while still being accessible to two-photon excitation from the ground state.

There are two types of $L > 2$ molecules, depending on the relative dominance of the s-wave and p-wave interactions. When the s-wave interaction is dominant, the "trilobite" molecule is formed. These molecules have $^3\Sigma$ symmetry (i.e., their projection of angular momentum along the internuclear axis is zero). When

the p-wave interaction is dominant, "butterfly" molecules can be formed. These molecules can have Π symmetry (i.e., their projection of angular momentum along the internuclear axis is one) as well as $\Sigma(M = 0)$ symmetry [10]. This symmetry can be used to determine whether an observed state is of the trilobite or butterfly type, by observing the selection rule behavior the state has.

Previous experiments have observed dipoles as large as ~ 1 Debye in ^{87}Rb [1] and $15 - 100$ Debye in ^{133}Cs [2]. In each of these cases the excitation was to a state asymptotically corresponding to a $(nS_{1/2} + \text{ground state})$ pair. Pure S-state ultralong-range Rydberg molecules, however, do not have significant dipole moments as they do not have mixing between states of opposite parity. The dipoles observed in these experiments are due to admixtures between the S-states and hydrogenic states. As described in Sec. 2.4, the small non-integer portion of the S state quantum defect, as well as the low-energy p-wave resonance at ~ 8 meV and the large spin-orbit coupling in ^{133}Cs result in large mixing between the $nS + 6S$ and $(n-4)(L \geq 3) + 6S$ potentials. In the case of the ^{87}Rb experiment in [1], the admixture is $\sim 0.1\%$, and in the case of the ^{133}Cs experiment in [2], the admixture is $\sim 1\%$. In this chapter, states in ^{133}Cs with hydrogenic admixtures $\sim 60-90\%$ leading to permanent electric dipole moments of $1000 - 3000$ Debye are described.

These states contrast with the macrodimers discussed in Sec. 2.5, which consist of two Rydberg atoms bound by multipolar interactions. Although both carry the label "ultralong-range", they are significantly different in scale:

macrodimer states are typically ~ 5000 nm in internuclear separation, while trilobite states have internuclear separations of ~ 100 nm. As a result, to observe trilobite states, atomic samples with higher densities are required. In addition, the binding energies of trilobite molecules are on the order of 1 GHz and the potential wells are narrow. As a result, there are few (< 10) bound vibrational levels per well and they are spectroscopically distinguishable. Ultracold samples are required in order to observe the vibrational levels. In contrast, macrodimers have binding energies ~ 20 MHz and very broad potential wells. As a result, vibrational levels in macrodimer potential wells are so closely spaced that they are indistinguishable [21].

Both the requirements for ultracold temperature and density are met in the experiment described in this chapter by the implementation of a crossed far-off resonance dipole trap (FORT), described in Sec. 4.3.2.

5.2 "Trilobite" molecules

Three different experiments are performed on the trilobite molecules. First, spectra are taken to determine the binding energies of the molecular states. Second, to demonstrate the hydrogenic admixture of the bound states, the dipole moments of selected molecular states are measured by observing the broadenings in the spectral lines due to the Stark shift. Third, as a further test of the hydrogenic admixture of the bound states, the lifetimes of the selected molecular

states are measured by varying the time between excitation and ionization.

The atomic sample for the experiments is the far-off resonance trap (FORT). The trilobite states of interest are bound at a range of ~ 100 nm. The molecules are created through a two-photon photoassociation process. For the photoassociation to occur, there must be a pair of ground state atoms at the correct distance from each other. As a result, cold and dense samples are required to observe trilobite states. At a peak density of 5×10^{13} cm^{-3}, the atoms in the FORT have an average internuclear distance of 185 nm. Fig. 5.1 shows the pair distribution function at various densities. To achieve a significant fraction of the atoms in the proper internuclear range, a large density $> 10^{13}$ cm^{-3} is required. At a density of 5×10^{13} cm^{-3}, an individual atom has a probability of $\sim 6\%$ of having a nearest-neighbor at the correct range to be excited into the trilobite state.

5.2.1 Spectra measurement

After the FORT is loaded as described in Section 4.5, a series of 500 excitation pulses at 2 kHz occurs. A timing diagram for the probing period is shown in Fig. 5.2. The first- and second-step lasers pulse simultaneously for 10 μs. 5 μs after the end of the laser pulse, a 67 V cm^{-1} electric field pulse with a duration of 500 ns pushes ions toward the MCP detector. The FORT laser remains on during the probing period.

Ionization of any molecules formed is performed by photoionization from the

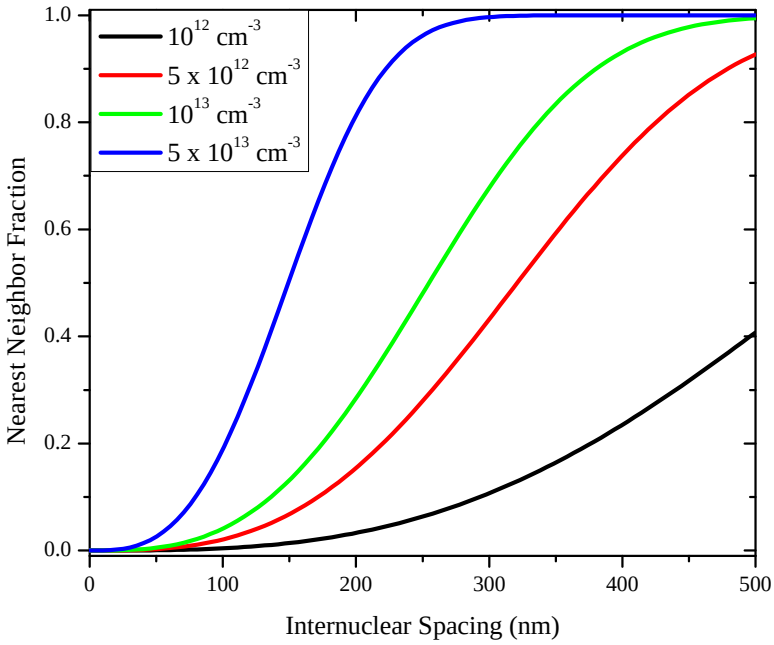

Figure 5.1: The pair distribution function at various densities. Excitation of trilobite states requires nearest neighbor pairs at ~ 100 nm, and so the trap density must be $> 10^{13}$ cm^{-3} to achieve a significant fraction of pairs the required internuclear spacing.

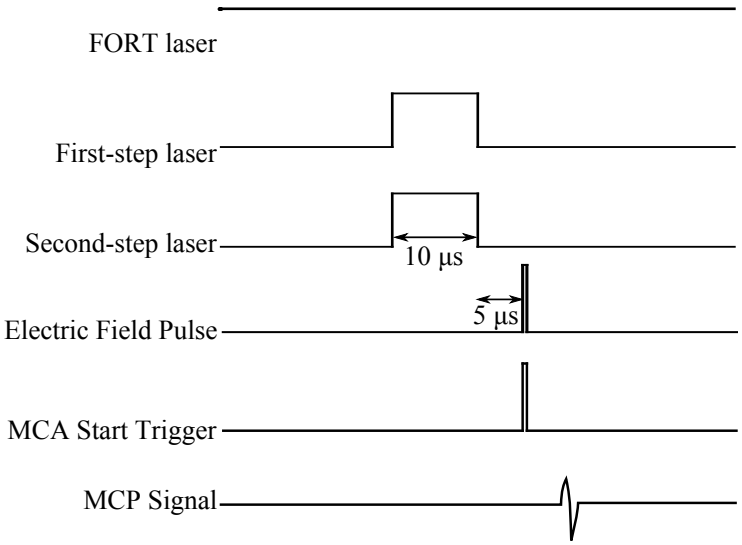

Figure 5.2: Timing diagram for the spectra and linewidth measurements. This pulse sequence is repeated 1000 times for each dipole trap at a rate of 2 kHz. The FORT is continuously on during the probing. The width of the electric field pulse is 500 ns.

FORT beam. Because the amplitude of the electric field pulse is less than the electric field needed to ionize any remaining atoms (305 V cm^{-1} for $n = 37$ [22]), atoms remaining when the electric field pulse occurs will not be counted. As a result, the detection efficiency is reduced.

In [30], the photoionization rates for $nD_{5/2}$ states were investigated in a single-beam dipole trap with 10 W of power. These results were compared to a model from [33], which is discussed in Sec. 2.2.4.

The photoionization rate depends strongly on the orbital angular momentum of the Rydberg electron; the rate at $L_r = 0$ is two orders of magnitude smaller than at $L_r = 2$. Despite this, $\sim 30\%$ of the Rydberg atoms at $31S$ are ionized before the electric field pulse occurs. Using the expression for σ and the light intensity (3×10^{10} W m^{-2}), the photoionization rate is 4.4 kHz. In addition, blackbody radiation results in redistribution of population into P states at a rate of 17 kHz. These atoms are photoionized at a rate of ~ 600 kHz after they are put into the P state and thus this process can effectively be assumed to be immediate. Considering this effect, the combined photoionization rate is ~ 21.4 kHz.

The first-step photon is ~ 852 nm, and is blue-detuned by 275 MHz from the $6S_{1/2}(F = 3) \rightarrow 6P_{3/2}(F' = 4)$ transition. The laser is detuned to allow adiabatic elimination of the intermediate $6P_{3/2}$ state, narrowing the spectral lines by avoiding broadening due to the lifetime of the $6P_{3/2}$ state. This detuning is selected to ensure that any hyperfine ghosts – spectral lines corresponding

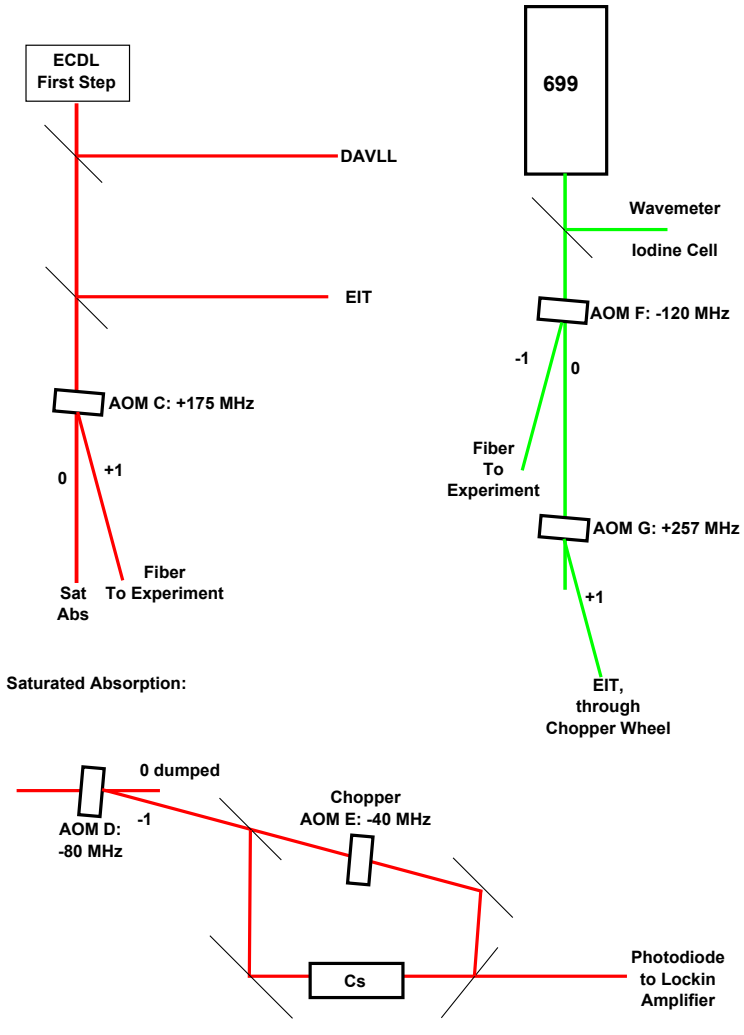

Figure 5.3: AOM detunings used in the trilobite spectra experiment.

to atoms off-resonantly excited into the $6P_{3/2}$ hyperfine levels then resonantly excited to the Rydberg state – are to the blue of the atomic transition when scanning the second-step laser, avoiding contamination of our spectra, which are taken to the red of the atomic transition.

The setup for the AOMs for the excitation lasers is shown in Fig. 5.3. The first step laser is sent through an AOM (AOM C in Fig. 5.3), and the first order spot is coupled into a fiber for the experiment. The zero-order spot is used for the saturated absorption reference. Two AOMs in the saturated absorption reference give a 100 MHz offset to the laser lock. The zero-order light goes to the EIT setup. The intensities used for the EIT are ~ 0.5 mW cm^{-2} in the first step, and ~ 500 mW cm^{-2} in the second step. For excitation of atoms in the dipole trap, 64 mW cm^{-2} is used in the collimated first step beam and 3.5×10^6 mW cm^{-2} is used in the focused second-step beam.

The second-step photon is ~ 511 nm. This laser is scanned in 1 MHz steps from ~ 1 GHz red of the atomic transition to the atomic transition.

An electromagnetically-induced transparency (EIT) signal is used as a reference for the spectra measurements. Using these detunings, the EIT peak positions can be calculated using a process described in Sec. 4.4.4. In the system shown in Fig. 5.3, there are EIT peaks corresponding to the counterpropagating beam at -478 MHz, -377 MHz, and -243 MHz. These peaks correspond to the $F = 3 \rightarrow F' = 4$, $F = 3 \rightarrow F' = 3$, and $F = 3 \rightarrow F' = 2$ hyperfine transition on the ^{133}Cs D2 line, respectively. There are also three copropagating peaks on the

blue side of the atomic line which were not used in this experiment. These peaks, along with the AC Stark shift-adjusted Rydberg peak position, are suitable for referencing the positions of the spectral lines that are observed.

Results

The spectra for the $(37S + 6S)^3\Sigma$, $(39S + 6S)^3\Sigma$, and $(40S + 6S)^3\Sigma$ systems are shown in Fig. 5.4. Theoretical spectra are also shown. For the theoretical spectra, an adjustment of 2.25% to the theoretical value for the s-wave scattering length from [35] is applied. Fig. 5.5 shows a comparison between the experimental spectrum and the potential energy curves for $(37S + 6S)^3\Sigma$. The bound state positions observed in the experiment agree well with the positions predicted by the theory.

In the potential curves shown in Fig. 5.5, the M_J projections are indicated by dashed ($M_J = 0$) and solid lines ($M_J = \pm 1$). For the potential wells that the states of interest occupy, the splittings between the projections are sufficiently small that the projections are not distinguishable given the experimental resolution. The splittings between the projections are ~ 2 MHz, while the resolution of the spectral lines, as seen in Fig. 5.4, is ~ 20 MHz.

A transverse background field $F_t \approx 15$ mV cm^{-1} is present in the experiment and causes broadening of the peaks in the spectra. The theoretical spectra are calculated with a background field of 15 mV cm^{-1} included. The peaks in the spectra are calculated using the function:

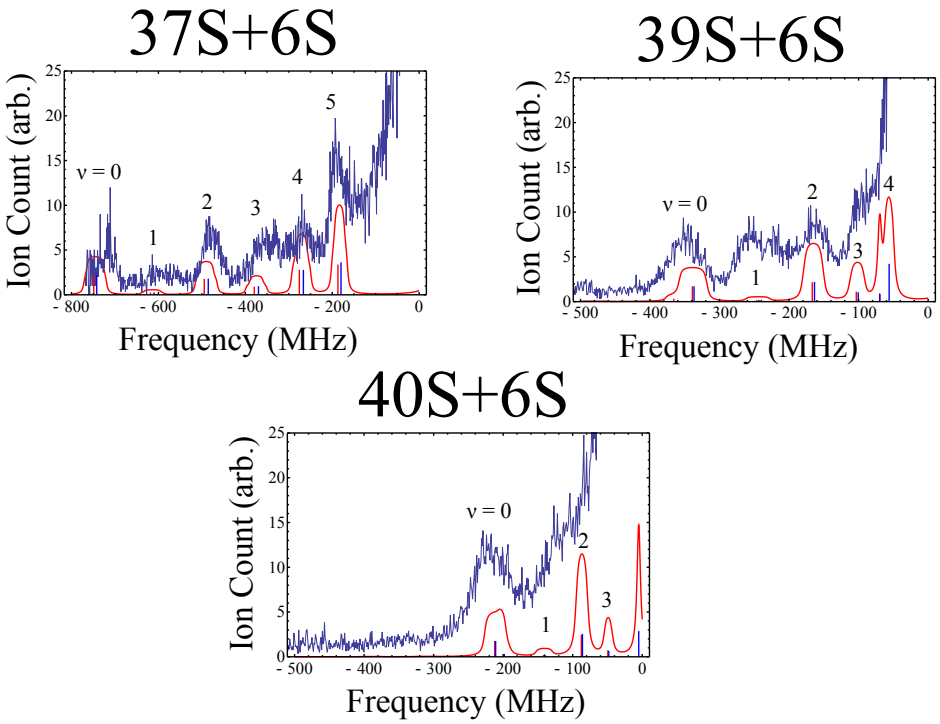

Figure 5.4: A comparison between calculated spectra (red) and experimental spectra (blue) for the states correlating to the $37S+6S$, $39S+6S$ and $40S+6S$ dissociation limits. The centroids of the vibrational levels are shown as sticks underneath the calculated spectra. Bound states corresponding to the $M_J = 0$ and $M_J = \pm 1$ projections are indicated with red and blue sticks, respectively.

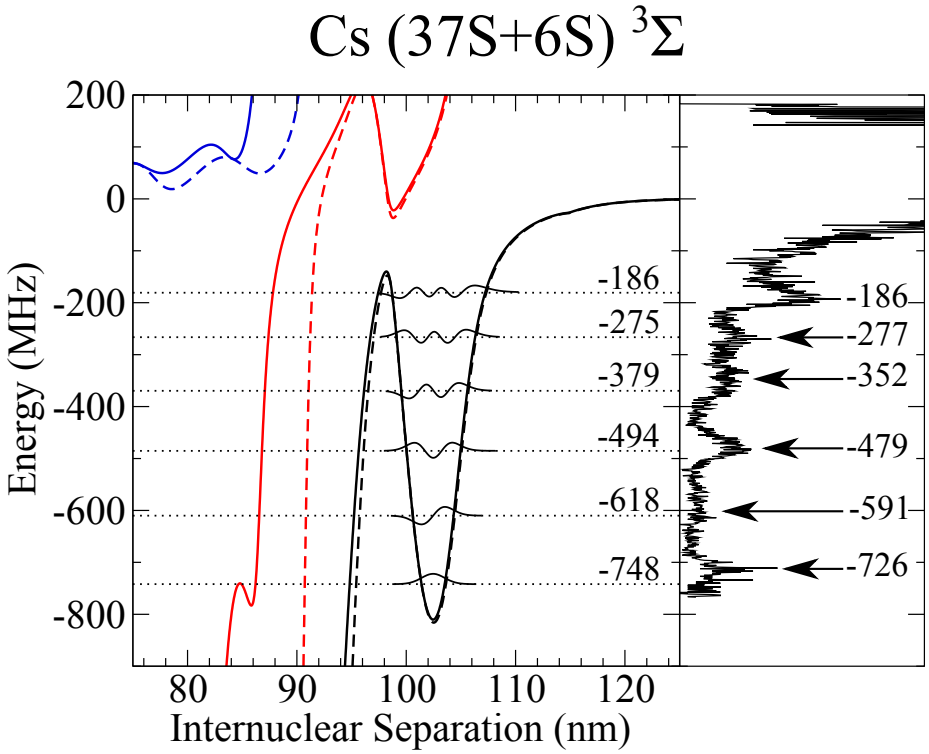

Figure 5.5: A comparison between the calculated vibrational levels in the outermost potential energy well, superposed with the associated wave functions (left) and observed spectra (right), for states correlating to the $37S + 6S$ limit. Even parity ($v = 0, 2, ...$) vibrational levels have stronger signals because the de Broglie wavelength of the ground state wave function, $\lambda_{dB} \sim 35$ nm, is much longer than the width of the outermost potential well.

$$\frac{A}{2dF}\left[\tan^{-1}\left(\frac{x-x_0+dF}{\gamma/2}\right)-\tan^{-1}\left(\frac{x-x_0-dF}{\gamma/2}\right)\right]. \tag{5.1}$$

This expression is a convolution of a step function of width dF, representing the density of rotational states in the line, with a Lorentzian of width γ, representing the linewidth of the excitation lasers, with centers x_0 corresponding to the calculated vibrational energies and widths dF determined by the calculated dipole moments and the amplitude of the background electric field. The transition probabilities A correspond to the Franck-Condon factor for the transition into the trilobite state.

There is a significant modulation of the peak amplitudes for vibrational levels of opposite parity, with even v having larger amplitudes than odd v. The reason for this is that the thermal deBroglie wavelength of the ^{133}Cs atoms is long compared to the width of the potential well: $\lambda_{dB}(T = 40\ \mu\text{K}) \sim 35$ nm, while the potential wells are ~ 5 nm wide. Thus, the ground state wavefunction is nearly flat over this range, and odd vibrational wavefunctions tend to cancel out in the Franck-Condon factors. This odd-parity cancellation is akin to the Cooper minima in atomic ionization spectra [58]. In that case, Cooper found a difference in ionization cross sections between states without nodes (e.g. $1s$, $2p$, and $3d$), analogous to the even parity trilobite states, and states with nodes (e.g. $2s$), analogous to the odd parity trilobite states.

5.2.2 Linewidth Measurement

The linewidths of selected trilobite states are measured in order to determine the electric dipole moments of the states. The experimental setup is similar to the spectra measurement, except for the application of background electric fields, and scanning over a shorter range.

The detunings used in the linewidth measurements are the same as used in the spectra measurement, with the -377 MHz EIT peak and the -243 MHz EIT peak acting as references on each side of the trilobite peak to account for any laser drift. The 699 is scanned at 1 MHz per frequency step (with one dipole trap per frequency step). The timing is similar to the spectra measurement. Each laser pulse is 10 μs long and followed 5 μs later by an electric field pulse to push ions to the MCP. As in the measurement of the vibrational spectra, photoionization is used to ionize any Rydberg atoms created by the laser pulse.

An electric field in the vertical axis can be applied using plates inside the vacuum chamber. A voltage can be applied through a HV feedthrough, which is connected to the top electric field plate. The top electric field plate is connected to a central ring and the lower plate through resistors.

The applied voltage must be carefully calibrated so that any stray background field in the vertical dimension is canceled out. Any field in the transverse directions, however, cannot be canceled out with the apparatus. The calibration can be done by exciting Rydberg atoms at very high n and minimizing the

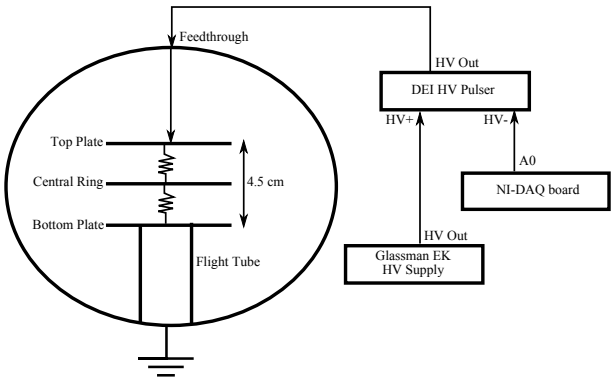

Figure 5.6: A schematic of the electric field apparatus in the UHV chamber. The output of the DEI pulser is connected through a feedthrough into the chamber to the top plate. A resistive network with a combined resistance of 3 kΩ connects the top plate through a central ring to the bottom plate. The top and bottom plates are separated by 4.5 cm. The bottom plate is connected to the flight tube and is electrically connected to the chamber, which is grounded.

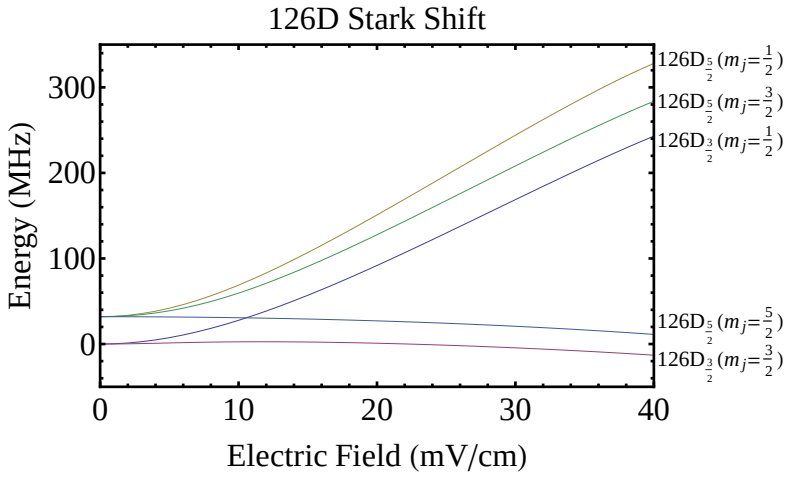

Figure 5.7: Stark shift curves for the $126D$ Rydberg state. At zero electric field, two peaks will be present in spectra: one corresponding to the $126D_{5/2}$ state, and another corresponding to the $126D_{3/2}$ state. As the electric field is applied, the peaks split and shift. The peak positions and splittings can be used to measure the electric field. The zero on the vertical scale corresponds to the $126D_{3/2}$ state at zero field.

Stark splittings of the m_J levels. We used the $126D$ state for this purpose. A calculated Stark splitting for $126D$ is shown in Fig. 5.7 and an experimental spectrum corresponding to a background field of 15 mV cm^{-1} is shown in Fig. 5.8. A spectrum taken around the Rydberg line shows multiple peaks, with the number of peaks and the splittings between the peaks depending on the electric field. The electric field can then be determined by matching the peak positions with the calculated m_J levels.

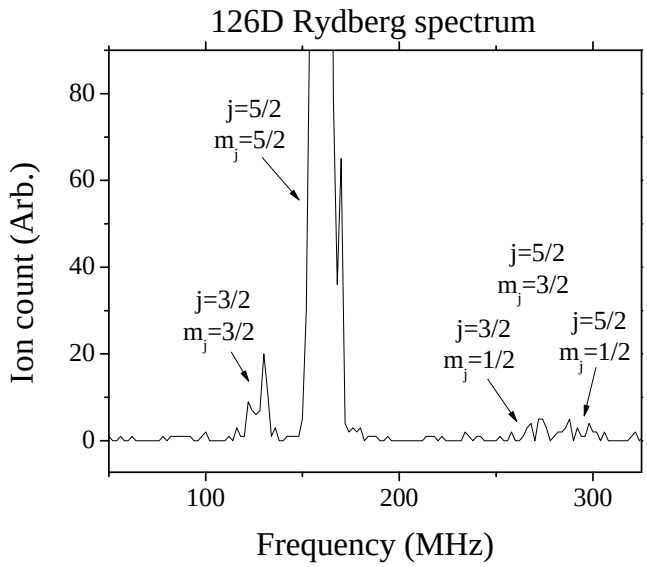

Figure 5.8: Experimental spectrum at $126D$ in the presence of a background electric field of 15 mV cm^{-1}. The large variance in the peak heights is due to the selection rules for the transition in the presence of the horizontally polarized excitation light.

This measurement indicated that the stray transverse background field is ~ 15 mV cm^{-1}, and that a field of -20 mV cm^{-1} must be applied to cancel out the stray fields in the vertical direction. These fields need to be remeasured occasionally as they vary with time. Over the course of ~ 6 months, the vertical electric field inside the chamber varied by ~ 20 mV cm^{-1}.

Three spectral absorption lines are selected for Stark shift measurements: the excited vibrational level at ~ -277 MHz, $v = 4$, in the potential energy curve correlating to the $37S + 6S$ limit, and the ground vibrational levels, $v = 0$, in the potential energy curves correlating to the $39S + 6S$ and $40S + 6S$ limits. The selected states are marked by arrows in Fig. 2.4. Spectra are taken at various fields and the widths of each of the peaks are fit to the function shown in Eqn. 5.1, where the transition probability A, the peak center x_0, and the spectral line broadening dF are fit parameters.

The density of states is a step function because the rotational constant of the molecule is small: 7 kHz, which is smaller than the radiative linewidth of the state, ~ 50 kHz. As a result the different possible alignments of the molecule relative to the electric field are equally likely, with aligned and anti-aligned configurations having the greatest Stark shift, while perpendicular configurations have zero Stark shift. The line then appears broadened, rather than split, by the electric field, and due to the density of states the line has a flat top.

Molecules with permanent electric dipole moments exhibit Stark shifts that are linear with electric field. Thus, the peak widths should vary linearly with

the applied electric field. However, due to the presence of a stray transverse background field, the observed functions are non-linear at small fields. The total electric field that the atoms experience can be expressed as $\vec{F} = F_a\hat{z} + F_t\hat{x}$, where the $\hat{z}$ axis is vertical in the chamber, the $\hat{x}$ axis is along the direction of the background electric field, F_a is the applied vertical electric field, and F_t is the stray transverse electric field. The function used to fit these relationships is $d\sqrt{F_a^2 + F_t^2}$, where d is the dipole moment. F_t and d are parameters of the fit.

Results

The linewidths for the excited vibrational level at ~ -277 MHz, $v = 4$, in the potential energy curve correlating to the $37S + 6S$ limit, and the ground vibrational levels, $v = 0$, in the potential energy curves correlating to the $39S$+$6S$ and $40S + 6S$ limits are shown in Fig. 5.9. The graphs show the width of the spectral line dF, fit according to Eqn. 5.1, as a function of the applied field F_a. At applied fields greater than ~ 10 mV cm^{-1}, the broadening is approximately linear. At lower fields, the broadening is nonlinear due to the presence of the background field of ~ 15 mV cm^{-1}.

For the ~ 277 MHz vibrational peak near the $37S + 6S$ asymptote, the measured electric dipole moment is $D = 2330 \pm 400$ Debye, while we obtained $D = 2310 \pm 250$ Debye and $D = 1915 \pm 164$ Debye for the $v = 0$ level in the outer wells shown in Fig. 2.4 near the $39S + 6S$ and $40S + 6S$ asymptotes, respectively. The dipole moment for $37S + 6S$ is within 1% of the predicted

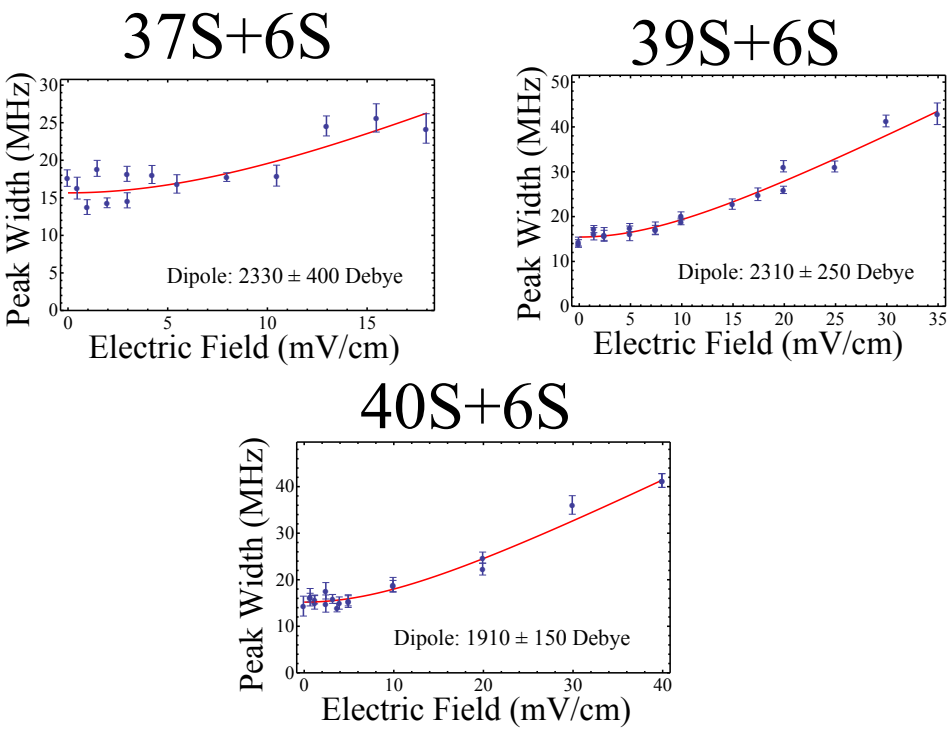

Figure 5.9: Linewidths as a function of applied field F_a for the -275 MHz peak corresponding to $37S + 6S$, and the $v = 0$ states corresponding to $39S+6S$ and $40S+6S$. The error bars for the dipole moments are determined as the background field and two-photon laser linewidth are varied within the measurement error. The error bars on the linewidth data are the statistical error of the linewidth fit.

theoretical value, and the dipole moments for $39S + 6S$ and $40S + 6S$ are within 13% and 6% of the predicted theoretical values, respectively. Due to the mixing with hydrogenic levels discussed in Chapter 2, the dipole moments are 10-100 times greater than those of previously-observed trilobite-like molecules [1, 2].

There are several sources of uncertainty in the dipole moment measurement. The largest source of uncertainty is the uncertainty in the background electric field. For the $39S+6S$ case, this gives a contribution of ~ 220 Debye to the error. Another contribution to the uncertainty comes from the statistical fit of the width data. For the $39S + 6S$ case, this gives a contribution to the uncertainty of ~ 50 Debye.

Some sources of uncertainty are also present in the theoretical dipole moments. Uncertainty in the value of the s-wave scattering length results in uncertainty in the hydrogenic admixtures and dipole moments. The adjustment to the theoretical value for the s-wave scattering length was determined by adjusting the scattering length to fit the experimental spectra. These sources of uncertainty are estimated to cause an uncertainty of 100 Debye in the theoretical values. The experimental and theoretical values for the dipole moments match to within the uncertainty when all the sources of uncertainty in the experimental and theoretical values are considered.

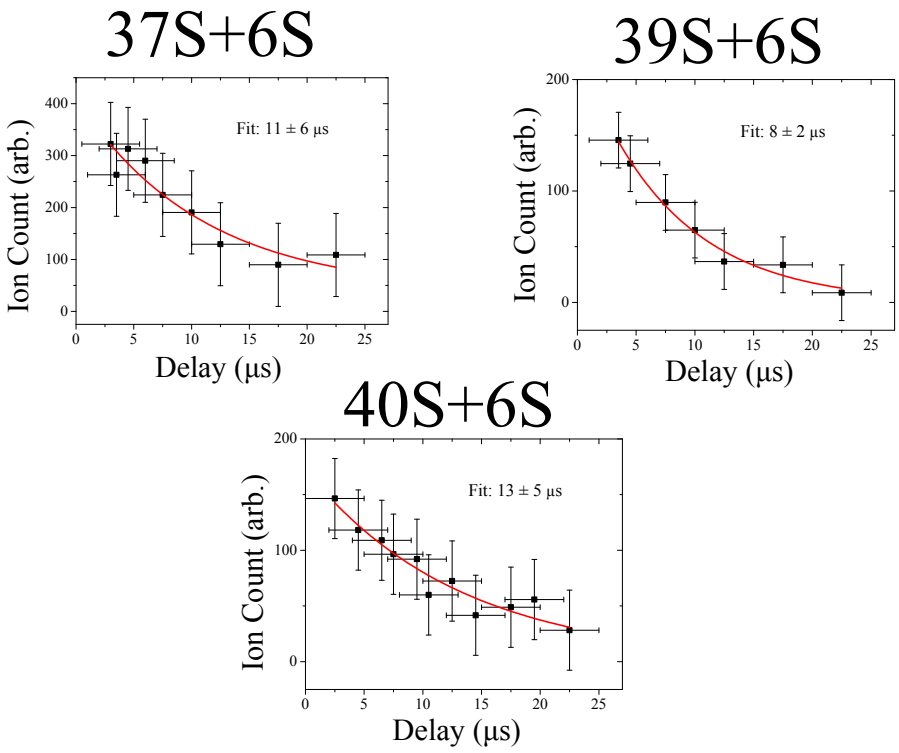

Figure 5.10: Ion counts for the $v = 4$ level in the potential energy curve correlating to the $37S + 6S$ limit, and $v = 0$ in potential energy curves correlating to the $39S + 6S$ and $40S + 6S$ limits, as a function of the delay between excitation and ionization. The uncertainties in the delay time are due to the width of the 5 μs laser pulses used. The vertical error bars are the statistical error in the ion counts.

5.2.3 Lifetime measurement

Lifetimes are measured for the excited vibrational level at ~ -277 MHz, $v = 4$, in the potential energy curve correlating to the $37S + 6S$ limit, and the ground vibrational levels, $v = 0$, in the potential energy curves correlating to the $39S + 6S$ and $40S + 6S$ limits. The lifetimes are measured by varying the time between excitation and ionization. To ensure that the time between excitation and ionization is known, it is necessary to use pulsed electric field ionization rather than photoionization. To achieve this, the amplitude of the electric field pulse is increased to 300 Vcm^{-1} and the FORT is turned off for a 40 μs period around the excitation pulse.

Because turning off the FORT causes atoms to be lost from the trap due to thermal expansion, the trap lifetime is significantly reduced. To account for this, the pulse train is reduced to 100 pulses in 50 ms. For each data point, 10000 pulses are performed, requiring the FORT to be loaded 100 times. The ion count inside the time-of-flight region of interest over the 10000 pulses is counted by the MCA. Three sets of 10000 pulses are taken for each point to acquire a statistical estimate of the error. A timing diagram for the probe sequence is shown in Fig. 5.11.

Due to the small signals on the trilobite peak, a good frequency reference is required in order to keep the laser on resonance. To accomplish this, the EIT setup is adjusted to place an EIT peak at the frequency position of the trilobite

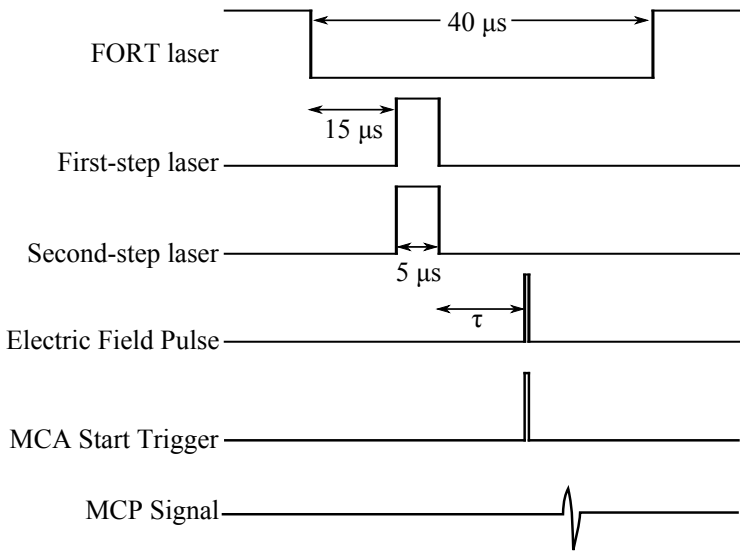

Figure 5.11: Timing diagram for the lifetime measurement. This pulse sequence is repeated 100 times for each dipole trap at a rate of 2 kHz. The delay τ between excitation and ionization is varied to measure the lifetime. The FORT is turned off during the probing to prevent photoionization. The width of the electric field pulse is 500 ns. The delay between the FORT off signal and the laser pulse is set so that the FORT is fully off before the laser pulse occurs.

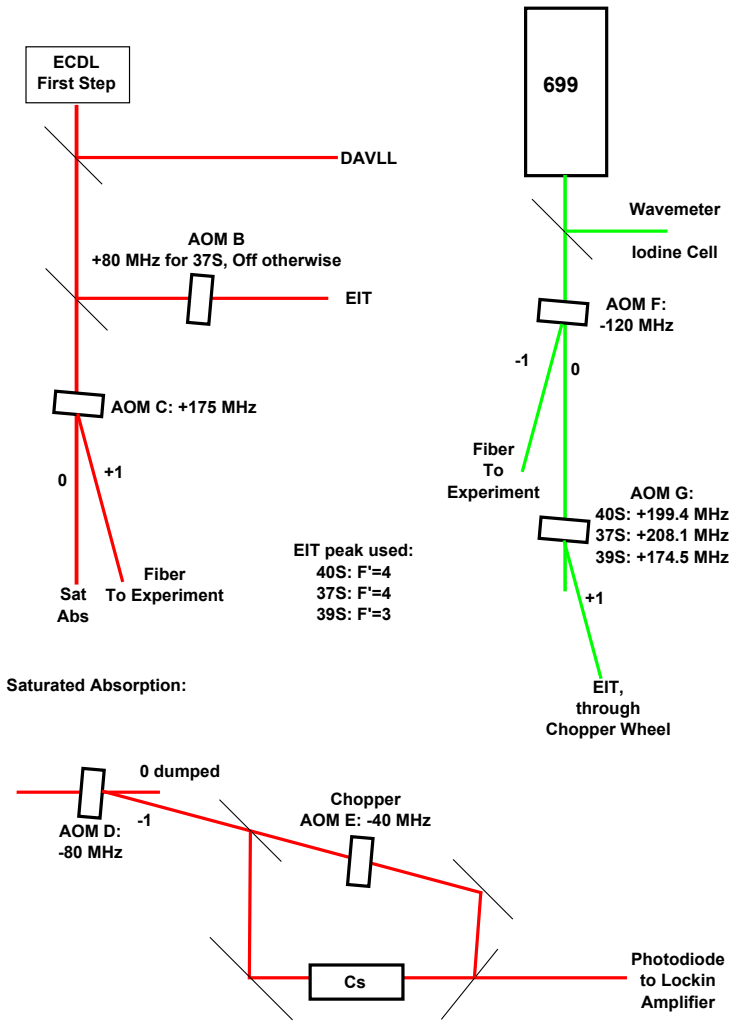

Figure 5.12: AOM detunings used in the trilobite lifetimes experiment. Different detunings were used for each molecular peak measured so that an EIT line could be matched to each molecular peak.

peak, and the laser is kept on resonance by manually adjusting the scan voltage of the 699 to keep the EIT signal maximized. A diagram showing the AOM frequencies used is shown in Fig. 5.12.

Results

The lifetime data for the three states whose dipole moments are measured is shown in Fig. 5.10. The data is acquired by taking the ion count inside the time-of-flight region of interest and extracting the signal by subtracting a normalized background ion count from outside the region of interest. The subtraction is done to remove background noise from the signal. The data presented in Fig. 5.10 is extracted from the raw data using the formula:

$$\text{Ion count} = \mathrm{N}(\mathrm{t}_{\mathrm{ROI},2} - \mathrm{t}_{\mathrm{ROI},1}) - \mathrm{N}(\mathrm{t}_{\mathrm{bg},2} - \mathrm{t}_{\mathrm{bg},1})\frac{\mathrm{t}_{\mathrm{bg},2} - \mathrm{t}_{\mathrm{bg},1}}{\mathrm{t}_{\mathrm{ROI},2} - \mathrm{t}_{\mathrm{ROI},1}}, \tag{5.2}$$

where $t_{ROI,i}$ are the beginning and ending times for the region of interest where the Cs^+ ions are present, and $t_{bg,i}$ are the beginning and ending times chosen for the background ion count. The ion counts are then fit to an exponential decay function to extract the lifetime.

The uncertainty in the timing in the lifetime data comes from the finite (5 μs) width of the excitation pulse. Because the atom could be excited at any time during the pulse, there is an uncertainty in the time between the excitation and the ionization. This is accounted for by assigning the mean delay to correspond

to an atom being excited in the middle of the pulse, with the uncertainty being plus or minus half the width of the pulse, giving an uncertainty of ± 2.5 μs for each point. The uncertainty in the ion counts comes from the standard deviation of the measurements performed.

The measured lifetimes are 11 ± 6 μs for the -275 MHz peak corresponding to the $37S+6S$ asymptote, 8 ± 2 μs for the $v = 0$ state corresponding to $39S+6S$, and 13 ± 5 μs for the $v = 0$ state corresponding to $40S + 6S$. These lifetimes are considerably shorter than the expected lifetime for the nS atomic state. The lifetime for the $40S$ state with radiative and blackbody decay included is 37 μs [29]. The lifetimes for the $(n-4)F$ states are shorter and are comparable to the measured lifetimes of the trilobite states. For the $36F$ state, the lifetime including radiative and blackbody decay is 18 μs [22].

This shortened lifetime is indicative of an admixture of the $((n-4)F+6S)^3\Sigma$ state into the $(nS + 6S)^3\Sigma$ states, which agrees with the result from the dipole measurement, where the very large dipoles are indicative of a large ($\sim 60-90\%$) admixture. However, this result does not suggest a very large admixture of the $((n-4)(L \gg 3)+6S)^3\Sigma$ states, as the states with very large L have significantly longer lifetimes than the $(n-4)F$ state. For the circular state $36(L = 35)$, the lifetime is 127 μs, primarily due to blackbody decay [59]. However, the circular state, which has the longest radiative lifetime, has the additional requirement that $|m| = n-1$, such that there is only one dipole transition possible out of the circular state [60], and it is unlikely that there is a significant component of

the trilobite state with a maximized value of m.

Tunneling out of the potential well is possible, and could shorten the lifetimes of the states. To determine whether this was a potential issue, tunneling lifetimes were calculated using a semi-classical approximation for the states observed in the experiment. In this approximation the vibrational wavefunction is used to estimate the probability of the barrier being passed at the inner turning point:

$$P = \int_0^{r_{tp}} |u(R)|^2 \mathrm{d}R, \tag{5.3}$$

where r_{tp} is the internuclear distance at the inner turning point and $u(R)$ is the vibrational wave function. This probability is then used to determine a lifetime for the state by estimating the rate at which the molecule encounters the inner turning point. The calculated lifetimes are several orders of magnitude longer than the timescales involved in the experiment, and thus tunneling is not an important factor in the lifetimes of the states.

5.3 "Butterfly" molecules

Experiments were performed on "butterfly" states asymptotically corresponding to the $31S + 6S$ and $32S + 6S$ systems. In these cases, the p-wave interaction dominates over the s-wave interaction, allowing the presence of molecules with Π symmetry.

Because these molecules exhibit Π symmetry, they follow different selection rules for excitation than the Σ molecules. This can be observed by varying

the polarization of the excitation light. When the excitation light is polarized linearly parallel to the electric field, $\Delta M = 0$ transitions are excited, resulting in a single line that broadens in an electric field, similar to the trilobite molecule states described above. However, when the excitation light is polarized linearly, perpendicular to the electric field, $\Pi = \pm 1$ transitions are excited, resulting in a line that splits into two lines, a case which does not occur for the Σ molecules.

The potential curves for the state of interest are shown in Fig. 5.13. The potential wells that contain the vibrational levels seen in our spectra are located between -4 GHz and the atomic line at 0 GHz. The p-wave portion of the interaction is far larger relative to the s-wave portion than in the higher n cases, resulting in a much larger splitting between the $M_J = 0$ and $M_J = \pm 1$ potential curves.

5.3.1 Experiment

Two experiments were performed on the $31S + 6S$ and $32S + 6S$ systems. First, the spectra to the red of the atomic line were taken, and then the behavior of the lowest bound states were observed as an electric field was applied. The experiments performed are similar to the ones used at higher n. With hydrogenic admixtures in the $n = 31, 32$ case of $> 90\%$, the signal level is smaller than for the higher n. Another factor in the lower signal level is that the wells in the potential curves, depicted in Fig. 5.13, are at closer internuclear separations than at higher n, and thus yield a lower signal at an equivalent density.

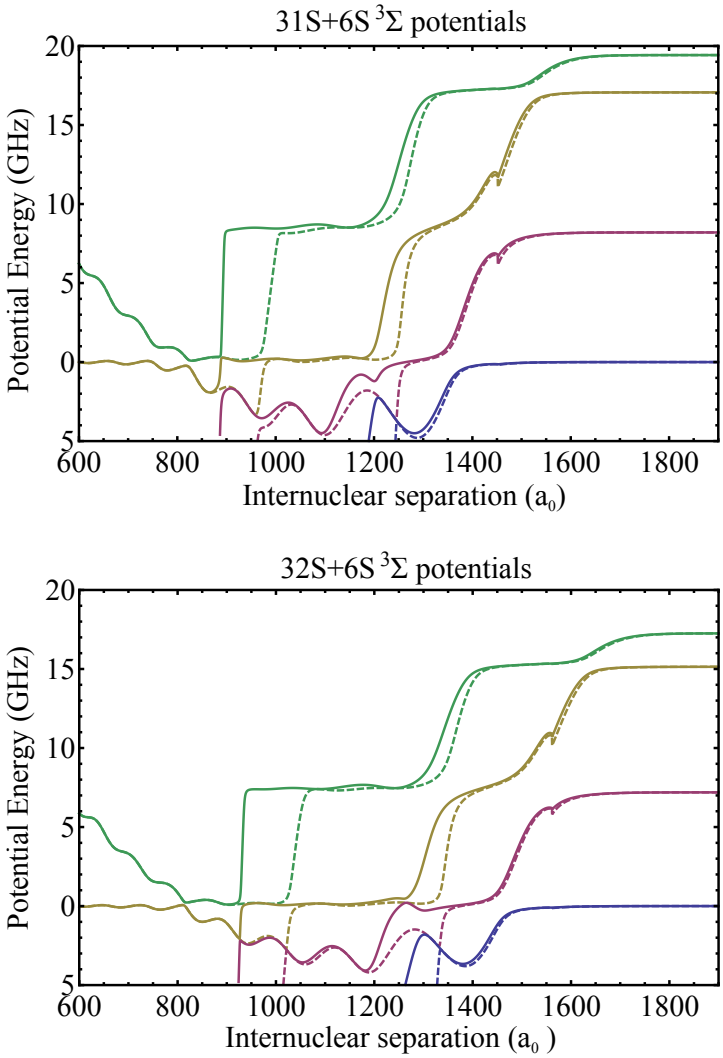

Figure 5.13: Potential curves for the $31S + 6S$ and $32S + 6S$ systems. The potential wells of interest for our spectra are located between -4 GHz and the atomic line at 0 GHz.

The spectra were produced by scanning in 500 MHz sections, starting from the Rydberg line. EIT was used for frequency markers within ~ 1 GHz of the atomic Rydberg line, but further from the Rydberg line the EIT lines were inaccessible. As a result, beyond 1 GHz from the atomic line, the sections of the spectra were patched together by locating the same molecular resonances in different sections and setting their frequencies to be equal.

For the electric field measurements, the furthest-detuned vibrational level was selected from the $n = 31, 32$ spectra. For the $31S + 6S$ case, this line is at ~ -3500 MHz and for the $32S + 6S$ case, the line is at ~ -3600 MHz. The polarization of the second-step excitation light is set using a $\lambda/2$ waveplate following the output of the optical fiber which the second-step laser is coupled through.

5.3.2 Results

The spectra to the red of the $31S+6S$ and $32S+6S$ states are shown in Fig. 5.14. Numerous lines appear in the spectra between ~ -3600 MHz and the atomic line. Because the potential curve structure for these states is more complicated than at higher n, interpretation of the spectra is more difficult.

The lowest detected vibrational level for the two spectra were used for electric field measurements. These measurements were performed in the presence of two different polarizations of excitation light: one perpendicular to the electric field and the other parallel to the electric field. In the resulting spectra, when a

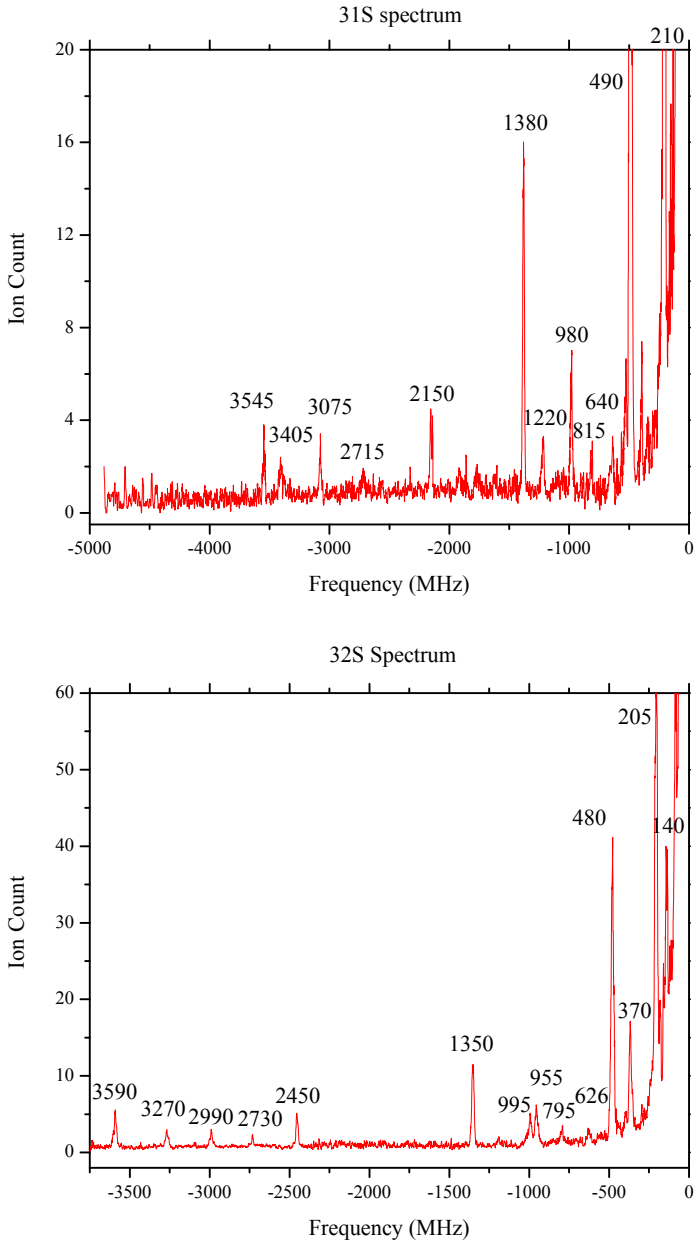

Figure 5.14: Spectra red of the $31S + 6S$ and $32 + 6S$ atomic transitions.

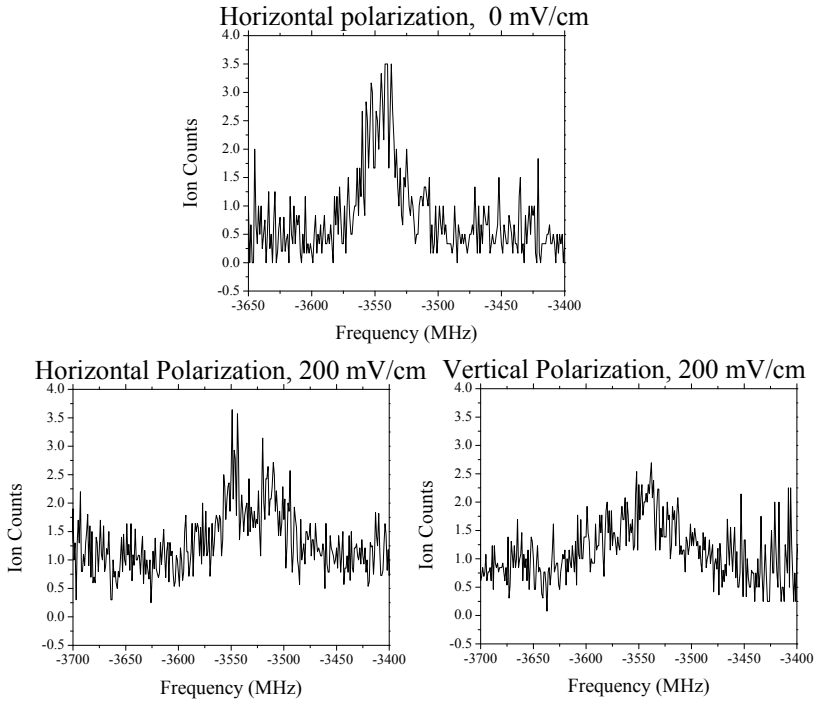

Figure 5.15: Spectra depicting the lowest observed vibrational level of $31S+6S$ in three cases: when zero field is applied, when 200 mV cm^{-1} is applied and the excitation light is vertically polarized (parallel to the electric field), and when 200 mV cm^{-1} is applied and the excitation light is perpendicular to the electric field.

perpendicular (horizontal) polarization is used, the line splits, with a splitting that is dependent on the applied electric field. When a parallel polarization is used, no such splitting occurs. This can be seen in Fig. 5.15, where the spectral line at zero field is compared to the spectral line at 200 mV cm^{-1} with horizontal and vertical polarizations.

To determine how the splitting increases as a function of the electric field

in the presence of perpendicularly polarized excitation light, the spectral line was observed at various electric fields. An example of the splitting as an electric field is applied can be seen in Fig. 5.16. The datasets shown in the figure are at fields of 0 mV cm^{-1}, 200 mV cm^{-1}, and 400 mV cm^{-1}. As the field is applied, the line splits in two, with a splitting that increases linearly with the electric field. The splitting as a function of the electric field for the lowest vibrational levels in $n = 31, 32$ is shown in Fig. 5.17. The slope of the line is 0.070 ± 0.003 MHz/(mV cm^{-1}), which corresponds to a dipole moment of 140 ± 10 Debye. While this dipole moment is significantly smaller than the other states observed (likely due to the smaller internuclear distances at which the p-wave dominated states form), it is still indicative of a significant hydrogenic admixture.

5.4 Conclusion

To summarize, molecular states with very large dipole moments ~ 2000 Debye were observed. These states have $\sim 60 - 90\%$ admixture in the hydrogenic states, resulting in molecular states that are primarily trilobite in character. The remaining admixture in the S state facilitates photoassociation into these states. While both $M_J = 0$ and $M_J = \pm 1$ levels are accessible in the dipole trap, for the outermost well at $n = 37, 39, 40$ the splittings between the M_J projections are small enough that they are not experimentally distinguishable.

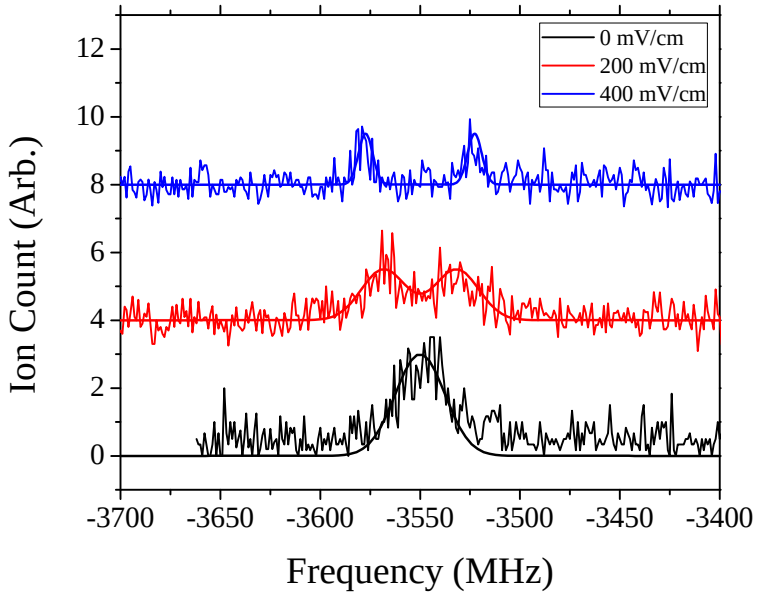

Figure 5.16: Splitting of the lowest vibrational level in the $31S + 6S$ and $32S + 6S$ spectra at three different electric fields in the presence of perpendicularly-polarized excitation light. Gaussian fits to the peaks are superimposed.

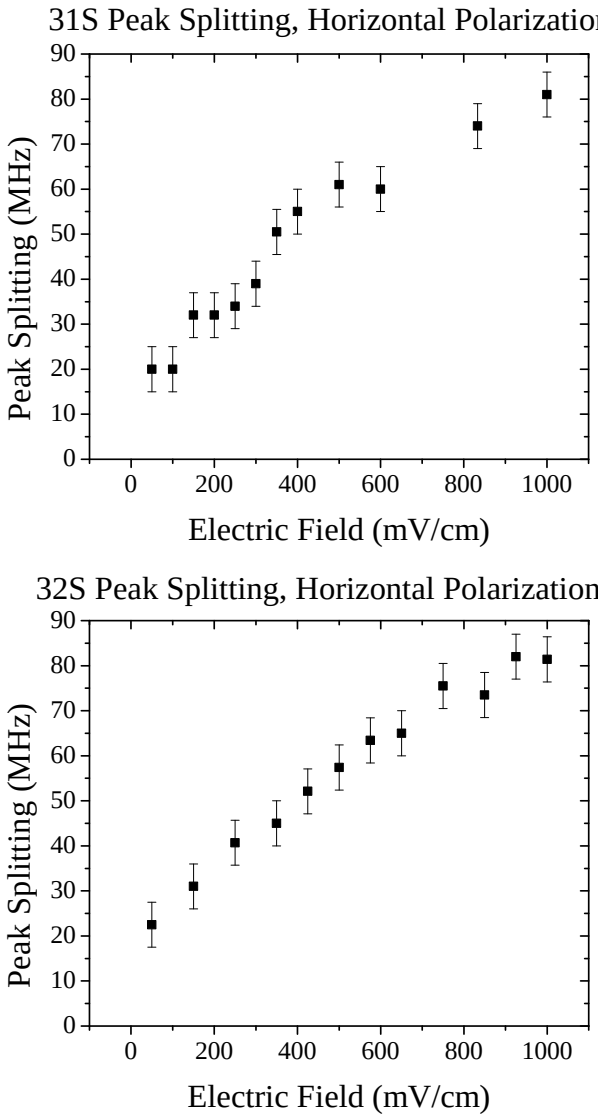

Figure 5.17: Splitting of the lowest vibrational level in the $31S + 6S$ and $32S + 6S$ spectra as a function of electric field in the presence of perpendicularly-polarized excitation light. The error bars reflect the uncertainties in the splittings due to drift in the second-step laser lock.

This experiment expands on the work in [2], where a hydrogenic admixture of $\sim 1\%$ in blue-detuned potential wells in the $nS + 6S$ system in ^{133}Cs, where $31 \leq n \leq 34$, resulted in dipole moments of $20 - 100$ Debye. The molecular states in ^{133}Cs have significantly different properties than the states that have been observed in ^{87}Rb S-states [11, 12, 1], where hydrogenic admixtures of $< 1\%$ yield dipoles of ~ 1 Debye, and D-states [13, 14] which have dipole moments smaller than the S-states.

The small non-integer portion of the S state quantum defect, as well as the ~ 8 meV p-wave resonance and large spin-orbit coupling in ^{133}Cs, results in the large mixing between the $nS + 6S$ and $(n-4)(L \geq 3) + 6S$ potentials. This mixing allows the large hydrogenic admixtures in the red-detuned potential wells. These large admixtures allow the large permanent electric dipole moments that were observed in the experiment.

Additionally, there is strong evidence of the presence of "butterfly" states – p-wave dominated high-angular momentum states – in the spectra red-detuned from $31S + 6S$ and $32S + 6S$. The electric field behavior of the spectral lines is consistent with a molecule which can exhibit Π symmetry, characteristic of a butterfly state. The electric field dependence of the splitting of the spectral lines in the presence of perpendicularly-polarized excitation light indicates that the molecule has a large dipole moment on the order of hundreds of Debye.

Chapter 6

Conclusions and Future Directions

In conclusion, we observed ultralong-range Cs "trilobite" molecules with dipole moments of ~ 2000 Debye. In addition we have observed "butterfly" molecules with large dipole moments, which are distinguished from the trilobite states by their symmetry properties. The energies and dipole moments of the states are in agreement with calculations performed by our collaborators, Seth Rittenhouse from Western Washington University and Hossein Sadeghpour from ITAMP at Harvard University. The dipole moments are the largest of any homonuclear diatomic system to date, and are one to two orders of magnitude larger than the previous largest dipole moments, $20 - 100$ Debye, reported in [2]. They are also two orders of magnitude larger than the dipole moment of RbI (11.5 Debye), the largest dipole moment reported in [61].

The observation of these very large dipole moments has potential applications in various areas. For example, in quantum computing there is great interest in using systems of atoms and molecules that can interact at large range and be controlled with small electric fields. These molecules would be very useful for this purpose because of the large dipole moments. In addition, the method of photoassociating these molecules by exploiting admixtures between dipole transition-forbidden polar states and dipole transition-allowed non-polar states allows flexibility in using these molecular states in quantum computing

applications.

Our study of these trilobite and butterfly states was made possible by the additions that were made to the experimental apparatus. A new 50 W dipole trapping laser enabled the achievement of a peak density of 5×10^{13} cm^{-3}, facilitating the photoassociation of Rydberg molecules. Improvements to the Zeeman slower enabled its use in the experiment, improving the lifetime of the dipole trap by reducing the background vapor pressure in the vacuum chamber.

Additionally, we have calculated Rydberg-Rydberg pair potential curves and analyzed them for several different systems. In the case of the ^{85}Rb $nD + nD$ system described in Section 3.2, a Landau-Zener analysis of avoided crossings in the potential curves corresponding to the $nD + nD$ and $(n+2)P + (n-2)(L \geq 3)$ states gave results that explain the $(n+2)P$ atom yield observed in the experiment. We performed calculations for the $90D_{5/2} + 90D_{5/2}$ system in ^{133}Cs in a 100 mV cm^{-1} field which indicate a strong anisotropy due to the induced dipoles of the atoms, and have performed scattering calculations on these potential surfaces. Pair interactions can also be used to explain the behavior of some many-body systems, such as the Rydberg aggregations described in Section 3.4. In the $37D + 37D$ system in ^{85}Rb in fields of ~ 1.65 V cm^{-1}, we have shown that we can use our potential curve calculations to predict the lineshapes seen in the experiment, which result from dipole blockade of the excitation into the Rydberg state.

Future directions for the experiment include observations of D-state Rydberg

molecules in Cs. The D states in Cs are energetically isolated from hydrogenic states, yielding molecules with small dipole moments which contrast with the molecular states associated with the S states discussed in this thesis.

Another possible future direction for the experiment is the detection of Rydberg molecules corresponding to high-n states. As n increases, the radius of the Rydberg electron increases, causing the Rydberg electron to occupy a larger volume making excitation of trimers, tetramers, and higher-order states more likely. This has already been observed in ^{87}Rb [15], but in ^{133}Cs, this effect is combined with the dipole moments due to admixtures with hydrogenic states. This can produce interesting physics when considering the behavior of multi-body states. For example, for trimers, the energetically-favored state is likely to be a linear alignment, analogous to the CO_2 molecule. Such a molecule would have zero dipole moment, despite the individual bonds having very large dipole moments.

With the recent addition of a new excitation laser to the experiment, the possibility of doing two-color spectroscopy on Rydberg pair states is opened. This greatly increases the number of pair states accessible to the experiment, opening the possibility of interesting new dynamics and further study of macrodimer states.

References

[1] W. Li, T. Pohl, J. M. Rost, S. T. Rittenhouse, H. R. Sadeghpour, J. Nipper, B. Butscher, J. B. Balewski, V. Bendkowsky, R. Löw, and T. Pfau, Science **334**, 1110 (2011).

[2] J. Tallant, S. T. Rittenhouse, D. Booth, H. R. Sadeghpour, and J. P. Shaffer, Phys. Rev. Lett. **109**, 173202 (2012).

[3] C. H. Greene, A. S. Dickinson, and H. R. Sadeghpour, Phys. Rev. Lett. **85**, 2458 (2000).

[4] L. D. Carr, D. DeMille, R. V. Krems, and J. Ye, New Journal of Physics **11**, 055049 (2009).

[5] S. Ospelkaus, K.-K. Ni, D. Wang, M. H. G. de Miranda, B. Neyenhuis, G. Qumner, P. S. Julienne, J. L. Bohn, D. S. Jin, and J. Ye, Science **327**, 853 (2010).

[6] H. Weimer, M. Muller, I. Lesanovsky, P. Zoller, and H. P. Buchler, Nat Phys **6**, 382 (2010).

[7] M. Lukin, M. Fleischhauer, R. Cote, L. Duan, D. Jaksch, J. Cirac, and P. Zoller, Phys. Rev. Lett. **87**, 037901 (2001).

[8] E. Fermi, Il Nuovo Cimento **11**, 157 (1934).

[9] Omont, A., J. Phys. France **38**, 1343 (1977).

[10] E. L. Hamilton, C. H. Greene, and H. R. Sadeghpour, Journal of Physics B: Atomic, Molecular and Optical Physics **35**, L199 (2002).

[11] V. Bendkowsky, B. Butscher, J. Nipper, J. P. Shaffer, R. Löw, and T. Pfau, Nature **458**, 1005 (2009).

[12] V. Bendkowsky, B. Butscher, J. Nipper, J. B. Balewski, J. P. Shaffer, R. Löw, T. Pfau, W. Li, J. Stanojevic, T. Pohl, and J. M. Rost, Phys. Rev. Lett. **105**, 163201 (2010).

[13] D. A. Anderson, S. A. Miller, and G. Raithel, Phys. Rev. Lett. **112**, 163201 (2014).

[14] A. T. Krupp, A. Gaj, J. B. Balewski, P. Ilzhöfer, S. Hofferberth, R. Löw, T. Pfau, M. Kurz, and P. Schmelcher, Phys. Rev. Lett. **112**, 143008 (2014).

[15] A. Gaj, A. T. Krupp, J. B. Balewski, R. Lw, S. Hofferberth, and T. Pfau, Nat. Commun. **5**, 4546 (2014).

[16] D. Tong, S. M. Farooqi, J. Stanojevic, S. Krishnan, Y. P. Zhang, R. Côté, E. E. Eyler, and P. L. Gould, Phys. Rev. Lett. **93**, 063001 (2004).

[17] W. Li, P. J. Tanner, and T. F. Gallagher, Phys. Rev. Lett. **94**, 173001 (2005).

[18] M. Mudrich, N. Zahzam, T. Vogt, D. Comparat, and P. Pillet, Phys. Rev. Lett. **95**, 233002 (2005).

[19] A. Fioretti, D. Comparat, C. Drag, T. F. Gallagher, and P. Pillet, Phys. Rev. Lett. **82**, 1839 (1999).

[20] I. Mourachko, D. Comparat, F. de Tomasi, A. Fioretti, P. Nosbaum, V. M. Akulin, and P. Pillet, Phys. Rev. Lett. **80**, 253 (1998).

[21] K. R. Overstreet, A. Schwettmann, J. Tallant, D. Booth, and J. P. Shaffer, Nat. Phys. **5**, 581 (2009).

[22] T. F. Gallagher, *Rydberg Atoms*, 1st ed. (Cambridge University Press, New York, 1994).

[23] K.-H. Weber and C. J. Sansonetti, Phys. Rev. A **35**, 4650 (1987).

[24] W. Li, I. Mourachko, M. W. Noel, and T. F. Gallagher, Phys. Rev. A **67**, 052502 (2003).

[25] J. Han, Y. Jamil, D. V. L. Norum, P. J. Tanner, and T. F. Gallagher, Phys. Rev. A **74**, 054502 (2006).

[26] P. Goy, J. M. Raimond, G. Vitrant, and S. Haroche, Phys. Rev. A **26**, 2733 (1982).

[27] M. Marinescu, H. R. Sadeghpour, and A. Dalgarno, Phys. Rev. A **49**, 982 (1994).

[28] F. Salvat, J. M. Fernández-Varea, and W. Williamson, Computer Physics Communications **90**, 151 (1995).

[29] I. I. Beterov, I. I. Ryabtsev, D. B. Tretyakov, and V. M. Entin, Phys. Rev. A **79**, 052504 (2009).

[30] J. Tallant, D. Booth, and J. P. Shaffer, Phys. Rev. A **82**, 063406 (2010).

[31] A. L. d. Oliveira, M. W. Mancini, V. S. Bagnato, and L. G. Marcassa, Phys. Rev. A **65**, 031401 (2002).

[32] V. A. Nascimento, L. L. Caliri, A. L. de Oliveira, V. S. Bagnato, and L. G. Marcassa, Phys. Rev. A **74**, 054501 (2006).

[33] M. Saffman and T. G. Walker, Phys. Rev. A **72**, 022347 (2005).

[34] A. Schwettmann, K. R. Overstreet, J. Tallant, and J. P. Shaffer, Journal of Modern Optics **54**, 2551 (2007).

[35] C. Bahrim, U. Thumm, and I. I. Fabrikant, Journal of Physics B: Atomic, Molecular and Optical Physics **34**, L195 (2001).

[36] M. Scheer, J. Thøgersen, R. C. Bilodeau, C. A. Brodie, H. K. Haugen, H. H. Andersen, P. Kristensen, and T. Andersen, Phys. Rev. Lett. **80**, 684 (1998).

[37] S. P. Andreev, B. M. Karnakov, V. D. Mur, and V. A. Polunin, Sov. Phys. JETP **86**, 866 (1984).

[38] M. L. Zimmerman, M. G. Littman, M. M. Kash, and D. Kleppner, Phys. Rev. A **20**, 2251 (1979).

[39] J. S. Cabral, J. M. Kondo, L. F. Gonalves, L. G. Marcassa, D. Booth, J. Tallant, and J. P. Shaffer, New Journal of Physics **12**, 093023 (2010).

[40] D. Jaksch, J. I. Cirac, P. Zoller, S. L. Rolston, R. Côté, and M. D. Lukin, Phys. Rev. Lett. **85**, 2208 (2000).

[41] C. Boisseau, I. Simbotin, and R. Côté, Phys. Rev. Lett. **88**, 133004 (2002).

[42] M. R. Flannery, D. Vrinceanu, and V. N. Ostrovsky, Journal of Physics B: Atomic, Molecular and Optical Physics **38**, S279 (2005).

[43] J. S. Cabral, J. M. Kondo, L. F. Gonalves, V. A. Nascimento, L. G. Marcassa, D. Booth, J. Tallant, A. Schwettmann, K. R. Overstreet, J. Sedlacek, and J. P. Shaffer, Journal of Physics B: Atomic, Molecular and Optical Physics **44**, 184007 (2011).

[44] T. J. Carroll, K. Claringbould, A. Goodsell, M. J. Lim, and M. W. Noel, Phys. Rev. Lett. **93**, 153001 (2004).

[45] C. Zener, Royal Society of London Proceedings Series A **137**, 696 (1932).

[46] H. Weimer, R. Löw, T. Pfau, and H. P. Büchler, Phys. Rev. Lett. **101**, 250601 (2008).

[47] R. Löw, H. Weimer, U. Krohn, R. Heidemann, V. Bendkowsky, B. Butscher, H. P. Büchler, and T. Pfau, Phys. Rev. A **80**, 033422 (2009).

[48] F. D. Colavecchia, F. Mrugaa, G. A. Parker, and R. T Pack, The Journal of Chemical Physics **118**, 10387 (2003).

[49] R. T. Pack and G. A. Parker, The Journal of Chemical Physics **87**, 3888 (1987).

[50] A. Urvoy, F. Ripka, I. Lesanovsky, D. Booth, J. P. Shaffer, T. Pfau, and R. Löw, ArXiv e-prints 1408.0039 (2014).

[51] J. Stanojevic, R. Côté, D. Tong, E. E. Eyler, and P. L. Gould, Phys. Rev. A **78**, 052709 (2008).

[52] W. Demtröder, *Laser Spectroscopy*, 2nd ed. (Springer-Verlag, Berlin, 1996).

[53] C. Hoffmann, Ph.D. thesis, University of Heidelberg, 2013.

[54] K. R. Overstreet, J. Franklin, and J. P. Shaffer, Rev. Sci. Inst. **75**, 4749 (2004).

[55] A. Schwettmann, J. Sedlacek, and J. P. Shaffer, Review of Scientific Instruments **82**, (2011).

[56] D. A. Steck, Alkali D Line Data, available online at http://steck.us/alkalidata, (revision 2.1.4, December 23, 2010).

[57] T. Weber, J. Herbig, M. Mark, H.-C. Nägerl, and R. Grimm, Science **299**, 232 (2003).

[58] J. W. Cooper, Phys. Rev. **128**, 681 (1962).

[59] T. Xia, X. L. Zhang, and M. Saffman, Phys. Rev. A **88**, 062337 (2013).

[60] R. G. Hulet, E. S. Hilfer, and D. Kleppner, Phys. Rev. Lett. **55**, 2137 (1985).

[61] *CRC Handbook of Chemistry and Physics*, 95th ed., edited by W. M. Haynes (CRC Press, London, 2014).

Appendix A

Usage of the Rycol Program

Rydberg-Rydberg potentials are generated using a program called Rycol. There are two primary components to Rycol: a Mathematica notebook and a Fortran program. The Mathematica notebook calculates the Stark shifts of the individual atomic states and generates a list of pair states to be included in the calculation. The output data from the Mathematica notebook is given as input to the Fortran program, which calculates potential curves and can also be configured to calculate eigenvectors of the pair state Hamiltonian.

A.1 Rycol Mathematica notebook

There are two versions of the Mathematica notebook. One is used in the anisotropic case, in which the internuclear axis is not parallel to the electric field axis. In this case, $M = m_{J1} + m_{J2}$ is not conserved and a rotation must be applied to the pair state Hamiltonian. The other version is used in the isotropic case. The version for the isotropic case can generate the angular matrix terms required for the Fortran program in either sparse or non-sparse format.

The first section of both versions of the Mathematica notebook is called "Initial Parameters", which contains parameters which specify which directories should be used for input and output, as well as important parameters for the calculation. The parameters that can be changed here are listed in Table A.1.

The main parameters that control the basis set used in the calculation are maxL, which controls the maximum orbital angular momentum L to be included in the basis set; nState, the principal quantum number n of the main state of interest; and lState, the orbital angular momentum L of the main state of interest. The parameter bgefieldmV contains the electric field in mV cm^{-1}. The various atom-dependent parameters are assigned based on the value of the parameter atomicnumber, which is the atomic number of the atom of interest (37 for Rb, 55 for Cs).

Four parameters determine the directories that the Mathematica notebook will write output to and look for wavefunctions in. The parameter basedir is the base directory which the other directories are located in. The parameter csStarkDirectory determines where the output directory will be relative to basedir, and radialDataDirectory determines where the notebook will look for wavefunction files. The parameter fortDirectory determines where the input files for the Fortran program will be written, and is given relative to csStarkDirectory.

If the output directories do not exist, the notebook will create them. It is important, though, that the directory containing the RADIAL wave function files be correct. The parameter AsymptoticEnergyWidth, which specifies the energy range (in cm^{-1}) over which pair states will be included in the calculation may need to be adjusted during the calculation to ensure the number of pair states included is correct.

The second section of the notebook, "Set Directories...", contains the file-

Table A.1: The parameters for the Rycol Mathematica notebook and their functions.

Parameter	Data Type	Function
basedir	String	Base directory
nState	Integer	Principal quantum number n
lState	Integer	Orbital angular momentum l
maxL	Integer	Maximum l to include in state list
bgefieldmV	Real	Electric field in mV cm^{-1}
atomicnumber	Integer	Atomic number (37 for Rb, 55 for Cs)
csStarkDirectory	String	Output directory relative to basedir.
radialDataDirectory	String	Directory with wave function data.
fortDirectory	String	Directory where output files for the Fortran program are written, relative to csStarkDirectory.
AsymptoticEnergyWidth	Real	Energy range, in cm^{-1} over which pair states will be included in the potential curve calculation.
rParams	3 Real	Maximum, minimum, and step size values for the internuclear distance R.

names used for outputting the radial matrix elements calculated later in the notebook. These parameters should not need to be changed.

The third section of the notebook, "Set the electric field conversion factors...", sets the conversion factor between V cm^{-1} and the atomic unit for electric field as well as the maximum and minimum m_J values to include in the calculation. The m_J values should be set automatically based on the parameter maxL from "Initial Parameters".

Next, in the section "Define the states needed...", the notebook determines what single-atom states to include in the Stark shift calculation, based on the parameters nState and lState from "Initial Parameters". Two lists are formed: hydrogenicstates, which contains a list of hydrogenic states where $L > 4$, and nonhydrogenicstates, where $L \leq 4$. These lists are then combined to form the list mystates, and the individual fine structure states are listed in mystatesFS.

In the following two sections, the notebook loads the wave functions for all the states in mystates. For the hydrogenic states, the wave functions are computed using the analytic formula for the hydrogen wave function. For the non-hydrogenic wave functions, the notebook imports wave functions previously calculated using a Fortran program called RADIAL [28], in which the Dalgarno potential [27] is used in the Schrödinger equation for the system. Two different methods are used to determine the wave functions because the Dalgarno potential accounts for the interaction between the electron and the ion core in the Rydberg atom, which is insignificant for high L. Because different grids were used for

different n in the calculation of the RADIAL wave functions, the notebook performs an interpolation on the imported wave functions and then assigns all the wave functions to use the same grid, to ensure that the integrals for the radial matrix elements are correct. It is important to note that the wave functions used by the notebook are $u(r) = R(r)/r$, where $R(r)$ is the full radial portion of the wave function. Because of this, the radial volume element in integrals is dr rather than $r^2 dr$; for example, the integral to calculate the normalization of the wave function can be expressed as $\int_0^\infty u^2(r)dr$.

After loading the wave functions, the notebook calculates the radial matrix elements $\langle \psi_{nl} | \, r \, | \psi_{n'l'} \rangle$. The numerical integration used by the notebook uses the rectangle approximation to the integral which, over the grid spacings used, produces accurate results relatively quickly compared to other methods. The calculated matrix elements are written to a file in the output directory, which can be reloaded later by using the "Load in precalculated radial matrix elements" section. When performing a calculation using precalculated radial matrix elements, the sections where the wave functions are loaded and where the radial matrix elements are calculated from the wave functions can be skipped.

The next four sections of the notebook assemble the single-atom Stark Hamiltonian. There are two main components to this Hamiltonian: the field-free atomic state energies on the diagonal of the matrix, and the off-diagonal Stark matrix terms. The Stark matrix terms are of the form:

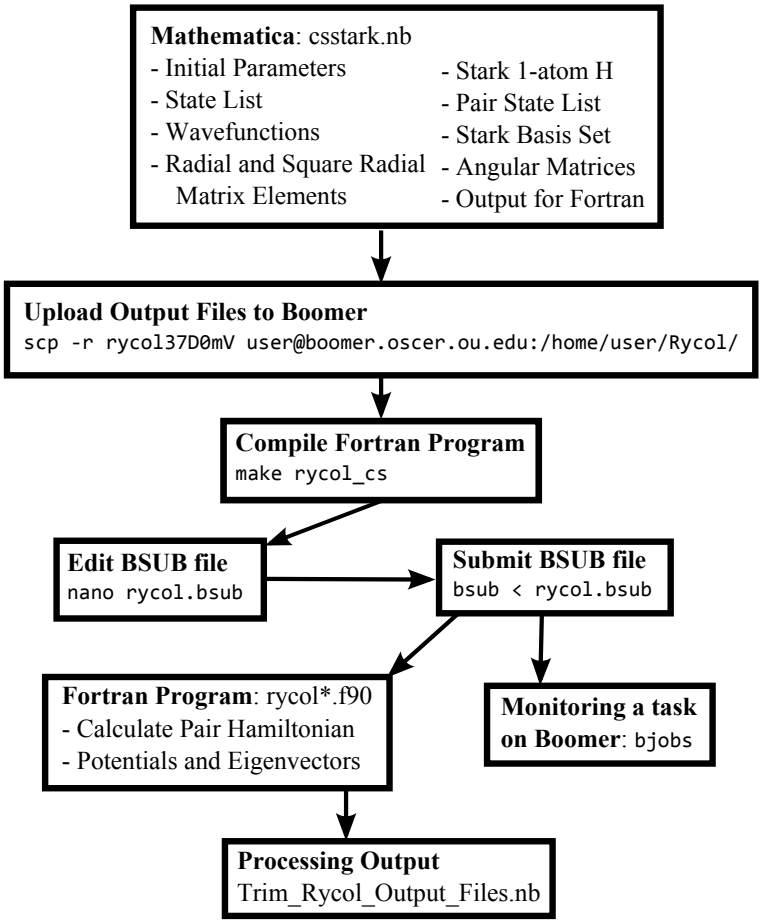

Figure A.1: Flowchart for the Rycol program, with example commands for each step in `monospace type`.

$$H_s(m_J) = \sum_{m_S=-1}^{1} \sqrt{\frac{l_{max}^2 - (m_J - m_S)^2}{(2l_{max}+1)(2l_{min}+1)}}$$
$$\langle l, m_J - m_S; 1/2, m_S \,|\, j, m_J\rangle \, \langle l', m_J - m_S; 1/2, m_S \,|\, j', m_J\rangle$$
$$\langle \psi_{nl}| \, r \, |\psi_{n'l'}\rangle \,,$$

where $\langle l, m_J - m_S; 1/2, m_S \,|\, j, m_J\rangle$ is the Clebsch-Gordan coefficient coupling the orbital angular momentum to the spin angular momentum of the atom, l_{max} is the greater of l and l', and l_{min} is the lesser of l and l'. Selection rules for dipole-allowed transitions are applied to determine which elements are non-zero.

The field-free energies are calculated using the formula:

$$E_{nlj} = -\frac{1}{2(n - \delta_{nlj})^2}, \tag{A.1}$$

where n is the principal quantum number of the state, l is the orbital quantum number, j is the total angular momentum quantum number, and δ_{nlj} is the quantum defect. For Rb, values for δ_{nlm} are available for each fine structure state [24, 25]. For Cs, only one j value for each l value has a specified δ_{nlm} in the literature [23], and instead the fine structure splitting is specified separately [26]. A diagonal matrix is built from the field-free energies and added to the Stark matrix to produce the single-atom Hamiltonian.

The notebook then calculates the square radial matrix elements $\langle \psi_{nl}| \, r^2 \, |\psi_{n'l'}\rangle$ using the same integration method as for the radial matrix elements. Similarly to the radial matrix elements, the square radial matrix elements are written to

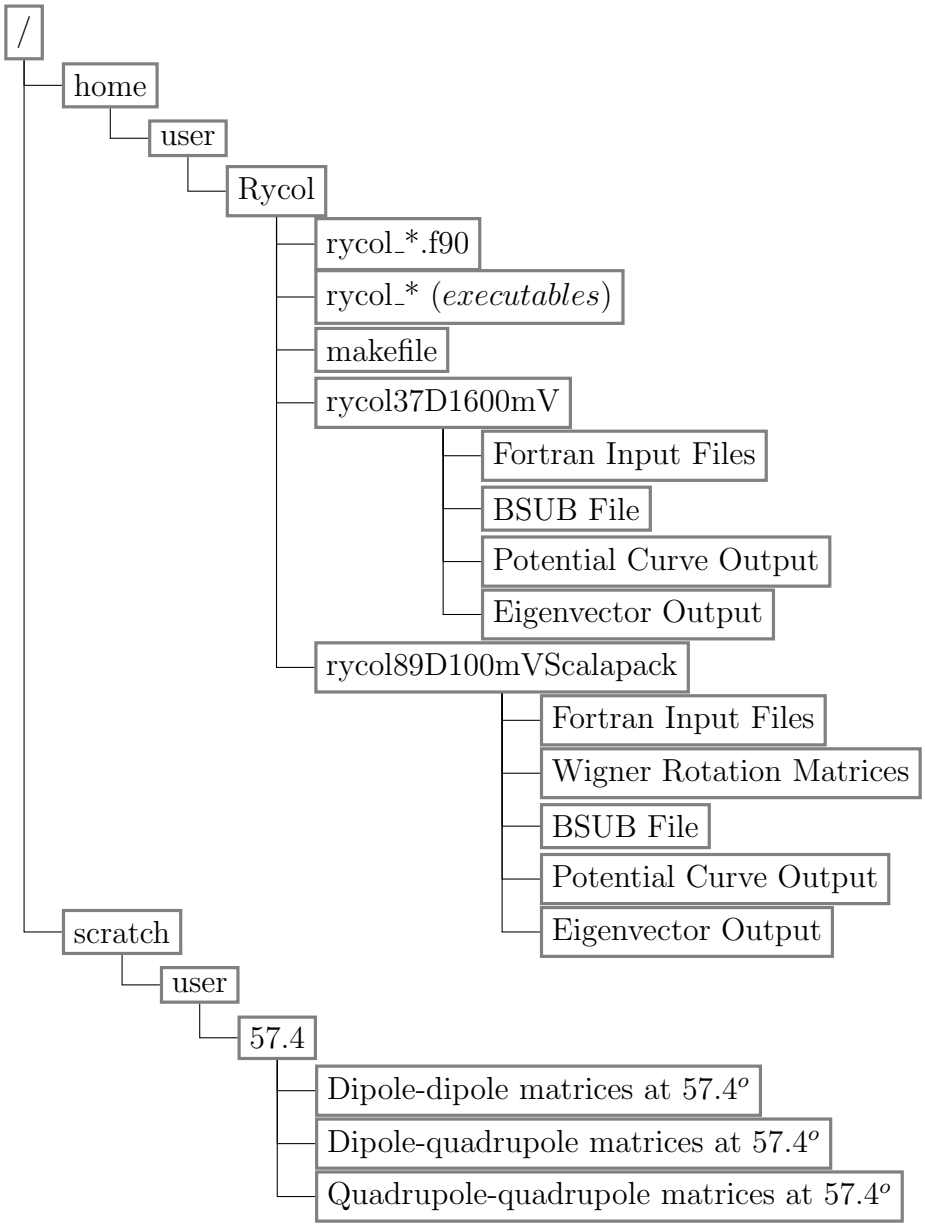

Figure A.2: Example filesystem layout on Boomer. Paths in the BSUB file must match the paths of the files on Boomer.

a file and can be reloaded for later use.

At this point, all the elements needed for the single-atom portion of the calculation have been collected. In the section "Rydberg-Rydberg Collision Data" the notebook collects the elements needed for the pair calculation. In the first subsection, "Set directory and parameters..." the `mycolstates` list formed earlier is used to generate a list of $|n, l, j, m_J\rangle$ single-atom states to be included in determining the list of pair states. In the subsection "Get all possible 2-atom states..." a list of pair states is generated by including all pairs of $|n, l, j, m_J\rangle$ single-atom states.

Not all of these pair states are necessary to include in the potential curve calculation, so the notebook determines which states to include by calculating the Stark-shifted energies of each pair state, sorts the list based on the energies, and then removes pair states outside an energy range determined by the `AsymptoticEnergyWidth` parameter specified at the beginning of the notebook. The command `Table[Length[mycolstates[M]], M, Mmin, Mmax]` shows the number of pair states included after filtering based on the pair state energies. For isotropic cases, the number of states needs to be greater than 1,000 for convergence, but less than 10,000 to avoid excessive memory usage by the Fortran program. If the number of l states included in the calculation is not truncated, then the number of states necessary for convergence will be $\sim 7,000$. For anisotropic calculations, the number of states that must be included for convergence is much greater, typically $\sim 50,000$. If the number of states included

falls outside this range, the number of states can be adjusted by changing the value of `AsymptoticEnergyWidth` and rerunning the first two subsections of "Rydberg-Rydberg Collision Data".

In the third subsection of "Rydberg-Rydberg Collision Data", "Get all the ingredients needed for the Hamiltonian matrix...", pair state energies are calculated and sorted, and the eigenvectors for each of the single-atom Stark states are calculated.

The following two sections are used to calculate the angular matrices used for the pair-state Hamiltonian. The matrices contain the matrix elements of the spherical harmonics:

$$\langle L_i, J_i, m_J | \, Y_l^m \, | L_k, J_k, m'_J \rangle \tag{A.2}$$

where $l = 1$ or 2, and $-l \leq m \leq l$. The values of l and m are indicated in the output file name. For example, "angmattwominusonesparse.dat" contains the matrix elements for Y_2^{-1} in sparse format.

The first section calculates the matrices using a dense-matrix format, and the second uses a sparse-matrix format. Which version should be used depends on the maximum l included in the calculation. If the basis is truncated at $l \leq 12$, then the non-sparse version should be used. Otherwise, the sparse-matrix version should be used. For non-truncated basis sets, this section can use a large amount of memory, typically $\sim$ 6GB. At the end of these subsections, the

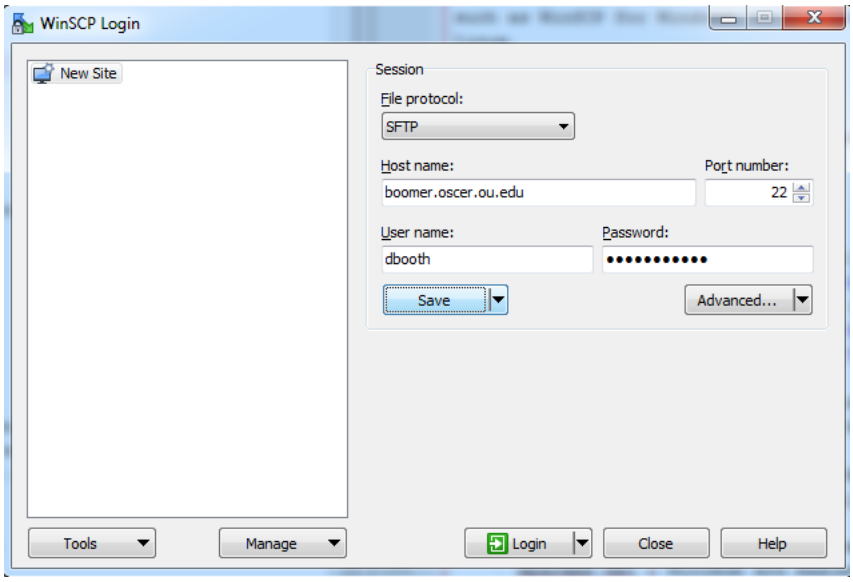

Figure A.3: An example setup for WinSCP to allow transferring files to Boomer.

angular matrices are written to the output directory.

The final subsection, "Output the ingredients for Fortran", writes the files necessary for the Fortran program to the output directory, specified by "csstarkDirectory <>fortDirectory".

The Mathematica notebook for the anisotropic case has two additional sections, which calculate and export Wigner rotation matrices for angles specified in the "Export Wigner matrix elements for Fortran" section. These matrices are required to rotate the pair-state Hamiltonian by the angle between the internuclear axis and the electric field axis, Θ.

A list of files output by the Mathematica notebook can be seen in Table A.2, with explanations of the contents of each file. The directory containing the output files can be copied to the university's supercomputer, Boomer, using a secure file

transfer protocol (SFTP) program, such as WinSCP for Windows, or the `sftp` command line program for Linux. An example of how to set up the connection for WinSCP is shown in Fig. A.3. The hostname, `boomer.oscer.ou.edu`, must be entered, and the default port number, 22, is used. Enter your username and password and click on the Save button to save the site so that the hostname does not need to be entered again.

A.2 Rycol Fortran program

A.2.1 Input files

In addition to the files output by the Mathematica notebook, one or more other files are needed by the Fortran program, depending on the type of calculation being done. For all cases, a batch submission (BSUB) file is needed. This file tells the BSUB program on Boomer how to load the Fortran program on the supercomputer's nodes, how many nodes to use, and how long to allow the program to run. An explanation of how to submit jobs on Boomer can be found at `http://www.oscer.ou.edu/boomer_quick_and_dirty.php#running`, including example BSUB files.

To calculate eigenvectors in addition to potentials, three additional files are required: "revecoutput.dat", which contains a list of internuclear separations in μm to output eigenvectors for, "rnumoutput.dat", which contains the number of items in the list in "revecoutput.dat", and "stateevecout.dat", which contains

Table A.2: The output of the Rycol Mathematica notebook and the contents of each file.

File	Contains
angmatlengths.dat †	Lengths of sparse angular matrices
angmat*sparseFS.dat †	Sparse angular matrices
angularmatricelement*FS.dat ‡	Non-sparse angular matrices
colEiM.dat	Collision energies for 1-atom states.
colparams$M$.dat	Parameters of the list of pair states in the basis set.
csRadialMatrixElement[Square].dat	Radial [square] matrix elements for 1-atom states.
eveciM.dat	Stark basis eigenvectors for 1-atom states.
mparams.dat	Minimum and maximum M value.
mycolstates$M$.dat	List of quantum numbers of all pair states included in the basis set.
rparams.dat	Maximum, minimum, and step size for the internuclear separations R.
statepos$M$.dat	Number of pair states in the basis set.

† Only generated when running sparse angular matrix calculation.

‡ Only generated when running non-sparse angular matrix calculation.

three elements: the minimum and maximum state numbers to output eigenvectors for, and the M value to calculate eigenvectors for.

In the anisotropic case, the Fortran program uses the Scalapack library, which shares matrices between multiple nodes. An additional file, "nprocs.dat" is required in this case. This file contains one integer, which is the number of processes in each grid that the matrices will be divided between. This number must divide evenly into the total number of processes, so that each grid has the same number of processes.

A.2.2 Compiling Rycol Fortran source code

There are several versions of the Rycol Fortran program, listed in Table A.3. The source code files are marked with the filename extension `.f90`. The program names are each marked with the atom (`rb` or `cs`) that the program calculates potentials for. The anisotropic versions of the program are marked with the word `rotation`. Versions marked with `allL` use sparse angular matrices, and versions without that word in the name use dense matrices. The versions of the program that calculate eigenvectors in addition to potentials are marked with `evecs`. If a program writes the dipole-dipole, dipole-quadrupole, and quadrupole-quadrupole matrices to disk, then it is marked with `save`, and if it loads the matrices from disk, it is marked with `load`.

Before compiling the source code, three commands need to be added to the user profile (a text file in the home directory named ".bash_profile"). They tell

Table A.3: Versions of the Rycol Fortran program with the function of each version.

Version	Functions
rycol_*.f90	Potentials using non-sparse angular matrices
rycol_*_allL.f90	Potentials using sparse angular matrices
rycol_*_allL_evecs.f90	Potentials and eigenvectors using sparse angular matrices
rycol_*_evecs.f90	Potentials and eigenvectors using non-sparse angular matrices
rycol_cs_rotation_evecs.f90	Potentials and eigenvectors for Cs in anisotropic case, using non-sparse angular matrices, loading dipole-dipole, dipole-quadrupole, and quadrupole-quadrupole matrices from disk
rycol_cs_rotation_load.f90	Potentials for Cs in anisotropic case, using non-sparse angular matrices, loading dipole-dipole, dipole-quadrupole, and quadrupole-quadrupole matrices from disk
rycol_cs_rotation_save.f90	Saves dipole-dipole, dipole-quadrupole, and quadrupole-quadrupole matrices to disk for Cs in anisotropic case, using non-sparse angular matrices

† $*$ is replaced by 'cs' for cesium, or 'rb' for rubidium.

the compiler which MPI library is being used and what hardware interface is being used. Those three commands are: `export MPI_COMPILER=intel`, `export MPI_LIBRARY=openmpi`, and `export MPI_HARDWARE=ib`.

To compile the source code files, a makefile is required. The makefile contains instructions that tell the `make` program on Boomer how to compile the source code file. The command `make all` compiles all versions of the program listed in the makefile, and individual versions can be compiled using the name of the executable: for example, `make rycol_cs_evecs`.

When compiled, the programs are linked to several library files that are necessary for tasks performed by the program. The programs must be linked to an MPI library for the parallel processing to work. Old versions of Rycol used the mvapich MPI library, but this library has been removed from Boomer, and so new versions use the OpenMPI library. Additionally, the matrix diagonalizations performed by Rycol require either the LAPACK or SCALAPACK libraries, depending on whether the matrices need to be divided between nodes. Generally, any Rycol run that uses a basis set larger than 10,000 states will require the SCALAPACK library. Smaller basis sets can use the LAPACK library. The anisotropic versions of the program are written to use SCALAPACK. Using SCALAPACK should be avoided in cases where it is not necessary, as communication between nodes is much slower than memory access, so a job dividing memory between nodes will run much slower than a job that stores full matrices in each node. The paths to each library are contained in the makefile under the

variable names `ScaLAlib` and `LAlib`, but these paths are likely to change when Boomer is replaced by a newer supercomputer.

A.2.3 Submitting a job to Boomer

Once the Fortran program is compiled and the input files are placed in the input directory, the job can be submitted to the batch processing queue. In the BSUB file, there is an `mpirun.lsf` command. The argument to this command should be the executable to be run. The path to the executable should be an absolute path, not a relative path. Never run the executable directly, as the MPI library requests exclusive use of the node it is run on, and running it directly would cause the login node to become inaccessible. Additionally, there is a `cd` command in the BSUB file, whose argument should be set to the input directory.

Once the parameters for the BSUB file are set, the job can be submitted with the command `bsub < rycol.bsub` (assuming the BSUB file is named `rycol.bsub`). The status of the job can be monitored using the `bjobs` command. When the job is first submitted it enters a queue (typically the "normal" queue), and its status will be listed as "pending". When there is time available on the supercomputer for the job, it begins running. If the job is still running when the amount of time specified in the BSUB file has passed, it will be automatically killed. Each job is assigned a number, shown after submitting the job and when running `bjobs`. To kill a job, use the command `bkill` with the job number as an argument, e.g. `bkill 5014781`.

A.2.4 Output files

When the program is completed, it will output files into the input directory named "evalssmallersteps$M$_new_.dat", which contain the potential curves of all the pair states in cm^{-1} as a function of internuclear distance in μm.

The Fortran program outputs the potential curves as a function of internuclear distance in files named "evalssmallersteps$M$.dat", where M is the total projection of the angular momentum. If the anisotropic version of the program is used, M is replaced by the rotation angle Θ at which the potentials were calculated. Each column in this file corresponds to one of the basis states.

Typically only a subset of the total basis set is needed. To trim the files to contain only the required states, there is a Mathematica notebook named "Trim_Rycol_Output_Files.nb". This notebook takes as input the atomic number (37 for Rb, 55 for Cs; for anisotropic potentials, this is not the actual atomic number, but is instead 56), the quantum numbers n and l, the electric field in mV/cm, the number of states to include in the trimmed file, and a list of angles to trim the potentials at (only used in the anisotropic case). The output is saved in the same directory as the input files, under the name "evals$M$.dat".

If eigenvectors were calculated, they are output under files named "evec$M$_R,S.dat", where M is the total projection of the angular momentum along the internuclear axis, R is the internuclear distance, and S is the state number label. The files contain a list of normalized eigenvector values, where

the nth row corresponds to the admixture of state n into state S.

Versions of the program that write matrices to the disk will write them to the scratch partition, which is a file system on Boomer which is separate from the home partition and has a larger disk space quota. Because the path for these files needs to be specified as an absolute path, these programs must be modified when being used by a different user account. The versions which load the matrices will need to be modified similarly.

A.2.5 Troubleshooting

If a job fails, it may fail to write potential files or eigenvector files. Troubleshooting can be done by looking at the error output from the program, which is written to two files, typically in the user's home directory. The names for the files are of the format "[job name].out.[job number]" and "[job name].err.[job number]". The ".out." file contains diagnostic information from the BSUB system, including when the job began running, the hostnames of the nodes the job ran on, and the final status of the job. If the job completed successfully, this status will be "Done", and if the job failed, it will be "Exit", followed by an error code.

If a job fails, useful information can usually be found by reading the ".err." file. This file contains information about the status of the program as it is running. Common failures include missing input files, jobs running out of time, and errors due to the program being compiled incorrectly.

Missing input files appear in the ".err." file as "error during read", followed by the name of the missing file. This error can be corrected by creating the needed file with the correct information and resubmitting the job.

If a job runs out of time, it will be noted in the ".out." file with the text "LSF Time Limit Exceeded." This error can be corrected either by reducing the scale of the calculation requested (for example, by editing `mparams.doc` to reduce the number of M values calculated) or by raising the time limit in the BSUB file and resubmitting the job.

If the program was compiled incorrectly (for example, if it was linked to the wrong library), the program may give error messages that seem unrelated to the problem. In these cases, it is important to check the libraries that are being linked to in the makefile. If the program is using the OpenMPI library (which was optional on the older supercomputers but required on Boomer), then the program should be linked to the OpenMPI version of the Basic Linear Algebra Communication Subprograms (BLACS). This should appear in the makefile as "-lmkl_blacs_openmpi_lp64". If the "openmpi_" portion of that argument is missing, it should be added, and the program should be recompiled. After the program is recompiled, the job can be resubmitted.

Appendix B

Publications

B.1 Publications

This is a list of peer-reviewed journal articles which I have been either an author or co-author on, in reverse chronological order.

8. D. Booth, S. Rittenhouse, J. Yang, H. Sadeghpour, and J. Shaffer, "Production of trilobite Rydberg molecule dimers with kilo-Debye permanent electric dipole moments ," Science **348**, 99 (2015).

7. A. Urvoy, F. Ripka, I. Lesanovsky, D. Booth, J. Shaffer, T. Pfau, and R. Löw, "Strongly correlated growth of Rydberg aggregates in a vapour cell," Submitted to Phys. Rev. Lett., Preprint available at arXiv:1408.0039, (2014).

6. H. Kübler, D. Booth, J. Sedlacek, P. Zabawa, and J. Shaffer, "Exploiting the coupling between a Rydberg atom and a surface phonon polariton for single-photon subtraction," Phys. Rev. A **88**, 43810 (2013).

5. J. Tallant, S. Rittenhouse, D. Booth, H. Sadeghpour, and J. Shaffer, "Observation of blueshifted ultralong-range Cs_2 Rydberg molecules," Phys. Rev. Lett. **109**, 173202 (2012).

4. J. Cabral, J. Kondo, L. Gonçalves, V. Nascimento, L. Marcassa, D. Booth, J. Tallant, A. Schwettmann, K. Overstreet, and J. Sedlacek, "Effects of electric fields on ultracold Rydberg atom interactions," J. Phys. B **44**, 184007 (2011).

3. J. Cabral, J. Kondo, L. Gonçalves, L. Marcassa, D. Booth, J. Tallant, and J. Shaffer, "Manipulation of quantum state transfer in cold Rydberg atom collisions," New Journal of Physics **12**, 93023 (2010).

2. J. Tallant, D. Booth, and J. Shaffer, "Photoionization rates of Cs Rydberg atoms in a 1064-nm far-off-resonance trap," Phys. Rev. A **82**, 63406 (2010).

1. K. R. Overstreet, A. Schwettmann, J. Tallant, D. Booth, and J. P. Shaffer, "Observation of electric-field-induced Cs Rydberg atom macrodimers," Nature Physics **5**, 581-585 (2009).

B.2 Presentations

This is a list of presentations that I gave or contributed to, in reverse chronological order.

19. D. Booth, J. Yang, and J. P. Shaffer, "Cs Trilobite Molecules and Rydberg Atom Interactions," Second International Workshop on Ultracold Rydberg Physics, Recife, Brazil (2014). (Poster)

18. D. Booth, J. Yang, and J. Shaffer, "Ultra-long range Red-Shifted Cs Trilobite Molecules in a 1064 nm Crossed Dipole Trap," DAMOP, Madison, WI (2014). (Talk)

17. D. Booth, Y. Jin, and J. Shaffer, "Cs Trilobite Molecules and Rydberg Atom Interactions," DAMOP, Madison, WI (2014). (Poster)

16. D. Booth, J. Tallant, P. Zabawa, G. Parker, and J. Shaffer, "Cs Trilobite Molecules and Rydberg Atom Interactions," DAMOP, Quebec City, QC, Canada (2013). (Poster)

15. J. Tallant, D. Booth, and J. Shaffer, "Ultra-long-range Cs Trilobite Molecules in a Crossed 1064 nm Dipole Trap," DAMOP, Anaheim, CA (2012). (Poster)

14. J. Tallant, D. Booth, J. Shaffer, S. Rittenhouse, and H. Sadeghpour, "Theoretical and Experimental evidence for the observation of trilobite states in Cs," DAMOP, Anaheim, CA (2012). (Talk)

13. D. Booth, J. Tallant, A. Schwettmann, and J. Shaffer, "Anisotropic Rydberg Interactions," DAMOP, Anaheim, CA (2012). (Talk)

12. J. Kondo, J. Cabral, L. Gonçalves, L. Marcassa, D. Booth, and J. Shaffer, "The effect of DC electric fields on nP cold Rydberg collisions," DAMOP, Atlanta, GA (2011). (Poster)

11. J. Tallant, D. Booth, L. Marcassa, B. Marangoni, and J. Shaffer, "Long-Range Trilobite-like Cs Molecules in a Crossed 1064 nm Dipole Trap," DAMOP, Atlanta, GA (2011). (Talk)

10. D. Booth, J. Tallant, B. Marangoni, L. Marcassa, and J. Shaffer, "Few-body Cs Rydberg Atom Interactions in a 1064nm Dipole Trap," DAMOP, Atlanta, GA (2011). (Poster)

9. D. Booth, J. Tallant, and J. P. Shaffer, "Few-body Cs Rydberg Atom Interactions in a 1064nm Dipole Trap," International Workshop on Ultracold Rydberg Physics, Recife, Brazil (2010). (Poster)

8. J. Tallant, D. Booth, and J. P. Shaffer, "Rydberg Atom-Rydberg Atom Molecules in Background Electric Fields," International Workshop on Ultracold Rydberg Physics, Recife, Brazil (2010). (Talk)

7. J. S. Cabral, J. M. Kondo, L. F Gonçalves, L. G. Marcassa, D. Booth, J. Tallant, and J. P. Shaffer, "Manipulation of quantum state transfer in cold Rydberg atom collisions," International Workshop on Ultracold Rydberg Physics, Recife, Brazil (2010). (Talk)

6. J. Tallant, D. Booth, A. Schwettmann, and J. Shaffer, "Rydberg tagging time-of-flight imaging: An improved apparatus for studying many-body processes," DAMOP, Houston, TX (2010). (Poster)

5. D. Booth, J. Tallant, A. Schwettmann, J. Shaffer, J. Cabral, J. Kondo, L. Gonçalves, and L. Marcassa, "Electric field effects on decay of Rb Rydberg atom pairs," DAMOP, Houston, TX (2010). (Talk)

4. A. Schwettmann, J. Tallant, D. W. Booth, C. E. Brown, and J. P. Shaffer, "Decoherence of a Rb BEC caused by stray magnetic fields and surface effects," DAMOP, Charlottesville, VA (2009). (Poster)

3. J. Tallant, A. Schwettmann, D. W. Booth, and J. P. Shaffer, "Rydberg tagging time-of-flight imaging to study 3-body Recombination," DAMOP, Charlottesville, VA (2009). (Poster)

2. A. Schwettmann, K. R. Overstreet, J. Tallant, D. W. Booth, and J. P. Shaffer, "Observation of Cs Rydberg atom macrodimers," DAMOP, Charlottesville, VA (2009). (Talk)

1. D. W. Booth, A. Schwettmann, J. P. Shaffer, J. S. Cabral, L. F. Gonçalvez, and L. G. Marcassa, "Electric field effects on cold Rydberg atom nD-nD pair collisions," DAMOP, Charlottesville, VA (2009). (Poster)